Air-coupled ultrasonic inspection of fiber reinforced composite materials

Ander Dominguez-Macaya Lopez

Supervisors:

Dr. Jon Aurrekoetxea (Mondragon Unibertsitatea)

Dr. Aitzol Iturrospe (Mondragon Unibertsitatea)

A thesis submitted for the degree of
Doctor by Mondragon Unibertsitatea

Department of Mechanics and Industrial Production

&

Department of Electronics and Computer Science

Mondragon Goi Eskola Politeknikoa
Mondragon Unibertsitatea

FEBRUARY 2020

Aita eta ama-rentzako

Baita Zaloa-rentzako ere

Acknowledgements

Completing my PhD has been a challenge that would not have been possible without those who have helped me in this adventure.

First and foremost, I would like to express my gratitude to my thesis supervisors, Dr. Jon Aurrekoetxea and Dr. Aitzol Iturrospe. I would like to thank them for giving me the chance to carry out this thesis and the confidence placed on me.

Furthermore, I would like to thank my co-workers from the Signal Theory and Communications, and the Polymer and Composites Technology of Mondragon Unibertsitatea who have provided feedback and help for this thesis, particularly to Dr. Iván Saenz.

I would like to thank the Government of the Basque Country for the grant received to carry out the PhD thesis (grant number PRE_2018_2_0220) and the stay at the Bundesanstalt für Materialforschung und –prüfung for three months (grant number EP_2019_1_0040).

My sincere thanks also go to Dr. Tomás Enrique Gómez for helping me with some of the technical stuff and Dr. Mate Gaal for giving me the chance to see and learn how other groups work. Their knowledge has given added depth to my thesis.

Additionally, I would like to thanks to those who have given me all the opportunities to be what I am today: my parents, Jaime and Marta.

Last, but not least, my greatest appreciation goes to my girlfriend, Dr. Zaloa Fernandez Ganzabal. We have been together for the last 8 years through thick and thin, supporting each other during our PhD theses. It has been 8 years but I hope it will be far more…

Abstract

The increase in the use of composite materials in recent years has led the industry into the development of new composite manufacturing processes, like the 3D ultraviolet pultrusion. These new manufacturing processes usually reduce manufacturing costs, cycle time or both. Ensuring the quality of the parts manufactured with these new processes is critical. Therefore, it is necessary to gain knowledge on these manufacturing processes, especially on the behavior of the material during the cure. To monitor these processes, the development of new non-destructive inspection techniques is required. For the 3D ultraviolet pultrusion, the use of non-contact non-destructive testing is necessary. Moreover, for structural parts, ensuring the required mechanical properties gives added value to the part.

In this thesis, the viability of air-coupled ultrasonics for plate-like fiber reinforced parts manufacturing is evaluated. At first, isotropic materials are evaluated, considering the ultraviolet cure of a vinyl ester resin. Air-coupled ultrasonics has proved to be fast enough to follow the ultraviolet cure, with quasi-normal ultrasonic spectroscopy. Then, the mechanical properties in fiber reinforced polymers with air-coupled ultrasonics are evaluated. The optimal set-up to generate leaky Lamb waves in plates with different properties is defined. Air-coupled ultrasonics showed that is what difficult to generate Lamb modes with different velocities, although it was possible with a mixed air-coupled laser ultrasonics set-up. Last, leaky Lamb waves where used with air-coupled ultrasonics to evaluate the properties of a fiber reinforced polymer during the thermal cure. The stiffness tensor of the composite was measured during the cure observing the largest variation at the last stages of the cure.

The main conclusion of this thesis is that the potential of air-coupled ultrasonics to monitor the fiber reinforced manufacturing processes is elevated. It can presents both the speed required to monitor fast curing processes like ultraviolet cure, with single measurements in less than a second; and the ability to characterize the full matrix of an orthotropic fiber reinforced polymer, through the use of micromechanical models. Air-coupled ultrasonics can be used to characterize the properties of materials with different geometries, like curves or hollow.

Resumen

El aumento en el uso de materiales compuestos en los últimos años ha llevado a la industria al desarrollo de nuevos procesos de fabricación de maetriales compuestos, como la pultrusión ultravioleta 3D. Estos nuevos procesos de fabricación, generalmente reducen los costes, el tiempo de ciclo o ambos. Garantizar la calidad de las piezas fabricadas con estos nuevos procesos es fundamental. Por lo tanto, es necesario obtener conocimiento sobre estos procesos de fabricación, especialmente sobre el comportamiento del material durante el curado. Para monitorizar estos procesos, se requiere el desarrollo de nuevas técnicas de inspección no destructivas. Para la pultrusión ultravioleta 3D, es necesario el uso de pruebas no destructivas sin contacto. Además, para las partes estructurales, garantizar las propiedades mecánicas requeridas da un valor añadido a la parte.

En esta tesis, se evalúa la viabilidad de los ultrasonidos con acoplamiento por aire para la fabricación de piezas reforzadas con fibra de tipo placa. Al principio, se evalúan los materiales isotrópicos, considerando el curado ultravioleta de una resina viniléster. Los ultrasonidos con acoplamiento por aire han demostrado ser lo suficientemente rápidos como para seguir el curado ultravioleta, por medio de espectroscopía ultrasónica en angulo quasi-normal. Después, se evalúan las propiedades mecánicas en los polímeros reforzados con fibra con ultrasonidos con acoplamiento por aire. Se define la configuración óptima para generar ondas de Lamb por aire, en placas con diferentes propiedades. Los ultrasonidos con acoplamiento por aire demostraron que es lo difícil generar modos de Lamb con diferentes velocidades, aunque fue posible con una configuración mixta de ultrasonidos láser y con acomplamiento por aire. Por último, las ondas de Lamb por aire se han utilizado con los ultrasonidos con acoplamiento por aire para evaluar las propiedades de un polímero reforzado con fibra durante el curado térmico. El tensor de rigidez del material compuesto se midió durante el curado observando las mayores variaciones al final del curado.

La principal conclusión de esta tesis es que el potencial de los ultrasonidos con acoplamiento por aire para monitorear los procesos de fabricación reforzados con fibra es elevado. Puede presentar tanto la velocidad requerida para monitorizar procesos de curado rápido como el curado ultravioleta, con mediciones en menos de un segundo; y la capacidad de caracterizar la matriz de rigidez ortotrópica de un polímero reforzado con fibra, mediante el uso de modelos micromecánicos. Los ultrasonidos con acoplamiento por aire se pueden usar para caracterizar las propiedades de materiales con diferentes geometrías, tanto curvas como huecas.

Laburpena

Material konposatuen erabileraren hazkundeak azken urteetan, material konposatuetarako fabrikazio prozesu berriak garatzera bultzatu du industria, esaterako, 3D pultrusio ultramorea. Fabrikazio prozesu berri hauek, oro har, kostuak, zikloaren denbora edota biak murrizten dituzte. Prozesu berri hauekin fabrikatutako piezen kalitatea bermatzea ezinbestekoa da. Hori dela eta, beharrezkoa da fabrikazio prozesu horien inguruko ezagutza lortzea, batez ere materialak ontzeko garaian. Prozesu horien jarraipena egiteko, suntsitzaileak ez diren ikuskapen teknika berriak garatzea beharrezkoa da. 3D pultrusio ultramorearentzako, beharrezkoa da kontaktu gabeko teknika ez suntsitzaileak erabiltzea. Gainera,pieza estrukturalen kasuan, beharrezkoak diren propietate mekanikoak bermatzeak balio erantsia ematen dio piezei.

Tesi honetan zuntzekin indartutako polimerozko plaka motako piezak, airez akoplaturiko ultrasoinuarekin erabiltzeko bideragarritasuna ebaluatu da. Hasieran, material isotropoak ebaluatu dira, binilester erretxina baten ontze ultramorea kontuan hartuta. Airearen akoplamenduarekin egindako ultrasoinuek ultravioleta ontzea jarraitu ahal izateko nahikoa azkarra dela frogatu da, ultrasoinuen espektroskopia bidez, angelu ia normala dela medio. Ondoren, airezko ultrasoinuekin zuntzekin indartutako polimerozko plaken propietate mekanikoak ebaluatzen dira. Airez akoplaturiko ultrasoinuekin Lamb uhinak sortzeko konfigurazio hoberena ebaluatzen da, propietate desberdinak dituzten plakekin. Airearen akoplamenduaerabiltzen duten ultrasoinuek agerian uzten dute zaila dela abiadura ezberdineko Lamb moduak sortzea, baina laser eta airezko ultrasoinuen konfigurazio mistoarekin posible izan zen. Azkenik, airez sorturiko Lamb uhinak erabili dira ontze termikoan zuntzez indartutako polimero baten propietateak zehazteko. Material konposatuko zurruntasuna ontze garaian neurtu zen, ontzearen amaieran aldakuntza handienak ikusiz.

Tesi honen ondorio nagusia hauxe da: airez akoplaturiko ultrasoinuekin zuntzekin indartutako polimerozko fabrikazio prozesuak kontrolatzeko duen potentziala handia dela. Bai ultramore ontze prozesu azkarra bezalako prozesuetan, behar den abiadura izan dezake, segundo bat baino gutxiagoko neurketekin; eta zuntz indartutako polimero baten zurruntasunaren matrize neurtzeko gaitasuna, eredu mikromekanikoak erabiliz. airez akoplaturiko ultrasoinuekin geometria ezberdinekin materialen propietateak neurtzeko erabil daitezke, kurbatuak eta hutsak adibidez.

Declaration of Originality

I hereby declare that the research recorded in this thesis and the thesis itself were developed entirely by myself at the Signal Theory and Communications, and the Polymer and Composites Technology research groups, at Mondragon Unibertsitatea.

Ander Dominguez-Macaya Lopez
Polymer and Composites Technology & Signal Theory and Communications
Mondragon Unibertsitatea
February 2020

Contents

Acknowledgements iii
Abstract v
Declaration of Originality xi
Contents xiii
List of Figures xv
List of Tables xvii
Acronyms xix
1. Introduction 1
1.1 Motivation 1
1.2 State of the art 3
1.2.1 Monitoring the FRP manufacturing processes 4
1.2.2 Material characterization with US 12
1.2.3 NCU: ACUS 16
1.3 Critical assessment of the state of the art 20
1.4 Objectives 21
1.5 Outline of the thesis 22
1.6 Publications 22
2. Monitoring the UV curing of a vinyl ester resin with ACUS 23
2.1 Theoretical background 23
2.1.1 Single-layer normal plane wave 23
2.1.2 Multi-layer non-normal plane wave transmission 24
2.1.3 Relationship between the acoustic and mechanical properties 26
2.2 Set-up and methodology 27
2.3 Results 29
2.3.1 Characterization before curing 29
2.3.2 Characterization during curing 31
2.3.3 Characterization after curing 36
2.4 Conclusions 37
3. Leaky Lamb waves with ACUS 39
3.1 Theoretical background 39
3.1.1 Transfer matrix method 41
3.1.2 Stiffness matrix method 44

3.1.3 Mixed TMM & SMM 46
3.2 Set-up and methodology 46
3.2.1 Straight and curved composite plate 46
3.2.2 Transducer efficiency: geometry and multimode generation 48
3.3 Results 50
3.3.1 Straight and curved composite plate 50
3.3.2 Transducer efficiency: geometry and multimode generation 52
3.4 Conclusions 57
4. Monitoring the thermal curing of a GFRP with ACUS 59
4.1 Theoretical background 59
4.1.1 Micromechanics 59
4.1.2 Mixed TMM & SMM 61
4.2 Set-up and methodology 61
4.3 Results 64
4.3.1 Sensitivity analysis 64
4.3.2 Cure monitoring 70
4.4 Conclusions 75
5. Summary and conclusions 77
5.1 Conclusions 77
5.2 Suggestions for Further Research 78
References 79

List of Figures

Figure 1-1: Traditional pultrusion process. 2
Figure 1-2: 3D-UV pultrusion process [Saenz-Dominguez **2018**]. 3
Figure 1-3: Pressure transducer for mold filling detection [Legault **2015**]. 4
Figure 1-4: Industrialized thermocouple embeddable into the mold [Thermometrics **2014**]. 5
Figure 1-5: Increased grating space (b) as opposed to a free fiber (a) [Konstantopoulos **2014**]. 6
Figure 1-6: Point voltage sensor (a) and cross-section view (b) [Tuncol **2007**]. 7
Figure 1-7: Through thickness ultrasonic measurement [Aggelis **2012**]. 8
Figure 1-8: IR thermography result of an uncured carbon fiber composite plate [Cuevas **2013**]. 9
Figure 1-9: Representation of THz pulsed spectroscopy waveform detector for Polymer Composite Materials [Yakovlev **2015**]. 10
Figure 1-10: Non-contact US monitoring set-up [Lionetto **2007**b]. 10
Figure 1-11: Schematic RUS setup. A rectangular parallelepiped suspended along a body-diagonal between transmitter and receiver is excited with a frequency sweep [Visscher **1991**]. 12
Figure 1-12: A RUS spectrum for a copper parallelepiped. The arrows indicate the computed frequencies based on a fit of the first 50 resonances [Leisure **1997**]. 13
Figure 1-13: (a) EMAT transducer [Nakamura **2012**] and (b) LUS wave generator and receiver [An **2013**]. 17
Figure 1-14: Piezoelectric transducer schematic. 19
Figure 1-15: CMUT schematic. 19
Figure 2-1: Plane-wave transmission in a multilayered plate. 25
Figure 2-2: Set-up to monitor the UV curing process with ACUS. 28
Figure 2-3: Frequency response of the PC plate (a) and the VE_{thick} plate (b). 30
Figure 2-4: Thickness of the VEthin with the DoC. 32
Figure 2-5: Temperatures in the PC plate during curing. 33
Figure 2-6: Temperatures in the upper (T_{AirUp}) and lower ($T_{AirDown}$) layers of air at 30 mm distance from the VE_{thin} and the PC. 33
Figure 2-7: Evolution of the acoustic properties during the cure: (a) longitudinal wave properties, (b) longitudinal complex modulus, (c) shear wave properties and (d) shear complex modulus. 35
Figure 2-8: Longitudinal storage modulus and DoC (a), and evolution of the elastic Young's modulus with the DoC (b). 36
Figure 3-1: Incident wave in plate. 39
Figure 3-2: Refracted waves in semi-infinite FRP medium. 40
Figure 3-3: Omega geometry. 47
Figure 3-4: Set-up for the measurement of the straight section. 48
Figure 3-5: Set-up for the measurement of the curved section. 48
Figure 3-6: Set-up for the measurement of the straight and curved section with the 3D-LDV. 50
Figure 3-7: Lamb wave measured and calculated dispersion curves of the straight (a) and curved (b) sections of the part. 52

Figure 3-8: Laser measurement of the simultaneous generation of Lamb modes with different velocities in the curved (a,b) and straight (c,d) sections: displacement in propagation direction (a,c) and in the thickness direction (b,d). 56
Figure 4-1: Set-up to measure the LLW with a fully ACUS and a PZT receiver. 62
Figure 4-2: Dispersion curves for the partially (a) and fully (b) cured GFRP for ΔE. .. 65
Figure 4-3: A0 mode in the partially and fully cured GFRP for ΔE. 65
Figure 4-4: S0 mode in the partially and fully cured GFRP for ΔE..... 66
Figure 4-5: A1 mode in the partially and fully cured GFRP for ΔE. 67
Figure 4-6: Dispersion curves for the partially (a) and fully (b) cured GFRP for $\Delta \nu$. ... 67
Figure 4-7: A0 mode in the partially and fully cured GFRP for $\Delta \nu$..... 68
Figure 4-8: S0 mode in the partially and fully cured GFRP for $\Delta \nu$. 68
Figure 4-9: A1 mode in the partially and fully cured GFRP for $\Delta \nu$..... 69
Figure 4-10: Frequency response change of the GFRP measured with the ACUS during the cure: (a) 0:45 h, (b) 2:00 h, (c) 2:45 h, (d) 3:30 h, (e) 4:15 h and (f) 5:00 h. 71
Figure 4-11: Evolution of the Young's modulus of the VE. 72
Figure 4-12: Evolution of Poisson's ratio of the VE. 73
Figure 4-13: Evolution of (a) Young's modulus and (b) Poisson's ratio compared with the DoC. 73
Figure 4-14: Evolution of Young's modulus and Poisson's ratio with the DoC. 74

List of Tables

Table 1-1: FRP manufacture monitoring techniques for 3D-UV pultrusion. 11
Table 2-1: Extracted acoustic properties before curing. 31
Table 2-2: Extracted mechanical properties before curing. 31
Table 2-3: Extracted acoustic properties of the VE_{thin}. 36
Table 2-4: Extracted elastic mechanic properties of the VE_{thin}. 37
Table 3-1: Fitted elastic properties for the main direction of the plates. 52
Table 3-2: Sensitivity of the evaluated piezocomposite transducers in pulse-echo. 53
Table 3-3: Normalized transmission efficiency of guided modes in the straight section. 55
Table 3-4: Normalized transmission efficiency of guided modes in the curved section. 55
Table 4-1: Initial parameters of the composite. 63
Table 4-2: Properties of the GFRP. 75

Acronyms

2D-FFT	*2-Dimensional Fast Fourier Transform*
3D-UV	*3-Dimensional Ultraviolet*
3D-LDV	*3-Dimensional Laser Doppler Vibrometer*
ACUS	*Air-Coupled Ultrasonic*
CSIC	*Centro Superior de Investigaciones Científicas*
DC	*Direct-Current*
DFT	*Discrete Fourier Transform*
DoC	*Degree of Curing*
DSC	*Digital Scanning Calorimetry*
EM	*Electromagnetic*
EMAT	*Electromagnetic Acoustic Transducers*
FFT	Fast Fourier Transform
FRP	*Fiber Reinforced Polymer*
GFRP	*Glass Fiber Reinforced Polymer*
IR	*Infrared*
LDV	*Laser Doppler Vibrometer*
LLW	*Leaky Lamb Waves*
NCU	*Non-Contact Ultrasonic*
NDE	*Non-Destructive Evaluation*
NDT	*Non-Destructive Testing*
OFI	*Optical Fiber Interferometry*
PC	*Polycarbonate*
RUS	*Resonant Ultrasonic Spectroscopy*
SMM	*Stiffness Matrix Method*
TC	*Transmission Coefficient*
THz	*Terahertz*
TMM	*Transfer Matrix Method*
TOF	*Time Of Flight*
US	*Ultrasonic*
UV	*Ultraviolet*

VE *Vinyl Ester*

Chapter 1
Introduction

The thesis “Air-coupled ultrasonic inspection of fiber reinforced composite materials” has been carried out inside the *Mechanical Engineering and Electrical Energy* Ph.D. program of Mondragon Unibertsitatea in a collaboration between the *Signal Theory and Communications* & the *Polymer and Composites Technology* research groups of Mondragon Unibertsitatea. The Basque Government through the Predoctoral Program (grant number PRE_2018_2_0220) has funded this thesis.

1.1 Motivation

With the objective of guaranteeing the competitiveness and growth in a globalized market, the European industrial sector faces several technological challenges. Many of these challenges are aimed to develop new high added value materials. [Premix **2013**]. Inside of the group of high added value materials are the fiber reinforced polymers (FRP), due to their many advantages [Premix **2013**]: weight reduction, high elastic properties and good behavior to fatigue. In fact, the global market of composites was estimated to be 81.7 billion dollars in 2016 and is expected to reach 109.4 billions by 2022 [EPTA **2018**]. Despite those figures, the composite market is mostly restricted to low production volume and high added value applications. This is due to the high operational cost and low productivity of the manufacturing processes used nowadays. According to the result of the analysis carried out by the journal Composites World in 2018 [Sloan **2018**], the 62% of the surveyed did not expect an increase in the use of composite in the automobile industry in the next two years. Thus, it would be logical that one of the challenges of the manufacturing industries relies on the automation of the manufacturing process. In this sense, Bader [Bader **2002**] carried out a comparison of the cost of the workforce to manufacture the same composite part with different manufacturing processes. The study concluded that pultrusion is the most cost efficient regarding workforce.

Pultrusion is a highly automated continuous process to manufacture straight profiles with high mechanical properties in the longitudinal direction [Tena **2014**]. As it can be observed in Figure 1-1, the pultrusion machine is composed of a fiber storage section (1), a resin bath (2), a preform (3), a heating mold (4), a pulling system (5) and a cutting section (6). The fibers are introduced in a resin bath. Once impregnated, a series of preforms guide the fibers to the entrance of the mold where it is thermally cured. With a mold, straight profiles or parts with fixed curvature radius can be obtained.

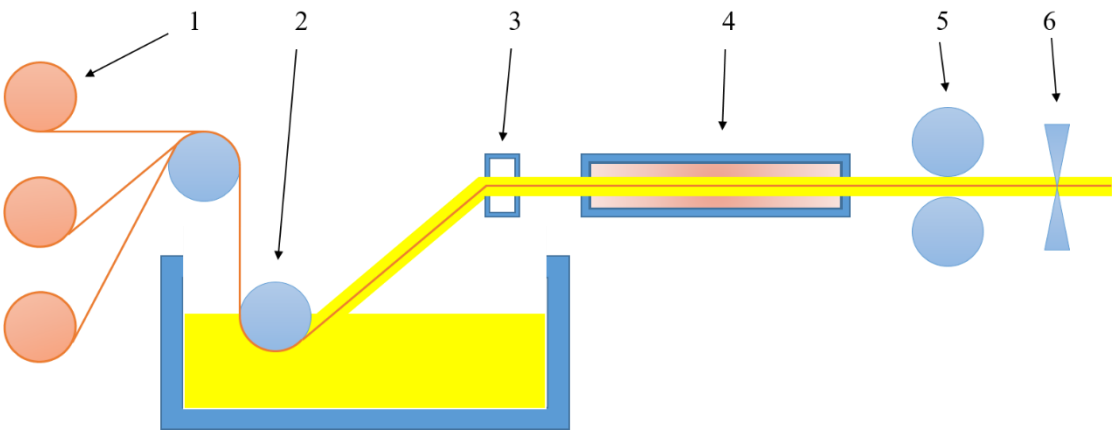

Figure 1-1: Traditional pultrusion process.

Curing the profile inside of a mold carries several limitations [Tena **2015**] such as elevated process incidences, an insufficient manufacturing speed and a reduced manufacturing flexibility. It also requires expensive high pulling force equipment and long heated molds.

These and other limitations are mainly caused by curing inside of a mold. Curing outside of a mold could solve some of these limitations, improving the manufacturing speed, flexibility or reducing the requirements over high pulling force equipment and long molds [Saenz-Dominguez **2018**; Tena **2015**]. However, curing thermally outside of the mold is not viable. Curing with ultraviolet (UV) light has proven to be a cost effective technology to cure polymers outside of the mold [Saenz-Dominguez **2018**; Tena **2015**]. Moreover, a reduction in pulling forces, an increase in profile geometry flexibility and productivity has been observed [Saenz-Dominguez **2018**; Tena **2015**]. All of these advantages have been obtained through the development of the 3-dimensional ultraviolet (3D-UV) pultrusion curing process [Tena **2015**].

The 3D-UV pultrusion curing process (Figure 1-2) is similar to the classical pultrusion process (Figure 1-1), with the main differences being in the die, the curing technology and the pulling method [Tena **2015**]. The 3D-UV process uses a short die, which reduces the friction of the uncured composite. The curing is carried out with UV light right outside of the mold in a fast manner. The pulling method used is a robotic arm, which, contrary to the classical pultrusion, gives flexibility to the manufactured parts. Despite these advantages, the 3D-UV curing pultrusion process is still quite new. It requires information on the manufactured part, which would ensure part quality.

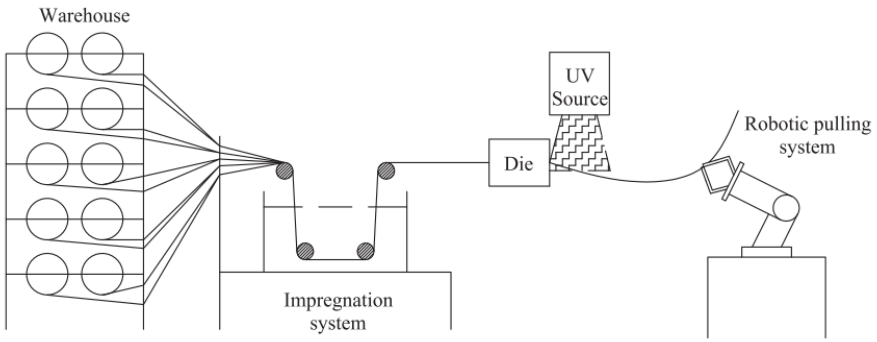

Figure 1-2: 3D-UV pultrusion process [Saenz-Dominguez **2018**].

The quality of the FRP composite parts can be evaluated from two points of view: beauty and safety. Beauty is of importance when the part is exposed, usually in expensive sports cars or ships. Despite the importance of the luxury market, the most critical area and the one in which 3D-UV pultrusion is mostly focused, is safety. It is for safety reasons that the manufacturing processes of FRP have always been forced to evaluate many, if not all, of their manufactured parts. Evaluating the manufactured parts with the most commonly used destructive tests, which consist of picking the manufactured part and destroying it through heat, brute force or others, is not a cost efficient means. Moreover, some FRP manufacturing processes present high variability [Mesogitis **2014**], which may cause the unevaluated part to not have the same quality. Since destroying every part that is manufactured is not the best business mode, non-destructive testing (NDT) comes forth as a good alternative.

NDT is an interdisciplinary field in science and technology where the properties of a part are evaluated without causing any damage to the part. Due to the non-damaging nature of these tests, NDT can be used to evaluate all of the manufactured parts, wasting less material and ensuring the quality of every part. The parts can also be evaluated during the manufacturing process itself, where information on how the material is changing can be obtained. Evaluating the state of the material at each point during the manufacturing process can be used to control the manufacturing process with feedback information. Furthermore, the information obtained during the manufacture process can be used in the design process itself. The evolution of the evaluated properties can be used in future parts, thus saving time and money in the long run. To ensure that the information that is obtained is valuable and meaningful for the process, finding and selecting the most adequate NDT technique is of outmost importance.

1.2 State of the art

This section describes the techniques and methods reviewed throughout the dissertation to characterize the properties of composite materials. The literature review is dived in three sections:

- Evaluation of the techniques that monitor the manufacturing processes of FRP materials and selection of the best fitting for the 3D-UV pultrusion (Section 1.2.1).
- Evaluation of the techniques to characterize FRP materials with ultrasonics (Section 1.2.2).
- Evaluation of non-contact ultrasonic techniques to characterize composite materials (Section 1.2.3).

1.2.1 Monitoring the FRP manufacturing processes

1.2.1.1 Contact inspection techniques

Contact inspection has been long used in FRP manufacturing [Cielo **1989**; Fink **1999**; Roberts **1991**; Webster **1999**]. This techniques do not directly fit a process like the 3D-UV pultrusion, but have been used in laboratory environment to gain knowledge over the UV cure process [Saenz-Dominguez **2018**]. They can also be used as validation methods and are therefore evaluated here.

1.2.1.1.1 Pressure

Pressure sensing is usually based on the piezoelectric effect, in which a pressure applied to an object generates a change in electric voltage. The piezoelectric sensors are embedded in a shell where the pressure under measurement and a reference probe can be isolated. There are different types of measurements depending on the reference pressure (absolute, gage or differential respectively) [Webster **1999**]. This kind of sensors are most popular in mold filling monitoring [Di Fratta **2013**; Govignon **2013**], as the correct filling of the composite part is crucial to ensure correct mechanical capabilities. Figure 1-3 shows an in-mold embedded pressure transducer for resin transfer molding (RTM) manufacturing.

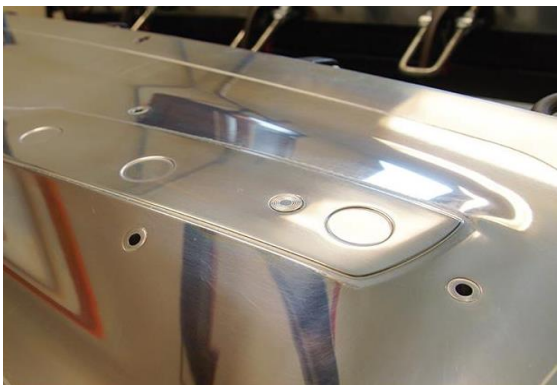

Figure 1-3: Pressure transducer for mold filling detection [Legault **2015**].

Pressure transducers, are one of the simplest and cheapest monitoring sensors. Moreover, these sensors are capable of withstanding harsh conditions of temperature and pressure, with more than 200 ºC and 20 bars, and are easily embeddable in-mold [Konstantopoulos **2014**]. However, these sensors require multiple transducers to estimate the filling status and cannot monitor the curing process effectively. Since the

UV pultrusion does not have a mold to fill and the most important part is the curing, the use of pressure transducers does not provide any valuable information.

1.2.1.1.2 Thermocouples

Thermocouples are used to measure part temperature. Thermocouples make use of the thermoelectric effect, which consists of two metal alloys in contact that produce a voltage differential proportional to the temperature difference.

Thermocouples have been widely used to measure the filling and curing process of different FRP manufacturing processes [Balvers **2009**; Tuncol **2007**]. Distributed thermocouples [Hsiao **2006**] have been used to obtain an estimation of the temperature image of the part being monitored. This is at relatively low cost of sensors and post-processing complexity. Furthermore, thermocouples can easily be embedded into the mold as industrialized thermocouples can withstand up to 750 ºC. Figure 1-4 shows an example of an embeddable thermocouple.

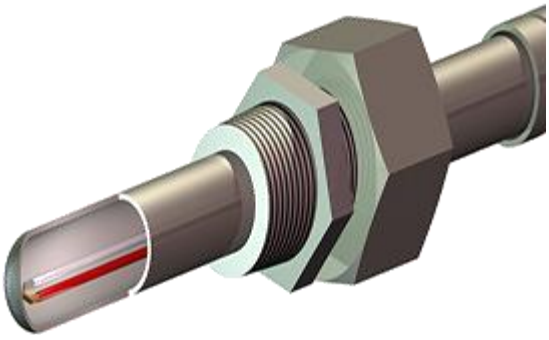

Figure 1-4: Industrialized thermocouple embeddable into the mold [Thermometrics **2014**].

Thermocouples are similar to pressure sensors in their advantages and disadvantages. These are simple, easy and cheap to use but can only make measurements at a point, with the possibility to make estimation but not actual measurements of the whole part. Despite the similarities, thermocouples can actually be used to monitor the curing process.

1.2.1.1.3 Optical fiber interferometry

Optical fiber interferometry (OFI) sensors make use of the electromagnetic wave interference. Fabry-Pérot interferometers are the most popular in optical fiber interferometry [Kalamkarov **1999**; Zhou **2002**]. These interferometers generate a partial reflection of the traveling light. When an external strain or thermal deformation influences the optical fiber, the spacing between the reflective surfaces vary, as do their refractive index [Konstantopoulos **2014**]. An example of this is shown in Figure 1-5.

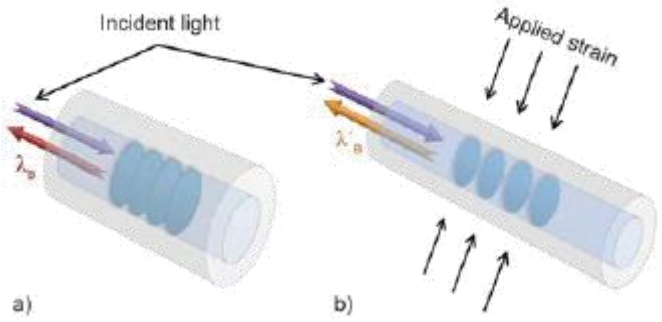

Figure 1-5: Increased grating space (b) as opposed to a free fiber (a) [Konstantopoulos **2014**].

The optical path is controlled by optical fibers, which make these devices compact and economic. Fiber Bragg Grating is the most used technology inside de Fabry-Pérot interferometers, where a distributed Bragg reflector is constructed in a short segment of the fiber, refracting particular wavelengths of light. Mold embedded optical fibers have been used for mold filling [Dunkers **2001**] and curing [Jung **2007**] monitoring. There have also been aims to make smart parts through embedding these sensors in the part [Zhou **2002**], but embedding the fibers can alter the mechanical properties of the part [Roberts **1991**; Sirkis **1995**].

OFI has been used to monitor residual strains during pultrusion [Kalamkarov **1999**] for straight parts. Optical fibers are delicate, which limits the application in industrial environments, and the curved shape of the 3D pultruded part could damage them if the curve were too sharp. However, OFI can be used during and after manufacturing which may be of interest in some cases.

1.2.1.1.4 Direct-current

Direct-current (DC) sensors measure the conductivity of a medium between two points as the part closes the circuit between the two measuring points. Once the circuit is closed, the voltage output is measured, which is proportional to the ion viscosity (ρ) [Konstantopoulos **2014**]. This type of sensors have been used both for mold filling [Bickerton **2001**; Lawrence **2002**; Tuncol **2007**] and curing [Garschke **2012**; Tena **2013**, **2016**] monitoring. Flowing resin closes the circuit during the filling process, thus allowing knowing when the resin has reached a point, but it also changes its resistance during the curing process, which allows using the same sensor to monitor both. Figure 1-6 shows an example of a mold embeddable DC sensor.

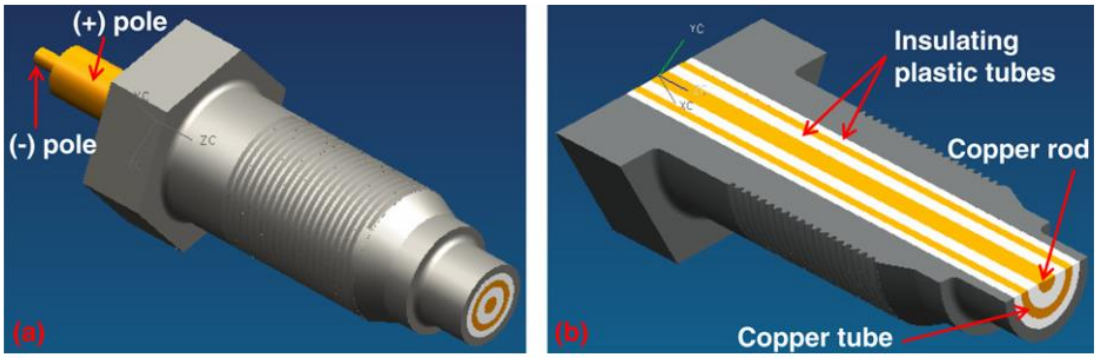

Figure 1-6: Point voltage sensor (a) and cross-section view (b) [Tuncol **2007**].

The main advantage of DC sensors lies in their simplicity of use. These easily embeddable point sensors measure the voltage drop between two points. Nevertheless, point voltage sensors lack information of the state of the surrounding part, despite the fact that some have tried to use distributed point voltage sensors [Fink **1999**] to get more information on the part, only estimations are possible. Moreover, DC sensors cannot be used with electrically conducting fibers like carbon fiber.

DC sensors have been used in UV pultrusion [Tena **2016**], but under laboratory conditions with a mold in one of the faces of the part. Using DC sensors in-process is not a viable solution. However, it is still interesting to consider the information that DC sensors can provide to improve the knowledge on the process.

1.2.1.1.5 Contact-ultrasonic

Ultrasonic (US) testing is based on the propagation of US waves in the part. US transducers convert mechanical strain into electrical signals and vice versa. Usually, US testing is based on measuring the time of flight (TOF) and attenuation of the propagated waves in usually three different ways: pulse-echo, transmission or pitch-catch.

US testing has been widely used to monitor the FRP manufacturing processes [Aggelis **2012**; Aldridge **2014**; Liebers **2012**], with set-ups like the one shown in Figure 1-7. The application of US for monitoring, mostly the curing process, focuses on the evolution of the mechanical properties during the manufacture process. Most of the work done with US has focused in contact-US testing in manufacturing processes that use closed molds. For contact-US, the transducers require a fixation pressure to ensure the correct transmission of the mechanical waves into the part. With US, it is possible to monitor both the filling and curing process of most of the FRP manufacturing processes [Konstantopoulos **2014**].

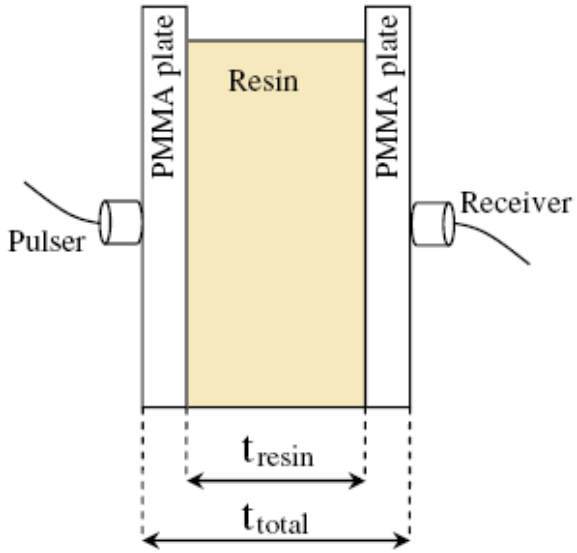

Figure 1-7: Through thickness ultrasonic measurement [Aggelis **2012**].

US technique, unlike the other techniques, provides information of the part's elastic properties. This means that apart from a qualitative evaluation of the part, it is possible to have a quantitative evaluation of its properties. This is highly interesting in order to ensure the quality of the manufactured parts. However, at the same time, US testing is usually more complex than other techniques, which is why US testing is not always used.

1.2.1.2 Contactless inspection techniques

Most of the FRP manufacturing processes are done inside of closed molds like in resin transfer molding, autoclave and even classical pultrusion. Since in the 3D-UV contact techniques cannot be used in-process, evaluating the non-contact inspection techniques is a necessity.

1.2.1.2.1 Infrared

Infrared (IR) thermometers monitor the temperature of the surface of a part. Unlike thermocouples, IR thermometers are contactless and have thermal radiation sensitive photocells to detect the thermal radiation produced by the part.

IR cameras have been used to measure the temperature in different parts during the composite manufacturing process [Cielo **1989**; Cuevas **2013**; Varnell **1992**]. These monitoring devices provide a thermal image of the surface or sub-surface of the part being manufactured, as shown in Figure 1-8. Since the temperature varies during both filling and curing, this technique provides much more information than thermocouples.

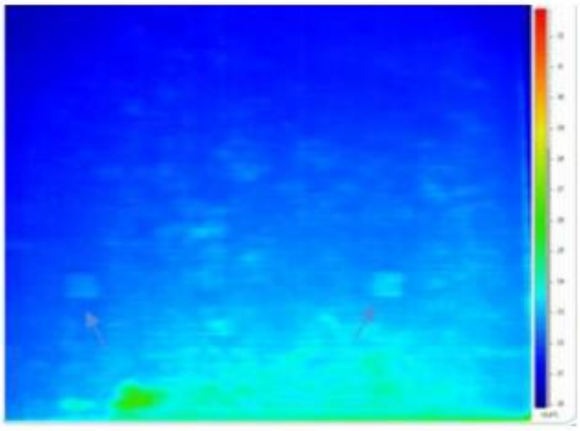

Figure 1-8: IR thermography result of an uncured carbon fiber composite plate [Cuevas **2013**].

For the processes with open mold, IR thermography can be used since there is direct vision between de part and the sensor. Yet, IR thermography is limited to superficial or sub-superficial thermal imaging. This technique is applicable in 3D-UV pultrusion as the curing is done outside of a mold, where direct vision is possible.

1.2.1.2.2 Electromagnetic

Electromagnetic (EM) monitoring includes Terahertz (THz) wave and Microwave technologies. THz, also known as Millimeter wave; and Microwave imaging are emerging NDT techniques used for dielectric (non-conducting, i.e., an insulator) materials analysis and quality control in the pharmaceutical, biomedical, security, materials characterization, and aerospace industries [Adam **2011**; Jepsen **2011**; Ospald **2013**]. Millimeter waves are set in the range of $0.1 - 10$ THz ["Terahertz wave technology" **2016**] while microwaves are in the range of $0.1 - 1000$ GHz [Kundu **2012**], even though there is no strict limit in the frequency range and this limit varies up to an order of magnitude depending on the author. EM waves have been used to monitor de curing process of composite materials [Naftaly **2007**; Sommer **2016**; Yakovlev **2015**]. An example of the set-up for the THz technique is shown in Figure 1-9.

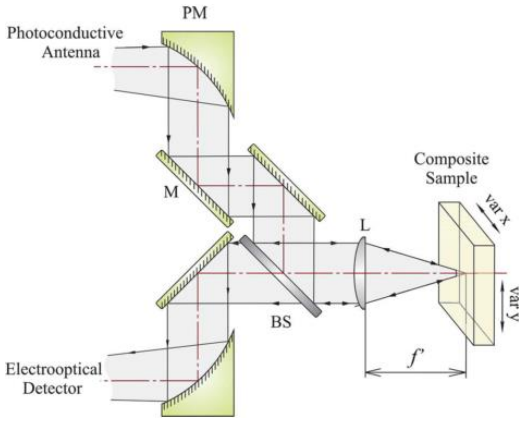

Figure 1-9: Representation of THz pulsed spectroscopy waveform detector for Polymer Composite Materials [Yakovlev **2015**].

EM monitoring can be used as a non-contact technique. It is limited to dielectric materials, except in the case of superficial monitoring or with conductive fiber materials when the polarization of the electric field and the fiber orientation are perpendicular [Li **2016**; Redo-Sanchez **2006**]. This technology is promising for its application to the manufacturing of FRPs but it is mostly limited to insulating materials.

1.2.1.2.3 NCU: ACUS

Non-Contact Ultrasonic (NCU) is a more recently developed technique than contact ultrasonics. The application of NCU is based on the generation of micro-deformations in the part without a contact between the transducer and the part. This can be done in several ways, using magnetostriction or heat to generate a wave in the material; or propagating a wave from the air into the material (this is explained in more detail in Section 1.2.3.2). ACUS is based on the latter physical concept. ACUS has been used to monitor the curing process of polymers [Lionetto **2007**a] and has showed potential for its use in non-cured FRP parts [Farinas **2012**, **2013**].

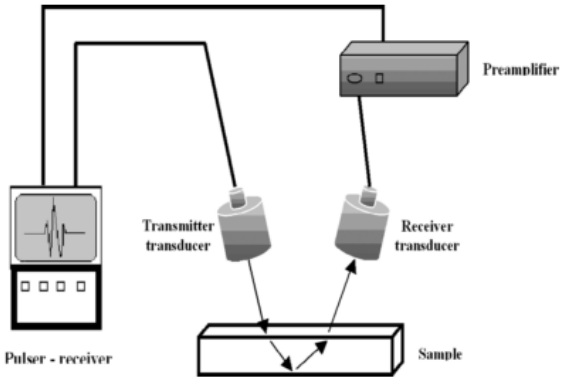

Figure 1-10: Non-contact US monitoring set-up [Lionetto **2007**b].

ACUS can be used in a similar way to contact-US, which implies that the same techniques might me applicable. The difficulty lies in coupling the wave from the air

into the material, which is more challenging than in contact-US. However, ACUS can characterize elastic properties, which is highly interesting.

1.2.1.3 Conclusion

An evaluation of the main requirements of the 3D-UV pultrusion process, concerning the different monitoring techniques, is presented in Table 1-1.

Since the 3D-UV pultrusion focuses in the curing of the material, those techniques that cannot monitor the curing do not fit process requirements. The contactless nature of the technique is also of outmost importance to apply them in the process, although–contact techniques can be used out of process to characterize the curing process. Measuring over an area has several advantages since it inspects the state of more than one point. It gives more information to evaluate the material correctly than just from a point. Lastly, measuring the mechanical properties, like Young's modulus or Poisson's ratio, of the material during the curing can ensure the quality of the manufactured part. The data on the mechanical properties could also be used as a way to certify the quality of the part meets standards.

Observing Table 1-1, EM and NCU fit the main process requirements, since are contactless, evaluate an area and can inspect inside the material. From two of them NCU stands out, since it can characterize elastic properties. This means that NCU, more specifically ACUS since it is not limited by the materials electric conductivity, shows the most potential for implementation for the 3D-UV pultrusion process.

Table 1-1: FRP manufacture monitoring techniques for 3D-UV pultrusion.

Technique	Curing	Contactless	Area	Through material	Elastic properties
Pressure	×	×	×	×	×
Thermocouple	✓	×	×	×	×
OFI	✓	×	×	✓	×
DC	✓	×	×	✓*	×
Contact-US	✓	×	✓	✓	✓
IR	✓	✓	✓	×	×
EM	✓	✓	✓	✓*	×
NCU (ACUS)	✓	✓	✓	✓	✓

* With limitations in electrically conductive materials.

1.2.2 Material characterization with US

As observed in the previous section, ACUS is the most promising technique to monitor the 3D-UV pultrusion process. Most contact-US techniques can be similarly applied in NCU, thus, it is necessary to consider them. Therefore, the characterization of the elastic properties of materials with both contact and non-contact US, and their applicability for ACUS, are evaluated in this section.

1.2.2.1 Resonant Ultrasonic Spectroscopy

Resonant ultrasonic spectroscopy (RUS) is the study of the spectra obtained by forced mechanical resonance of the samples by a swept frequency excitation. By using specimens with simple known geometry and models including specimen symmetry, resonant ultrasonic spectroscopy can determine the full elastic stiffness tensor to great precision with one measurement. There are a couple of reviews [Leisure **1997**; Migliori **2001**] that define the theoretical basis and techniques most used nowadays. There is also a review that focuses on acoustic transducers for RUS [Nakamura **2015**]. Here only some major advances in RUS are presented where the benefits and limitations of the technique are evaluated.

The first application of resonant ultrasonic, resonant sphere spectroscopy. was developed by D.B. Fraser and R.C. LeCraw [Fraser **1964**]. They showed that the elastic and anaelastic properties of solids could be measured as both a function of frequency and temperature. They excited a small sphere at different resonant frequencies and then captured the decay of the spheres vibration. The internal friction of different modes was calculated, which led to a direct calculation of the Lamé constants, λ and μ, and Poissons ratio of the isotropic solid. Yet, the method was limited to small spheres, which were not anisotropic.

Later, a rectangular parallelepiped resonance technique was developed by I. Ohno [Ohno **1976**] to characterize orthorhombic parallelepiped crystals. The accuracy of the determination of the elastic constants was determined by the initial mode identification and starting values of the elastic constants, the sensitivity of resonance frequencies to the variation of elastic constants, the shape and orientation of the specimen and the force applied to the specimen during vibration.

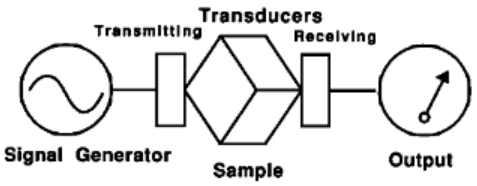

Figure 1-11: Schematic RUS setup. A rectangular parallelepiped suspended along a body-diagonal between transmitter and receiver is excited with a frequency sweep [Visscher **1991**].

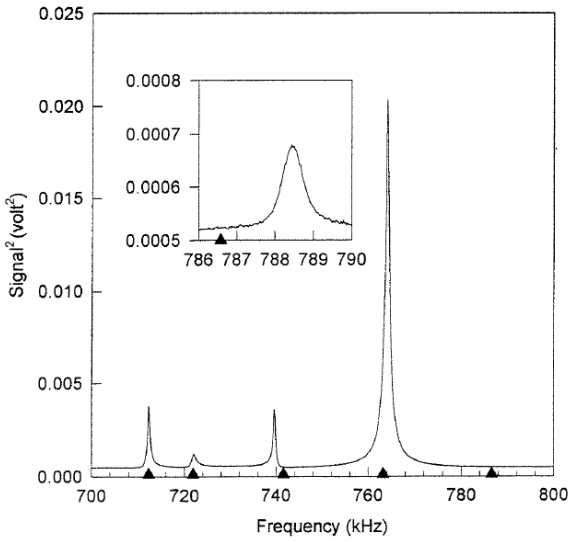

Figure 1-12: A RUS spectrum for a copper parallelepiped. The arrows indicate the computed frequencies based on a fit of the first 50 resonances [Leisure **1997**].

A. Migliori *et al.* [Migliori **1993**] developed what is today known as RUS. They previously developed and algorithm [Visscher **1991**], known as *xyz algorithm*, that computed a variety of anisotropic elastic objects, including spheres, cylinders, eggs, parallelepipeds and potatoes, which would be irregularly shaped samples. RUS allows for the determination of the full elastic tensor in a single measurement, from cryogenic to very high temperatures.

After RUS was set-out most of the research in the area has focused on [Cheeke **2017**] characterization of small samples [Migliori **2005**],characterization of samples in low [Whitney **1996**] and high [Li **2010**] temperatures, characterization of shear modes [Wang **2003**] and laser excitation and detection [Sedlák **2008**].

RUS has also been used non-contact with laser ultrasonic generators [Sedlák **2008**], to characterize elastic properties of solids based on the inversion of natural frequencies. It has also been applied with ACUS to obtain the relationship between plant leaves' elasticity and their water content [Sancho-Knapik **2012**], where it was demonstrated that the magnitude and phase spectra of the thickness resonances of plant leaves could be used to obtain the elastic constant in the thickness direction.

1.2.2.2 Through transmission

Through transmission ultrasonic material characterization is based on the measurement of the TOF and attenuation of the ultrasonic wave propagating inside a material. It has been known for a long time that the material's acoustic wave velocity (V_{ij}), in the i,j direction, was linked to the elastic tensor (c_{ij}) of the material and its density (ρ):

$$V_{ij} = \sqrt{\frac{c_{ij}}{\rho}} \tag{1-1}$$

The measurement of the longitudinal or shear wave velocity can be used to characterize the stiffness of isotropic or anisotropic materials as long as the density is known. Through transmission can be used with a single transducer in pulse-echo or multiple transducers in pitch-catch. Different variations where through transmission is used have been proposed to characterize materials, here focused in those that work in the thickness direction.

The measurements have mainly focused in contact-US due to the inherent difficulties to use NCU. These difficulties are further explained in Section 1.2.3 for NCU and Section 1.2.3.2 for ACUS. Specifically when working with a single transducer pulse-echo presents the greatest difficulty, where very scarcely has been used it been used for ACUS [Álvarez-Arenas **2019**]. The signal of the wave reflected in the external face of the material is several orders of magnitude greater than that of the inner face. Only for materials with low attenuation has pulse-echo been used [Álvarez-Arenas **2019**], which limits its use for FRP. For this reason, the works regarding the use of multiple transducers have been evaluated.

To reduce the number of measurements and the requirement of a coupling medium, different techniques have been proposed. B. Hosten *et al*. [Hosten **1987**] developed a method to characterize viscoelastic materials with ultrasonic waves transmitted through a plate shaped sample immersed in water. They applied Christoffel's equations to analyze the propagation of inhomogeneous waves in viscoelastic composite plates. They used a goniometer to precisely control the angle of the sample with respect to that of the incoming wave. Analyzing the velocities in different angles and the attenuation, they managed to measure the real and imaginary coefficients of the stiffness matrix. B. Hosten [Hosten **1991**] further developed Thomson and Haskell's plate transfer matrix for the application with isotropic viscoelastic materials, emphasizing in heterogeneous mode conversion and propagation through non-principal planes. The plate transfer matrix allows linking the top and bottoming stresses of the different layers of a plate. M. Deschamps and B. Hosten [Deschamps **1992**] presented the exact analytical formulation for the reflection and transmission of an ultrasonic plane wave by an immersed anisotropic and viscoelastic plate. B. Hosten and M. Castaings [Hosten **1993**a] modified the plate transfer matrix to introduce the heterogeneity modes generated at the interface of an absorbing medium. However, the transfer matrix method (TMM) fails at high frequency-thickness values, as it becomes unstable. M. Castaings and B. Hosten developed the delta operator technique [Castaings **1994**] which solved the high frequency-thickness value instabilities. Challis *et al*. [Challis **1993**] presented a high-frequency wideband goniometric apparatus to measure compression and shear acoustic wave velocities simultaneously. They measured several reverberations in the material. They measured the velocity in materials as aluminum, copper, ceramics and others, which showed no

attenuation. However, they stated that the attenuation should be measurable if it were significant enough. M. Lowe [Lowe **1995**] presented an ultrasonic NDT technique to monitor multilayered plates, showing how to calculate the complex bulk longitudinal and shear velocities for isotropic materials. He showed the relationship between the elastic and viscous behavior in the bulk and phase velocities and the attenuation of the propagating waves. B. Hosten *et al*. [Hosten **1996**] demonstrated that it was possible to apply the previously developed techniques to characterize materials with ACUS, using capacitive transducers as emitters and receivers. M. Castaings *et al*. developed an ultrasonic monitoring technique to characterize the complex stiffness matrix of thin plates [Castaings **2000**]. They used initially estimated valued of the stiffness, with a difference of up to 20% from the real values, and applied the simplex inversion algorithm to precisely characterize the properties of the viscoelastic plate.

1.2.2.3 Lamb waves

Lamb waves are elastic waves whose particle motion lies in the plane that contains the direction of wave propagation and the plane normal. An infinite medium supports just two wave modes traveling at unique velocities, longitudinal and shear waves; but plates support two infinite sets of Lamb wave modes, whose velocities depend on the relationship between wavelength and plate thickness. Since many FRP materials are plate-like structures, Lamb waves are of great interest for contact-US and NCU. Lamb waves can be generated in contact with glued piezoelectric disks [Dominguez-Macaya **2016**], where multiple modes can be simultaneously generated; or with a transducer with a wedge [Dominguez-Macaya **2018**], where the mode generated is dependent on the angle of the wedge. Lamb waves are specially interesting for ACUS due to the improvement in transmission efficiency [Chimenti **2014**].

Lamb waves, for NCU have been long studied. D Alleyne and P. Cawley [Alleyne **1992**] discussed the selection of the appropriate modes with NCU in water. They also showed the advantages of being mode selective and the ability to use the technique to detect flaws. M. Castaings and P. Cawley [Castaings **1996**] proved the frequency-angle relationship when using Lamb waves with ACUS. They presented for an isotropic material, aluminum, the dispersion curves of the angle-frequency relationship. That way, they presented how to be mode selective when generating Lamb waves in the plate. C. Chan and P. Cawley [Chan **1998**] demonstrated the effect of high attenuation in the propagation of Lamb wave modes. They compared plates with no attenuation, with half and with up to four times the attenuation of their original plate. In the latter case, the plate behaved as a “fluid plate”, a material that is unable to support shear motion. It showed that the velocity of some Lamb modes tended to the longitudinal wave velocity, instead of to the shear wave speed as usual. M. Castaings and B. Hosten [Castaings **2001**] analyzed the propagation of Lamb waves generated with ACUS in anisotropic materials. Experimental results showed good agreement with the analytically predicted waves, using the TMM, showing direction dependent behavior of the propagated modes. M. Castaings and B. Hosten [Castaings **2003**] analyzed the behavior of Lamb waves in viscoelastic aircraft sandwich structures. They

showed that guided modes were coupled due to the viscoelastic properties of the materials. The results were validated with FEM software. M. Castaings *et al*. [Castaings **2004**] analyzed the response of thermos-viscoelastic materials. Both complex displacements and stresses at any location in the structures were predicted and validated with FEM software. S. Dahmen *et al.* [Dahmen **2010**] developed a hybrid method to characterize the nine elastic constants of orthotropic materials. The method combines the application of TMM to characterize seven of the elastic constants, while longitudinal and shear contact measurements are used to determine the remaining two unknowns.

1.2.3 NCU: ACUS

As mentioned previously, NCU is the technique with which an US wave can be generated in a part without contact between the transducer and the part itself. This is of great interest in many cases, like for the 3D-UV pultrusion. There are many ways to generate the US wave without contact, from different mediums like water or air. In the 3D-UV pultrusion, only air is usable, since the samples cannot be placed under water. Thus, NCU in air needs to be evaluated.

1.2.3.1 Generation of ultrasonic waves in solids with NCU transducers

Since NCU has been used for material testing or characterization, generating the US wave in the material without contact has been one of the greatest challenges for scientists and engineers [Chimenti **2014**]. This can be achieved in two ways: generating the US wave directly in the part or propagating an US wave through the coupling medium, usually water or air, into the part. The generation of US ways directly in the part can be achieved with two technologies: EM US generation and Laser US.

If the part is electrically conductive or ferromagnetic, direct electromagnetic generation of ultrasonic in the part can be achieved [Thompson **1990**]. Electromagnetic acoustic transducers (EMAT) generate ultrasonic waves in the part with two interacting magnetic fields, as shown in Figure 1-13 (a). A rapidly changing magnetic field will generate eddy currents over the conductive surface, whilst a static magnetic field will generate Lorentz forces in the part, leading to a net mechanical displacement of the lattice ions. For ferromagnetic materials, additional interactions can occur [Thompson **1990**]. The use of EMATs in conductive materials is delicate and depends on many favorable properties, which makes the application limited [Chimenti **2014**]. Furthermore, EMATs require high electrical conductivity in the part, favorable part geometry and powerful magnetic fields, which can cause interferences in other devices. When all of the requirements are meet, EMATs qualify as NCU transducers [Chimenti **2014**].

Laser US (LUS) is the rapid surface deposition of heat with a high energy density [White **1963**], as shown in Figure 1-13 (b). If the surface of a body is subjected to transient heating (e.g., by electron bombardment or EM absorption) elastic waves are produced as a result of surface motion due to thermal expansion. Typically, a high-power pulsed laser (often a Q-switched Nd:YAG laser) [An **2013**; Sedlák **2008**], with a

small diameter focused beam at the material surface, is used as heating source. As the deposited energy is substantial and the area small with a short deposition time, energy density is very large. However, due to high thermal energies, it is a concern that these may be high enough to evaporate and melt the surface of the material. This process is called ablation and it is completely undesirable, as it would render NDT as no more non-destructive.

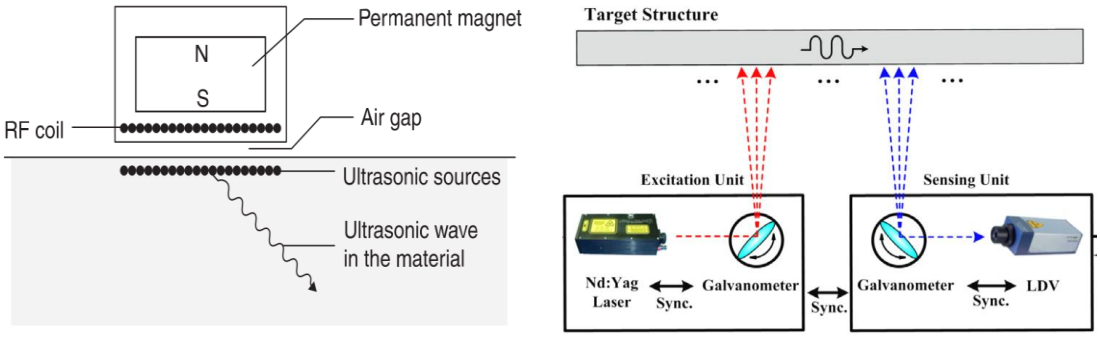

(a) (b)

Figure 1-13: (a) EMAT transducer [Nakamura **2012**] and (b) LUS wave generator and receiver [An **2013**].

Propagating the wave from a coupling medium, without contact, is usually done with water or air. Since water is not always a viable option due to the requirement to sink the part, air is the only choice. Air is advantageous since it is present everywhere, there is no need to carry it or be kept it in a closed environment. However, air presents some disadvantages that other fluids carry, like the inability to propagate shear waves, plus several of its own, like the frequency range limitation of 1.5 MHz. However, unlike the previous technologies, ACUS can be used for non-conductive materials and does not carry the risk of damaging the part.

1.2.3.2 ACUS

As mentioned previously, ACUS is the technology were the US measurements are carried out propagating the waves from the air into the part and from the part into the air back. The transmission between media, air and the part, is one of the main issues of ACUS. This issue comes from the acoustic impedance (Z) mismatch that exists between the air and the solid materials, either the transducer that is generating the wave or the part. When a pressure wave propagating in the air comes across a solid material layer the amount of energy that gets into the solid is usually very low. This can be observed calculating the acoustic transmission coefficient (T) [Krautkrämer **1990**] between the boundaries of air (acoustic impedance Z_{air} of 515 Rayl) and a glass fiber reinforced polymer (GFRP) [Performance Composites Inc. **2017**] (acoustic impedance Z_{GFRP} of around 3.5 MRayl) with the following equation:

$$T = \frac{4Z_{air}Z_{GFRP}}{(Z_{air} + Z_{GFRP})^2} \quad (1\text{-}2)$$

The transmission coefficient is around 0.059%, which means that 99.941% of the energy that is traveling through the air is reflected at the GFRPs boundary. That is a single boundary and there are usually four boundaries in the system: transducer-to-air, air-to-part, part-to-air and air-to-transducer; the transmission is greatly reduced. There are techniques that improve the transmission efficiency between the plate and the air, like RUS (Section 1.2.2.1) and Lamb waves (Section 1.2.2.3). It is also possible to improve the transmission between the transducer and the air.

1.2.3.2.1 Transducers

Amongst ACUS transducers, the most popular are piezoelectric [APC International **2002**; Cobbold **2006**; Iriarte **2010**; Wilson **1988**; Wong **2002**], capacitive [Caronti **2006**; Schindel **1995**] and thermoacoustic transducers [Gaal **2016**a, **2016**b]. Their popularity relies on their ease of use, cost and availability.

Piezoelectric transducers are composed of four sections, shown in Figure 1-14:

- The active material is the part of the piezoelectric transducer that converts the electrical signal into mechanical deformation and vice versa. Most common used materials are piezoceramic [Nakamura **2012**], polyvinylidene fluoride [Cobbold **2006**], piezocrystal [Iriarte **2010**] or piezocomposite [Bernassau **2009**].
- The matching layer increases the transduction of mechanical waves between the active material and the propagation medium. It does so by reducing the acoustic impedance mismatch between the active material and the air.
- The backing layer reduces wave reflections from the opposite side of the active material. It shortens the pulse length, which improves the axial resolution of the measurements. The material should have an acoustic impedance equal to the active material but high attenuating to avoid reflections.
- The encapsulation is usually made out of rigid and electrically conductive materials. This is to both protect the inner delicate parts of the transducer and provide electric and EM isolation.

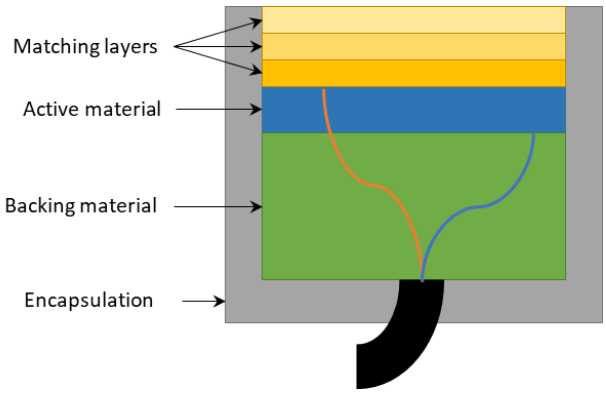

Figure 1-14: Piezoelectric transducer schematic.

Capacitive micomachined transducers (CMUT), Figure 1-14, is a type of US transducer that relies on the capacitive effect between conducting layers. CMUTs are built on silicon with micromachining techniques. The CMUTs consists of a thin flexible plate suspended over an air cavity. A thin metal layer on top of the transducer with an insulating foam between the contoured backplane and the upper electrode. When an alternating current is induced into the conductive capacitance, there is a variation in the distance between plates, which generates an acoustic wave. The air cavity, acts as a natural spring, which reduces significantly the impedance mismatch [Schindel **1995**]

Figure 1-15: CMUT schematic.

Thermoacoustic transducers transform thermal energy fluctuations into sound. They achieve acoustic wave generation by direct application of an electrical signal and without the use of any moving components. A thermoacoustic transducer causes local vibration of air molecules resulting in a proportional pressure change. Since there is no boundary from the place where the wave is generated to the air, the mismatch is reduced. Moreover, the thermoacoustic transducers do not resonate, which means that the generated acoustic pattern, like a single short pulse, is generated instead of larger resonating one. On the bad side, thermoacoustic transducers have only been used as transmitters and not receivers.

There are also other kind of transducers, which are called laser microphones or optical microphones [Fischer **2016**]. These transducers are quite new and at least an order of magnitude more expensive than the previous ones. Optical microphones have a much high sensitivity, since they apply laser US technology to detect the signal. These transducers, however, can only work as receivers and are known to pick noise from all of the directions.

Apart from the different technologies of transducers, the use of array transducers can be widely advantageous. They can be used to either control the focal distance electronically, instead of geometrically; or to control the direction of the generated wave [Farinas **2012**]. Moreover, they could be used to measure the phase velocity of Lamb waves in a fast way [Farinas **2012**]. However, nowadays there are nearly no ACUS transducer arrays due to the large wavelength of ultrasound in the range under 1 MHz. The size of the transducers is inversely proportional to the frequency. The active

elements of the array need to be at a distance of less than half a wavelength of each other, to ensure grating-lobe free beamforming. With use of waveguides this can be achieved at low (40 KHz) frequencies [Jager **2019**].

1.3 Critical assessment of the state of the art

Monitoring the manufacturing of FRP processes has shown to be of great interest for the industry. Much effort has been put in different monitoring techniques, each of them shows advantages and disadvantages in its application. The techniques that make punctual measurements are often the simplest to use and cheapest. However, they also provide with the fewest information. They can measure one or more points of the parts, with distributed sensors, but can only estimate the rest. The techniques that provide information on the status of the materials over an area usually require more complex systems, electronics and signal processing. These techniques can be non-contact, meaning that they usually require some sort of direct vision between the part and monitoring system. This can be done through a transparent mold or without any physical media in between.

In the case of 3D-UV pultrusion, the process itself limits the capability of using contact-monitoring techniques. Monitoring based on both EM waves and ACUS have shown the greatest potential for applications like 3D-UV pultrusion. EM waves are limited to be used in non-conductive materials and cannot determine the elastic properties of the material. ACUS has shown drawbacks, compared to EM waves, due to the difficulty to couple the wave from the air into the composite. However, ACUS gives the possibility to monitor the process and characterize the material at the same time. Due to that, ACUS is the technique with the highest potential.

ACUS presents drawbacks coupling waves between the air and composite, but this drawback is not only limited to air and composite. This coupling mismatch is also present in the transducers that propagate the wave into the air. Selecting the right technology of transducer is critical to ensure that the energy is transmitted from the transducer into the air. Piezoelectric and capacitive transducers can be used as emitter and receiver, which is advantageous, and is innocuous for the material, contrary to LUS generators. Particularly piezocomposite transducers have been observed to have a wide frequency range and efficiency.

Another focal point in ACUS monitoring, as for the manufacturing process, is the temperature variation due to the cure. The curing process heats not only the part but also the surrounding air. The variation of the temperature in both elements needs to be measured, to ensure the reliability of the measurements.

ACUS has shown great applicability in material characterization and defect detection. Materials with isotropic, orthotropic and other kind of anisotropy types have been characterized with high precision using the air as a couplant. It is clear, however, that even though impedance mismatch has been reduced with the use of proper

transducers and appropriated techniques, measurements in ACUS require high precision and sensitive electronics.

Several techniques for the characterization of materials with US have been developed. Most of the techniques allow obtaining the materials stiffness and viscosity. Techniques with contact and non-contact have been developed, with good results, even despite non-contact impedance mismatch limitations. The techniques that apply direct transmission through the material were first developed, but in non-contact, this carries limitations. Inspecting through the material cannot always be applied as the process may require one sided access or have two layers of material separated by air. That is, the part may have a closed, such as circular or hexagonal geometry, where three layers of air and two material layers would separate the transducers.

In the process of 3D-UV pultrusion the likelihood of manufacturing such parts is high, therefore, limiting that application. The 3D-UV pultrusion process, due to its own characteristics, manufactures long and plate-like geometries, curing out of a mold. This leads to show that the application of Lamb wave monitoring techniques are the most appropriate ones.

However, in composite manufacturing processes, not much effort has been put regarding ACUS. This may probably be due to the fact that most manufacturing processes use a mold or a bag, or other kind of surrounding structure. These structures prevent the use of ACUS, as contact techniques make much more sense.

Therefore, in order to monitor the curing process with ACUS, at the time little work has been done. The few work that have been done have focused on monitoring the curing of resin matrixes, characterizing the material in some defined curing moments and proving the viability of the technique.

1.4 Objectives

The main objective of the thesis is to evaluate the properties of composite materials during the UV pultrusion manufacturing process. To do this, the work has focused on three sections: evaluation of the isotropic viscoelastic properties of the resin matrix during the UV curing, evaluation of the properties of a curved geometry manufactured with the 3D-UV out-of-die pultrusion curing process and the evaluation of the anisotropic elastic properties of the GFRP during the thermal curing. To achieve this objective, several operative objectives have been defined:

- To evaluate the monitoring techniques that can show applicability for the FRP manufacturing processes.
- To evaluate the use of fast simultaneous measurements of the viscoelastic properties of resin during the UV curing process.
- To analyze the variation of elastic properties of anisotropic materials during the thermal curing process.

- To analyze the effect of the curvature in the evaluation of anisotropic properties of 3D-UV pultruded profiles.

1.5 Outline of the thesis

The remainder of this document is organized as follows:

In Chapter 2 a fast ACUS quasi-normal resonant spectroscopy monitoring process for UV curing of polymers based on is presented. In Chapter 3 a comparison of the evaluation of straight and curved GFRP profile properties is presented. In Chapter 4 an ACUS based on LLW to obtain the elastic properties of a GFRP plate during the thermal curing is presented. Finally, Chapter 5 summarizes the work done and the main conclusions obtained, as well as the future lines that can serve to complete and expand the work presented in this doctoral thesis.

1.6 Publications

The following papers have been published or are under preparation for publication in refereed journal and conference proceedings. Those marked by † correspond to a contribution included in this thesis.

Journal Paper:

- A. Dominguez-Macaya, T.E.G. Álvarez-Arenas, I. Saenz-Domínguez, I. Tena, J. Aurrekoetxea, A. Iturrospe. Monitoring the evolution of stiffness during ultraviolet curing of a vinyl ester resin with quasi-normal air-coupled ultrasonic spectroscopy. Polymer Testing (2019), volume 80.

Conference papers:

- A. Dominguez-Macaya, I. Saenz-Dominguez, J M Abete, J Aurrekoetxea, A Iturrospe. In process ultrasonics inspection method for ultraviolet (UV) out of die curing pultrusion process. XII European Conference on Non-Destructive Testing (ECNDT2018), Gothenburg, Sweden.
- A. Dominguez-Macaya, T.E.G. Álvarez-Arenas, I. Saenz-Domínguez, I. Tena, J. Aurrekoetxea, A. Iturrospe. Monitorizado de la evolución de la rigidez durante el curado ultravioleta mediante ultrasonidos con acoplamiento por aire. XIII Congreso Nacional de Materiales Compuestos (MATCOMP2019), Vigo, Spain.
- A. Dominguez-Macaya, M. Gaal, T.E.G. Álvarez-Arenas, J. Aurrekoetxea, A. Iturrospe. Air-coupled ultrasonic testing with Lamb waves for straight and curved GFRP plates. 2019 International Congress on Ultrasonics (ICU2019), Bruges, Belgium.

Chapter 2

Monitoring the UV curing of a vinyl ester resin with ACUS

One of the main objectives of this thesis is to evaluate the evolution of the viscoelastic properties of the resin during the UV curing. Therefore, in this chapter the evolution of the viscoelastic properties of a vinyl ester (VE) during the UV curing with quasi-normal ACUS resonant spectroscopy is analyzed. These viscoelastic properties are compared with the degree of curing (DoC) estimations based on DC sensor measurements. The first section of this chapter presents the theoretical background over the acoustic longitudinal and shear properties; and the mechanical longitudinal, shear, Young's modulus and Poisson's ratio are obtained. The second section presents the set-up and methodology used in this analysis. The third presents the results of the measurements whilst the fourth one shows the conclusions obtained from this analysis.

2.1 Theoretical background

2.1.1 Single-layer normal plane wave

The acoustic properties of a transmitted US wave in a plate surrounded by a fluid can be evaluated with the use of resonant ultrasonic spectroscopy [Álvarez-Arenas **2010**]. In the simplest case, a non-attenuating fluid, air, surrounds a single-layered plate where a plane wave is incident to the plate in a normal angle with respect to the surface. The transmission coefficient (TC) of this plane incident wave in the plate can be obtained using the following expression [Álvarez-Arenas **2010**]:

$$TC = \frac{2Z_f Z_s}{2Z_f Z_s \cos(k_l d) + i\left(Z_f^2 + Z_s^2\right)\sin(k_l d)} \tag{2-1}$$

whereZ_f and Z_s are the acoustic impedances of the air and the plate respectively; k_l is the wavenumber of the longitudinal wave in the plate and d is the thickness of the plate.

Evaluating the TC over a range of frequencies provides the frequency response of the plate to the plane wave propagating in the air (named as TC spectrum from now on). The TC spectrum is dependent on the acoustic longitudinal wave properties of the plate, the longitudinal velocity and attenuation, as well as the density of the plate. The acoustic longitudinal wave properties and density of the plate can be evaluated as proposed by Alvarez-Arenas [Álvarez-Arenas **2003**], even when the thickness of the plate is not previously known. Once the TC spectrum is obtained, the thickness of the plate is estimated from the phase of the transmitted pulse at the resonance frequency.

Once the thickness is known, the longitudinal velocity is estimated from the resonance frequency of the plate. The longitudinal attenuation is estimated from the Q-factor of the resonance peak and the reflection coefficient at the fluid-solid boundary. With these initial estimations of the longitudinal acoustic properties, values close to the real ones are obtained. To improve the precision of the estimated longitudinal wave properties, the measured TC spectrum is fitted with the theoretical one from Eq. (2-1). The acoustic properties of the experimental and theoretical model are fitted through a stochastic gradient descent algorithm [Álvarez-Arenas **2003**]. From the calculated acoustic longitudinal properties, the mechanical longitudinal modulus can be obtained, as is later explained in Section 2.1.3.

To obtain the mechanical properties of the plate that are usually of greatest interest (Young's modulus, shear modulus and Poisson's ratio) it is necessary to work in non-normal incidence angles [Fariñas **2013**]. The TC of a plate is no longer defined as in Eq. (2-1), since it does not support shear wave propagation nor is dependent on incidence angle.

2.1.2 Multi-layer non-normal plane wave transmission

When a plane wave is incident on a single layer or multilayered solid plate at an oblique incidence, as depicted in Figure 2-1, both longitudinal and shear waves are generated in the plate. To calculate the TC of an N-layered system the stresses and displacements at the interfaces need to be related as follows [Thomson **1950**]:

$$\begin{bmatrix} \xi_n \\ \zeta_n \\ \sigma_n \\ \tau_n \\ \hline 2G_n \end{bmatrix} = \begin{bmatrix} a_{11} & a_{12} & a_{13} & a_{14} \\ a_{21} & a_{22} & a_{23} & a_{24} \\ a_{31} & a_{32} & a_{33} & a_{34} \\ a_{41} & a_{42} & a_{43} & a_{44} \end{bmatrix} \begin{bmatrix} \xi_{n-1} \\ \zeta_{n-1} \\ \sigma_{n-1} \\ \tau_{n-1} \\ \hline 2G_{n-1} \end{bmatrix} \tag{2-2}$$

where ξ and ζ are the particle displacements in the surface and thickness direction at the boundaries, σ and τ are the normal and shear stresses respectively, and G is the shear modulus. The subscript n defines the layer's lower boundary, the $n-1$ defines the upper boundary and the expressions for the matrix elements, $a_{11}, a_{12}, \dots a_{44}$ are obtained from the layer properties.

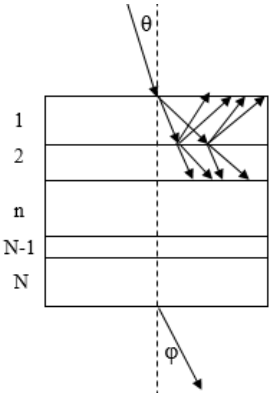

Figure 2-1: Plane-wave transmission in a multilayered plate.

The continuity of particle velocities and stresses at the interface of each n-layer allows defining the N-layer multilayer system as:

$$\begin{bmatrix} \xi_N \\ \zeta_N \\ \sigma_N \\ \tau_N \\ \hline 2G_N \end{bmatrix} = \prod_{n=1}^{N} [A]_n \begin{bmatrix} \xi_0 \\ \zeta_0 \\ \sigma_0 \\ \tau_0 \\ \hline 2G_0 \end{bmatrix} \tag{2-3}$$

where the elements of each of the $[A]_n$ layers are obtained as in Eq. (2-2). Applying boundary conditions to Eq. (2-3) the TC of the multilayered plate can be obtained [Álvarez-Arenas **2003**].

When the TC spectrum is evaluated for oblique incidence, the effect of the shear wave resonance over the longitudinal resonance can be observed [Álvarez-Arenas **2002**], this can be observed later in the results in Figure 2-3 (a). If the angle of incidence is close to normal angle with respect to the surface of the plate, the interference of the shear wave resonance with the longitudinal resonance can be observed. This interference in the spectrum, according to Thomson [Thomson **1950**], is composed of a local maxima and minima, and is dependent on the shear velocity and attenuation [Madigosky **1979**] :

$$c_s = \frac{f_{s_{res}} d}{m} \tag{2-4}$$

$$\alpha_s = (\alpha_l/2)(c_l/c_s)^3 \tag{2-5}$$

where c and α are the longitudinal (subscript l) and shear (subscript l) velocities and attenuations respectively, $f_{s_{res}}$ is the frequency in the centre of the local maxima and minima of the interference and m is the resonance order. An example can also be observed later in the results in Figure 2-3 (a).

Once the TC is calculated, as in the normal single layer plate case, it is necessary to make an initial approximation of the values of the acoustic properties of the

multilayered plate. Since the acoustic properties are composed of the longitudinal and shear velocities and attenuations of each of the layers, one way to approximate the acoustic properties is to consider the multilayer system as a single layer [Álvarez-Arenas **2018**]. With the initial estimation as a single layer, the properties of each of the layers can be simultaneously fitted with the multilayer model. If the layers cannot be separated, this is the best procedure. Another way to approximate the acoustic properties is to make independent measurements of each of the layers of the multilayer material. If it is possible to separate the layers, the initial estimations should be closer to the real values than with the previous method. Once the initial estimations of the acoustic properties have been carried out, the experimental TC spectrum can be fitted as in the multilayer case to obtain the correct acoustic properties.

2.1.3 Relationship between the acoustic and mechanical properties

The determination of the density and the mechanical viscoelastic properties like Young´s modulus and Poisson's ratio, as well as the loss tangent, is based upon the relationship between the acoustic and the mechanical properties for isotropic viscoelastic materials [Álvarez-Arenas **2010**; Qiao **2011**]. To obtain the density of the material, the transmission coefficient at the minimum transmission point T_{min}, where the thickness resonance has the least effect, is evaluated:

$$T_{min} = \frac{4Z_p^2 Z_a^2}{\left(Z_p^2 + Z_a^2\right)^2} \tag{2-6}$$

where $Z = \rho c_l$ for the plate (subscript p) and air (subscript α), and ρ and c_l are the density and longitudinal wave velocity of the plate and the air.

For viscoelastic solids, Young's modulus and Poisson's ratio are defined as complex mechanical properties, where the real part corresponds to the elastic behavior and the imaginary part corresponds to the viscous behavior. To calculate Young's modulus and Poisson's ratio, the complex viscoelastic longitudinal (L^*) and shear (G^*) modulus need to be calculated. The longitudinal viscoelastic modulus is related to the longitudinal acoustic velocity and attenuation, while the shear viscoelastic modulus is related to the shear acoustic velocity and attenuation. As the relationship of both L^* and G^* with their respective longitudinal and shear acoustic properties is identical, the modulus M^* in Eq. (2-7) and (2-8) can be substituted by either L^* or G^* [Qiao **2011**]:

$$M^* = M' + M'' \tag{2-7}$$

$$M' = \frac{\rho_s c^2\left(1-\left(\frac{\alpha c}{\omega}\right)^2\right)}{\left(1-\left(\frac{\alpha c}{\omega}\right)^2\right)^2} \text{ and } M'' = \frac{2\rho_s c^2\left(\frac{\alpha c}{\omega}\right)}{\left(1-\left(\frac{\alpha c}{\omega}\right)^2\right)^2} \tag{2-8}$$

M′ is the longitudinal or shear storage modulus, and M′′ is the longitudinal or shear loss modulus. It can be observed from Eq. (2-8) that the acoustic velocity and

attenuation are directly related to the viscoelastic properties. From the complex viscoelastic longitudinal and shear modulus, the bulk modulus K^* and Young's modulus E^* can be calculated [Qiao **2011**]:

$$K^* = K' + iK'' \text{ where } K' = L' - \frac{4}{3}G' \text{ and } K'' = L'' - \frac{4}{3}G'' \quad (2\text{-}9)$$

$$E^* = \frac{9K^*G^*}{3K^* + G^*} \quad (2\text{-}10)$$

Poisson's ratio for linearly viscoelastic materials ν^* is defined as follows [Tschoegl **2002**]:

$$\nu^* = \frac{3K^* - 2G^*}{2(3K^* + G^*)} \quad (2\text{-}11)$$

However, shear wave propagation in the liquid resin is will take place with a very low velocity and a very high attenuation coefficient. These features imply that Poisson's ratio will be very close to 0.5, imaginary parts will be large and that the influence of shear waves on longitudinal transmission will be much reduced. In the curing process, the liquid resin will only be liquid until the gelation point, where shear wave attenuation will be dramatically reduced [Lionetto **2013**] and the properties related to shear waves can be measured.

2.2 Set-up and methodology

To estimate the properties of the VE resin and polycarbonate (PC) the set-up shown in Figure 2-2 was built. Two broadband transducers were aligned in a quasi-normal incidence angle (3º) with the sample between them. The US transducers were piezo-composite unfocused transducers made at the Consejo Superior de Investigaciones Científicas (CSIC) with a working range from 400 kHz to 800 kHz [US-Biomat **2015**]. In order to drive the transducers, the signal generator of a PicoScope5000 and a Falco WMA-300 amplifier were used to generate a tone burst of 600 kHz - 200 $V_{peak\text{-}to\text{-}peak}$ with 10 square pulses. At the receiving side, a Femto HQA-15M-10T charge amplifier with 10 V/pC gain and the oscilloscope of the PicoScope5000 were used to register the signals.

To monitor the cure, a PC plate with 1.9 mm thickness was placed under the VE resin to sustain it during the liquid state. The mechanical and acoustic properties of the PC plate, measured in Section 2.3.1, are 1210 kg/m3 density and 2125 m/s longitudinal velocity, which are close to those of the VE and other resins, around 1000-1200 kg/m3 density and 1500-2500 m/s longitudinal velocity [Lionetto **2007**b]. The similarity in these properties enhances acoustic transmission between layers, thus making the choice of this material adequate.

The resin used in the experiment was a UV curable VE supplied by Irurena S.A (IRUVIOL GFR-17 LED). To cure the polymer, a UV light source (Phoseon Fire Flex)

with 395 nm wavelength and 1.6 W/cm^2 power density, was placed obliquely to the sample (60º). Despite the oblique irradiation, the intensity over the incident area in the sample was assumed as homogeneous. With the UV light, curing is done from top to bottom. Therefore, to ensure a homogeneous cure along the thickness a sample of 1.9 mm thickness was manufactured. Additionally, reducing the thickness, the bulk effect and the temperature gradient generated by the exothermic nature of curing are reduced, resulting in higher accuracy measurements.

To monitor the DoC, an Optimold DC sensor (Synthesites Innovative Technologies Ltd.) was placed in contact with the resin. The DC technique has been proven to be able to monitor the UV curing of polymers and their composites [Tena **2016**]. The DC sensor was placed at the same distance as the ACUS transducer with respect to the UV light to ensure equal curing degree at the measured area. Two pairs of thermocouples were also placed. A pair in contact with the upper and lower part of the PC plate ($T_{PC\text{-}VEthin}$ and $T_{PC\text{-}Air}$ in Figure 2-2) to monitor the temperature. The other pair (T_{AirUp} and $T_{AirDown}$ in Figure 2-2) were placed 30 mm away from the face of the VE and the PC. The measurements of the DC was registered using an Optimold software and the measurements of the thermocouples using a DAQ9219.

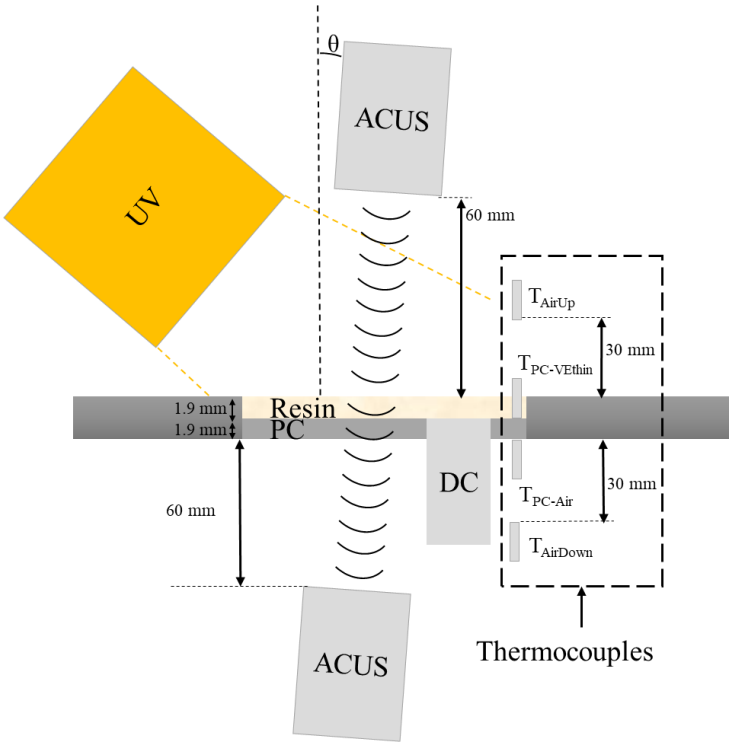

Figure 2-2: Set-up to monitor the UV curing process with ACUS.

To evaluate the acoustic properties, the transmitted ultrasonic signal was measured without neither the PC nor the VE layer. This signal was used as a reference of the frequency response of the system, which includes the electronic equipment, the transducer and the air between them. The US transmitted signal was later measured with the layer or layers between the transducers. For the signal of the system and the signal

transmitted through the layers, a discrete Fourier transform (DFT) (by a fast Fourier transform (FFT) algorithm) was carried out. The DFT response of the system without layers was used as a reference and compared with the DFT with the plates [Álvarez-Arenas **2003**]. This comparison provides the frequency response of the layers only, eliminating the effect of the equipment used and the air. This evaluation was done for three scenarios: before curing, during curing and after curing. In each of these three scenarios a total of four tests were carried out, with a single measurement of the system.

Before curing, two tests were carried out where each material, VE and PC, were characterized separately. In the first test, the 1.9 mm PC plate was characterized in order to obtain the parameters of the PC. In the second test, a 5.92 mm liquid VE (named as VE_{thick} from now on) was characterized. Since the liquid VE_{thick} resin requires a solid layer to hold it, a 0.1 mm PC was placed under the VE_{thick}. The choice of a thicker resin layer in combination with a thin PC plate is adopted to make an approximation of a single layer material. However, the properties calculated for the VE_{thick} as a single layer were later recalculated during curing, using these measurements as an initial approximation.

During curing, the 1.9 mm PC plate and a 1.9 mm VE (named as VE_{thin} from now on) were measured as a bilayer material. The choice of a 1.9 mm PC, instead of the 0.1 mm one, is adopted to thicken the sample and ensure that at least one resonance of the bilayer system is inside the bandwidth of the transducers. The properties estimated before curing were used as initial parameters. The thickness of the VE_{thin} and the elastic properties were measured as a bilayer system before turning the UV light on. The properties were estimated in three phases. First, the thickness during curing was evaluated. Second, the temperature variation in the PC and air was considered to reduce de error in the measurements. Last, the viscoelastic properties of the VE_{thin} resin during curing were finally evaluated taking into account the previous thickness and temperature conditions.

After curing, the VE_{thin} plate was removed from the PC supporting plate and its thickness and properties were measured at room temperature in the same fashion as before curing.

2.3 Results

2.3.1 Characterization before curing

The TC spectrum of the PC and the VE_{thick} were evaluated before curing. Figure 2-3 shows, for both materials, the measured TC spectrum, the initial estimation and the final estimation after fitting the curves with the resonance model. Figure 2-3 (a) shows the TC spectrum for the PC and Figure 2-3 (b) for the thick VE_{thick}. In Figure 2-3 (b), the VE_{thick} shows two resonance peaks at 520 kHz and 651 kHz, which are the fourth and fifth resonances respectively. The order of the resonance peak in the VE_{thick} can be calculated since the resonance frequency is repetitive in equidistant frequency hops,

131 kHz in the case of VE_{thick}. In Figure 2-3 (a), the PC only shows one resonance peak at 559 kHz, which is the first one. The maximum TC of the VE_{thick} and PC are also different, with -44 dB and -46 dB at their respective resonances. Since a 0 dB TC in the resonance frequencies would mean that the material is non-attenuating, the higher TC of the VE_{thick} implies that its longitudinal wave attenuation is lower that of the PC. The minimum TC in the VE_{thick} is at 590 kHz, whilst it is not visible in the PC TC spectrum, as it is out of the frequency range of the transducers. However, a lower minimum value in the TC of either material would mean a higher acoustic impedance mismatch, which is related to a higher velocity or density. The phase of the VE_{thick} is higher than that of the PC at their first visible resonance. The higher phase indicates either a lower velocity or a thicker sample in the VE_{thick}. The PC presents at the TC spectrum and phase an interference, which is caused by the shear waves, unlike the VE_{thick}. This interference, at 475 kHz in Figure 2-3 (a), is encircled in yellow and is composed of a local minima and maxima in the TC. The position of this interference, to the left of the first resonance of a single layer PC, indicates that the shear wave velocity is under half the velocity of the longitudinal waves.

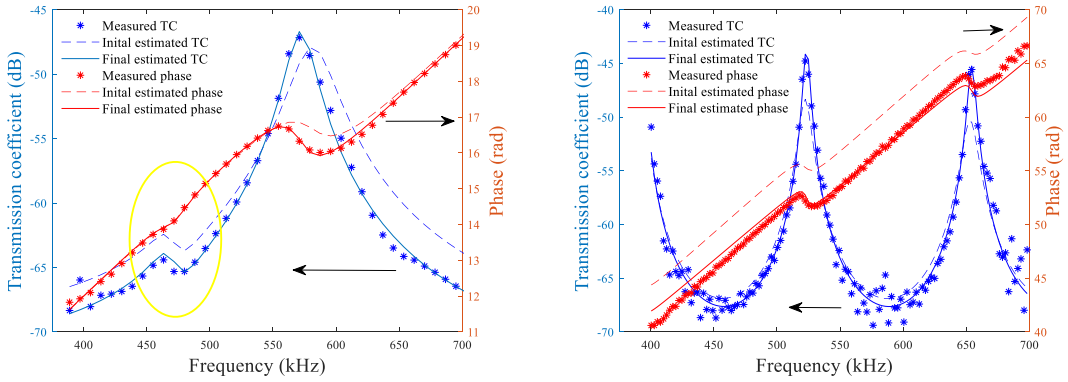

Figure 2-3: Frequency response of the PC plate (a) and the VE_{thick} plate (b).

The acoustic properties, as well as the thickness, of both the PC and VE_{thick} are shown in Table 2-1. The estimated thickness for the PC with ACUS is within the range measured with a micrometer. The longitudinal velocities for both the VE_{thick} and PC are in the expected range for those materials [Asay **1967**; Lionetto **2007**b; Selfridge **1985**]. The longitudinal attenuation, normalized to 1 Hz, and shear velocity of PC also fit the expected ones [Asay **1967**; Selfridge **1985**].

Table 2-1: Extracted acoustic properties before curing.

Material	Thickness estimated (mm)	Thickness measured (mm)	Longitudinal velocity (m/s)	Shear velocity (m/s)	Longitudinal attenuation (dB/m)	Shear attenuation (dB/m)
PC	1.9	1.88 ± 0.05	2125	897	$440 \cdot 10^{-6}$	$1.96 \cdot 10^{-3}$
Liquid VE_{thick}	5.92	-	1572	-	$223 \cdot 10^{-6}$	-

The mechanical properties of the PC and the VE_{thick} are reported in Table 2-2. The values obtained for the PC are within the expected range [Asay **1967**; Selfridge **1985**]. The viscous properties on either the VE_{thick} or the PC could not be compared to data in bibliography. Moreover, the viscous properties of the Poisson's ratio shown in Table 2-2 are completely elastic, as it was zero up to three significant figures.

Table 2-2: Extracted mechanical properties before curing.

Material	Young's modulus (GPa)	Shear modulus (GPa)	Bulk modulus (GPa)	Poisson's ratio	Density (kg/m^3)
PC	2.67 + 0.33i	0.96 + 0.12i	4.11 + 0.2i	0.39	1210
Liquid VE_{thick}	-	-	2.77 + 0.07i	0.5	1124

2.3.2 Characterization during curing

2.3.2.1 Variation of the thickness of VE_{thin}

Knowing the thickness of the VE_{thin} resin during curing is critical to ensure the precision of the properties estimated for the resin [Álvarez-Arenas **2003**]. Before the UV light is turned on, and the exothermic cure reaction begins, the thickness of the VE_{thin} resin can be simply estimated as in Section 2.1.1. Once curing is finished the final thickness of the VE_{thin} resin can be measured as previously and validated with a micrometer. During curing, estimating the thickness by ACUS requires accurate values of the surrounding air temperature and PC properties, and with the current set-up, it is not possible. Thus, in order to overcome this difficulty, the thickness of the VE resin is estimated assuming that the chemical shrinkage of the resin is proportional to the DoC [Antonucci **2002**] measured by de DC sensor. Figure 2-4 shows the evolution of the DoC registered by the DC sensor and the estimated thickness of the VE resin layer during curing.

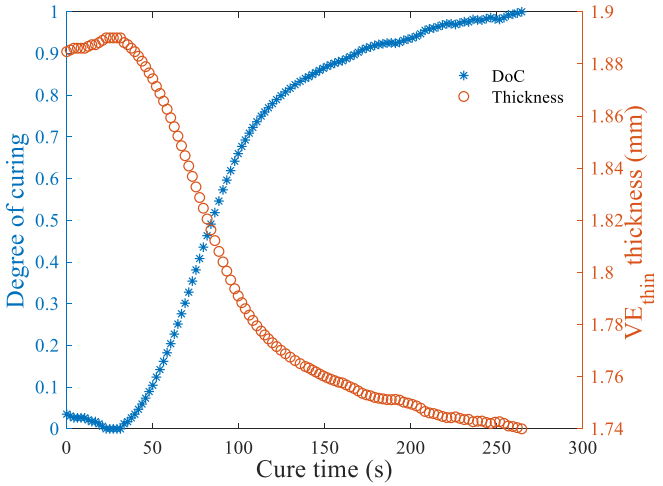

Figure 2-4: Thickness of the VE_{thin} with the DoC.

2.3.2.2 Variation of the properties of PC

The exothermic nature of the curing of VE resin modifies the temperature of the PC plate and, consequently, the effects of this heating must be considered. Figure 2-5 shows the evolution of the temperature in the upper (PC-VE_{thin}) and lower (PC-Air) boundaries of the PC. Due to the small thickness of the PC, the temperature inside was considered as a mean of the PC- VE_{thin} and PC-Air temperatures. The maximum temperature measured was 98 ºC in the PC- VE_{thin} boundary. Since the glass transition temperature of the PC is 140 ºC and the working range is up to 120 ºC, it is assumed that the mechanical stability of the PC plate is guaranteed. However, the thickness [The Engineering ToolBox **2003**] and ultrasonic velocity [Asay **1967**] change in this temperature range for PC. On one hand, as the thermal expansion for PC is $70 \cdot 10^{-6}$ $m \cdot m^{-1} \cdot ºC^{-1}$ [The Engineering ToolBox **2003**], the change in thickness for a 1.9 mm plate is ~8 µm. As the maximum variation in thickness is less than 0.5% of the total thickness, thermal expansion effect has been neglected. On the other hand, the longitudinal velocity changes more significantly with a -2.4 $m \cdot s^{-1} \cdot ºC^{-1}$ variation rate [Asay **1967**]. At the maximum PC- VE_{thin} temperature, this implies a PC velocity of 1999 m/s, a reduction of 6% compared to the initial 2125 m/s. Therefore, the temperature in the PC at any given time has to be taken into account to correct the longitudinal wave velocity.

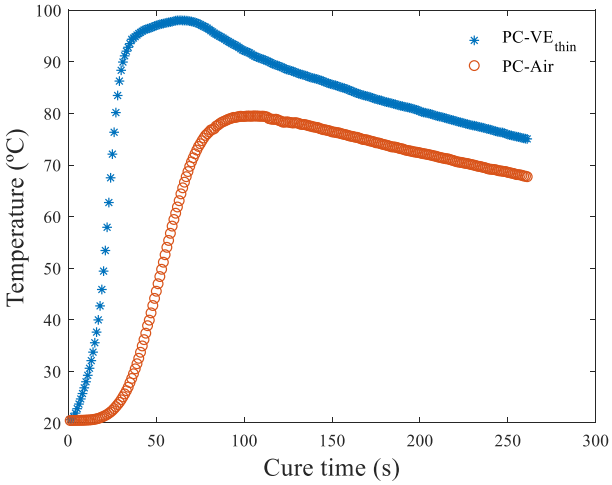

Figure 2-5: Temperatures in the PC plate during curing.

2.3.2.3 Variation of the properties of air

The heat generated during curing of VE resin is transferred to the PC plate as well as to the air. Heat transfer analysis is complex since both the convection on the VE resin and the radiation of the UV lamps must be considered. The experimental measurement of the temperature distribution in the air around the set-up is a highly complex task. A simplified model of the temperature of the air based on two linear zones is applied; the first region goes from the sample surface to the thermocouple placed in the mid-distance and the second from this thermocouple to the transducer. As can be seen in Figure 2-6 the temperatures in both sides of the set-up varied less than 6 ºC, except for short spikes, so it is considered that the temperature in these points during curing are constant.

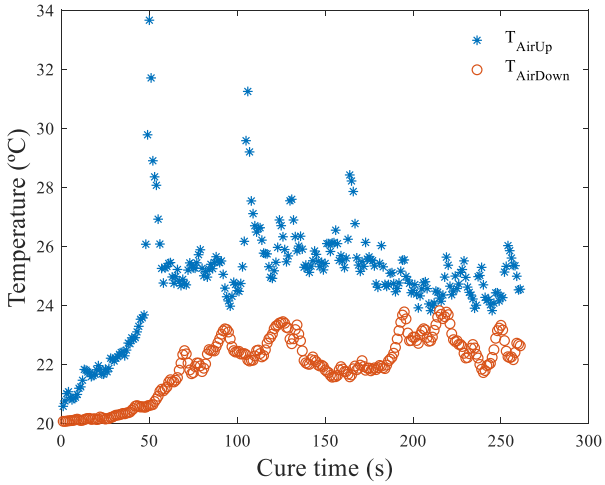

Figure 2-6: Temperatures in the upper (T_{AirUp}) and lower ($T_{AirDown}$) layers of air at 30 mm distance from the VE_{thin} and the PC.

Consequently, the temperature distributions in both sides were estimated as follows:

- In the upper zone, the temperature between the emitting transducer and the thermocouple is considered to be constant (23 ºC) during the whole curing process. However, from the thermocouple to the VE resin surface, it increases linearly from 23 ºC up to the temperature measured at the VE-PC interface (Figure 2-6). Even if this temperature is not real, since in the inner side of the VE the bulk effect induces higher temperatures than in the surface, it is the most conservative value.
- In the bottom zone, the temperature between the transducer and the thermocouple is also considered to be 23 ºC. The temperature between the thermocouple and the PC surface also vary linearly as in the upper zone and goes from 23 ºC up to the PC-Air temperature in each instant (Figure 2-6).

Based on this these estimated temperature distributions, the density and sound velocity in the air have been corrected during curing, considering that the coefficient for both the change in sound velocity is 0.606 $m \cdot s^{-1} \cdot ºC^{-1}$ and -0.00325 $kg \cdot m^{-3} \cdot ºC^{-1}$ for the density.

2.3.2.4 Evolution of the properties during curing

Once the effect of the temperature in the external elements, PC and air, was taken into account the properties of the VE_{thin} during curing were evaluated. The longitudinal and shear velocity and attenuation, as well as the longitudinal and shear viscoelastic modulus of the VE_{thin} are shown in Figure 2-7. In Figure 2-7 (a) and (b) the longitudinal acoustic and mechanical properties are presented. The longitudinal elastic modulus *L'* is 3 GPa at the beginning of the cure, which is an expected value as it is close to the values for epoxy [Aldridge **2014**] and polyester resins [Lionetto **2013**]. The first measurable variation in the viscoelastic properties is detected after 5 seconds of UV light exposure. The first variation observed is a reduction in the resonant frequency of the multilayer plate, which is linked to either a softening of the VE or a thickness increase. The softening, or reduction of the stiffness, was already observed by other authors [Chokanandsombat **2013**; Kister **2015**; Li **2000**] as the resin crosses the zero crosslink density point. This reduction of the stiffness can be observed to stop at 25 seconds, where it starts to regain stiffness. The ratio of change of velocity reaches its maximum point at around 67 seconds, where the temperature in the VE_{thin} can be observed to be maximum, in Figure 2-5. In fact, the attenuations rate shifts from an increase in attenuation to a reduction at that point in time. Despite reaching the maximum temperature at 67 seconds, the curing still goes on at a lower rate. At around 95 seconds, the shear wave interference was finally detectable in the spectrum. The evolution of the shear properties is presented in Figure 2-7 (c) and (d). Observing the shear storage and loss modulus it is visible that the value of the shear loss modulus is smaller than the shear storage modulus. The gelation point is considered to be the point in which the shear storage and the loss modulus have the same value [Martin **2000**],

which would point out that this point was already crossed once shear waves were measured. The evolution of the shear properties are closely similar to the longitudinal properties, with Poisson's ratio showing no change at 0.37.

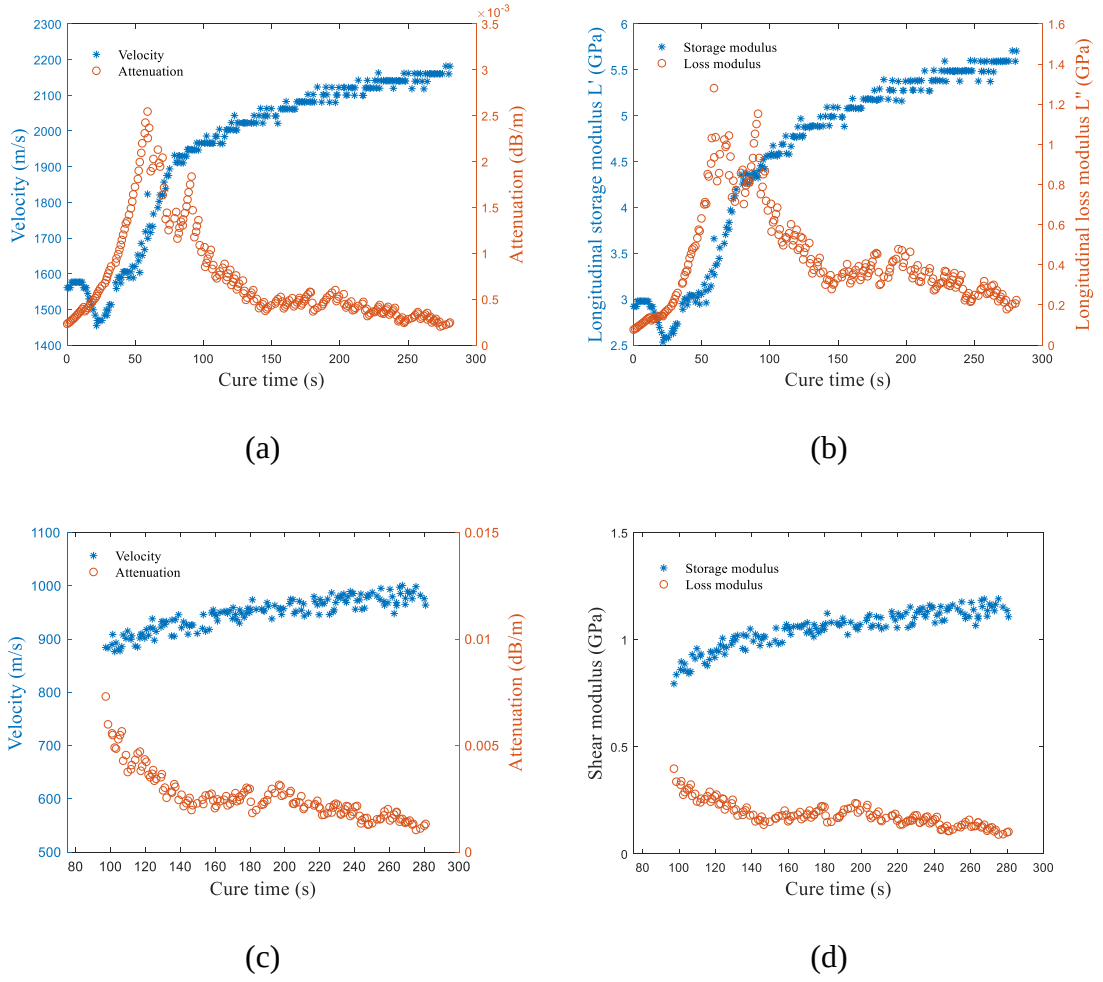

Figure 2-7: Evolution of the acoustic properties during the cure: (a) longitudinal wave properties, (b) longitudinal complex modulus, (c) shear wave properties and (d) shear complex modulus.

To ensure the reliability and precision of the US resonant technique to monitor curing, the data obtained were compared with the measurements of the DoC sensor. Figure 2-8 (a) shows the evolution of the longitudinal elastic modulus and the DoC during curing. It can be observed that both follow the same trend. In both cases, the zero crosslink point can be seen at around 25 seconds. In Figure 2-8 (b), a scatter plot of the estimated Young's modulus with the DoC percentage is presented. The initial DoC is 65% as shear waves where not measurable until that point. The scatter plot also shows the differences in the rate of change of elastic properties in time. At lower DoCs, the number of points is scarcer than at higher DoCs were the rate of change is smaller.

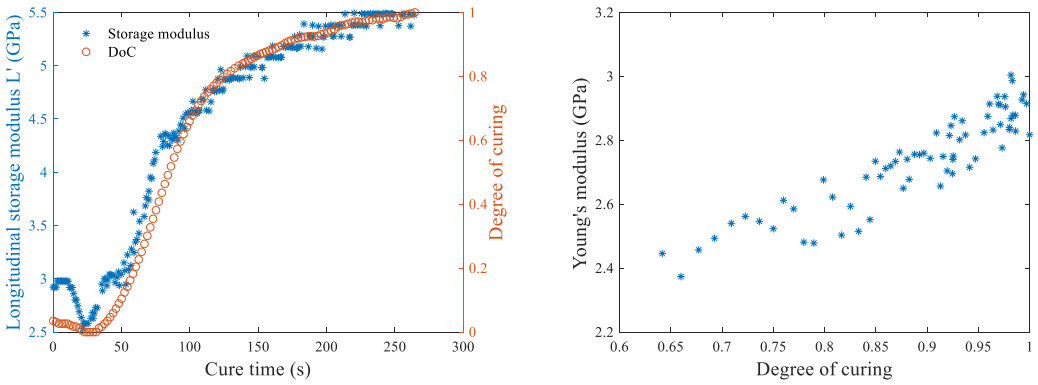

(a) (b)

Figure 2-8: Longitudinal storage modulus and DoC (a), and evolution of the elastic Young's modulus with the DoC (b).

2.3.3 Characterization after curing

The measured acoustic properties after curing at room temperature are compared with the properties at the beginning in Table 2-3. Taking into account the acoustic properties in Table 2-1 and Table 2-3, with the VE_{thick} and VE_{thin}, it can be observed that the difference is less than 3% in the values of the longitudinal wave. This difference may be due to the VE_{thick} not being a real single layer. However, it proved to be a good approximation. It can also be observed that the longitudinal attenuation is larger at the end than in the beginning of the curing, as it can happen in fast curing processes [Lionetto **2013**]. The shear wave velocity and attenuation could not be compared to the beginning of the cure, as they were not detectable up until a high curing point. The estimated final thickness suffered a reduction of ~7% from the initial one, validated with a micrometer. Regarding the viscoelastic properties measured at room temperature (Table 2-3 and Table 2-4) and at the end of curing, when the temperature is roughly 50 ºC higher than room temperature Figure 2-5), these are different. The temperature difference causes a decrease in the longitudinal and shear wave velocities of the VE_{thin} similarly to the case of the PC material.

Table 2-3: Extracted acoustic properties of the VE_{thin}.

Material	Thickness ACUS (mm)	Thickness micrometer (mm)	Longitudinal velocity (m/s)	Shear velocity (m/s)	Longitudinal attenuation (dB/m)	Shear attenuation (dB/m)
Liquid VE_{thin}	1.89	-	1551	-	249 10^{-6}	-
Cured VE_{thin}	1.76	1.8 ± 0.05	2351	1065	757 10^{-6}	3.5 10^{-3}

The mechanical properties after the curing are shown in Table 2-4. Comparing the VE_{thin} at the beginning of the cure, an increase in stiffening is observed. Young's modulus in Table 2-4 is 10% higher than that at the end of the curing in Figure 2-8 (b). This difference is caused by the cooling of the VE_{thin}. It should be noted that Poisson's ratio is consistent at 0.37.

Table 2-4: Extracted elastic mechanic properties of the VE_{thin}.

Material	Young's modulus (GPa)	Shear modulus (GPa)	Bulk modulus (GPa)	Poisson's ratio	Density (kg/m^3)
Liquid VE_{thin}	-	-	2.7 + 0.07i	0.5	1126
Cured VE_{thin}	3.3 + 0.8i	1.2 + 0.3i	4.47 + 0.35i	0.371 – 0.01i	1052

2.4 Conclusions

In this chapter, ACUS spectroscopy has been used to monitor the UV curing of a VE resin. This technology has proved to be useful to monitor a fast curing process were contact between the part and the transducer cannot be made, such as UV curing.

During curing, due to the exothermic nature of the process, the temperature of the resin increases sharply. This increase in temperature in the resin alters the properties of the PC plate and the air surrounding it. These changes in the properties need to be taken into account when characterizing the resin's properties. Thus, extra sensors like thermocouples are required to reduce the error in the measurements.

Moreover, curing causes chemical shrinkage in the resin sample, which needs to be considered. Measuring the thickness by ACUS with a resolution under 150 μm required a more complex set-up, due to the changes in air properties. Thus, the thickness was indirectly estimated based on the DoC measured with the direct-current sensor.

The mandatory use of a PC thin-plate to support the liquid resin must be considered during data analysis, by applying a bilayer material model.

At the earlier stages of curing, only the longitudinal waves where measurable due to the great attenuation of shear waves in the liquid VE resin. However, above the gel point, shear waves can be registered. Consequently, with the simultaneous measurement of longitudinal and shear properties, Young's modulus was characterized.

When the measurements of the ACUS spectroscopy were combined with the direct current sensor, a correlation between the DoC and the estimated Young's modulus can be observed. It must be pointed out that the Young's modulus values obtained by ACUS fitted with values reported in the VE's technical datasheet.

Chapter 3
Leaky Lamb waves with ACUS

The second goal of this thesis is to evaluate the properties of composite materials without contact based on guided waves. Using leaky Lamb waves, without contact, presents different challenges to ensure correct and efficient measurement in samples with different geometries. Thus, in this chapter the efficiency to generate guided waves with focused and unfocused transducers for straight and curved GFRPs parts is evaluated. The first section focuses on the theoretical background of guided waves in composite materials. The second section presents the set-up and methodology followed. The third section presents the results, whilst the last one shows the conclusions.

3.1 Theoretical background

A plane wave propagating in a semi-infinite fluid (Figure 3-1) is defined by the polarization vector $\boldsymbol{P}_f = [\cos(\theta), \sin(\theta)\cos(\phi), \sin(\theta)\sin(\phi)]$ and wave vector $\boldsymbol{k}_f = k_f \boldsymbol{P}_f$. When the plane wave propagating in the fluid comes across a semi-infinite solid layer, several waves can be generated inside, among other depending on the mechanical properties of the solid. Particularly, when the solid is a FRP composite, some mechanical properties, like the stiffness, are directionally dependent and present an orthotropic anisotropy. The stiffness of the FRP composite can be defined using the Voight matrix notation $[C_{ij}]$ (Eq. (3-1)) [Hosten **1987**] where i and j are the three axes (1,2,3). The three principal axes in a FRP are: the fiber direction, which is axis 1 for unidirectional composites and axes 1 and 2 for bidirectional FRP; and non-fiber direction, which are axes 2 and 3 for unidirectional composites and only axis 3 for bidirectional FRP. For FRP with other lay-ups ([0,+45,-45,0] for example), one might choose the reference for the axes as preferred.

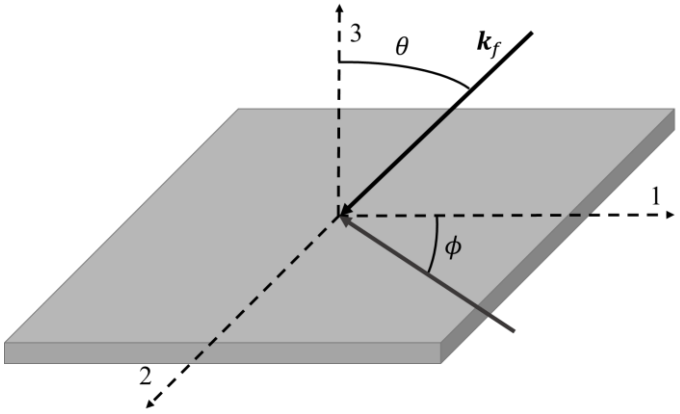

Figure 3-1: Incident wave in plate.

$$[C_{ij}] = \begin{bmatrix} C_{11} & C_{12} & C_{13} & 0 & 0 & 0 \\ - & C_{22} & C_{23} & 0 & 0 & 0 \\ - & - & C_{33} & 0 & 0 & 0 \\ - & - & - & C_{44} & 0 & 0 \\ - & symmetric & - & - & C_{55} & 0 \\ - & - & - & - & - & C_{66} \end{bmatrix} \quad (3\text{-}1)$$

When an incident plane wave interacts with an orthotropic material, a reflected wave with $\boldsymbol{P}_r = [-\cos(\theta), \sin(\theta)\cos(\phi), \sin(\theta)\sin(\phi)]$ and $\boldsymbol{k}_r = k_f \boldsymbol{P}_r$ is generated, along with at most three refracted waves with $\boldsymbol{P}_J$, $\boldsymbol{k}_J$ where J=l,s_1,s_2 (Figure 3-2) [Hosten **1991**]. The three refracted waves are one quasilongitudinal (l) and two quasishear (s_1, s_2) waves. The two quasishear waves propagate with a polarization with respect to the first and second axes. When the incident wave is in the direction of an axis ($\sin(\phi) = 0$ or $\sin(\phi) = 1$), only two waves are generated, a quasilongitudinal (l) and a quasishear (s) wave. There is only one shear wave because the velocity of both shear waves coincides in the axes [Rokhlin **1986**]. For each refracted wave, the critical angle is defined by $\theta_{J\text{lim}} = \arcsin(k_J/k_f)$ [Hosten **1991**].

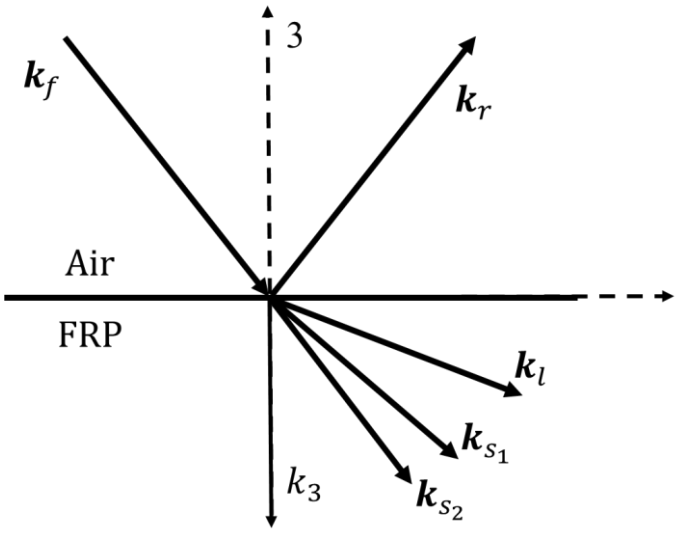

Figure 3-2: Refracted waves in semi-infinite FRP medium.

When the FRP composite is not a semi-infinite medium and, instead, has a plate-like geometry, Lamb waves are generated in the FRP. If Lamb waves are propagating in a plate surrounded by a semi-infinite fluid, some of the energy of the Lamb wave is leaked into the fluid. In order to measure Lamb waves without contact, the leaked acoustic energy is measured. This method is known as leaky Lamb waves (LLW) [Giurgiutiu **2015**; Karim **1990**].

To model the dispersion curves of the LLW in plate-like FRP composites, several analytical methods have been proposed, amongst which the transfer matrix method (TMM) [Castaings **2003**] and the stable matrix method (SMM) [Wang **2001**] are the most used.

3.1.1 Transfer matrix method

The process to calculate the dispersion curves of the LLW with the TMM is carried out in two steps. First, the wavenumber of the refracted longitudinal and shear wave (or waves), together with their associated polarization vectors are obtained. Then the transfer matrix that relates the displacements at both surfaces of the plate, the top and bottom of the plate, can be calculated considering stress and displacement continuity in the plate. When the plate is composed of multiple layers with different properties, these two steps are carried out for each layer iteratively and the transfer matrix of the plate is calculated by multiplying the transfer matrices of all layer.

In an anisotropic solid, the Christoffel's equation holds [Auld **1973**]:

$$\Gamma_{ij}P_j - \rho_s\omega^2 P_i = 0 \tag{3-2}$$

where Γ_{ij} is element of the Christoffel's tensor, where i and j are the three axes 1,2,3. Γ_{ij} relates the mechanical properties of the plate (stiffness $[C_{ij}]$ and density ρ_s) and those of the refracted waves (angular frequency ω and wavenumber $\boldsymbol{k}_J$) [Auld **1973**]. Non-trivial solutions of Γ_{ij} are obtained by an eigenvalues analysis of Eq. (3-2), where the eigenvectors represent the polarization vectors of the refracted waves [Auld **1973**; Hosten **1991**].

In order to obtain the eigenvectors, firstly, the wavenumbers of the refracted shear and longitudinal waves, $\boldsymbol{k}_J$ is decomposed in the 1, 2 and 3 axes directions, with the unitary vectors $\boldsymbol{x}_1$, $\boldsymbol{x}_2$ and $\boldsymbol{x}_3$ respectively:

$$\boldsymbol{k}_J = k_{J1}\boldsymbol{x}_1 + k_{J2}\boldsymbol{x}_2 + k_{J3}\boldsymbol{x}_3 \tag{3-3}$$

According to Snell's law, the wavenumber of the J refracted wave in the 1 and 2 axes (k_{J1} and k_{J2}) is the same as the wavenumber in the fluid in the same direction (k_{f1} and k_{f2} respectively) [Hosten **1991**]. This implies that for all J mode, in the 1 or 2 directions, the wavenumber will be the same (k_1 or k_2):

$$k_{f1} = k_{J1} = k_1 \text{ and } k_{f2} = k_{J2} = k_2 \tag{3-4}$$

From Eq. (3-3) and Eq. (3-4), it can be observed that only k_{J3} is unknown. Resolving the eigenvalue and eigenvector problem from Eq. (3-2), k_3 can be obtained [Hosten **1991**]. k_3 contains all k_{J3} solutions:

$$a(k_3^2)^3 + b(k_3^2)^2 + c(k_3^2) + d = 0 \tag{3-5}$$

where a, b, c and d are coefficients dependent on the mechanical properties of the plate (stiffness $[C_{ij}]$ and density ρ_s) and the refracted waves (angular frequency ω and wavenumber k_1, k_2) .

In the non-principal axes, k_3^2 in Eq. (3-5) has three real solutions, one for each J refracted wave. In the principal axes, there are also three real solutions, but only two of them are physically true, since there are only two refracted waves [Rokhlin **1986**]. In our case, due to the geometries obtained in the 3D UV pultrusion process, the analysis is narrowed down to the principal axis 1 and thickness axis 3. For this case, k_3^2 has a real solution for each J refracted wave ($J = l, s$). The two solutions of k_3^2 can be positive or negative real numbers. If k_3^2 is a positive number, k_3 will have two real solutions, a positive and a negative . However,a negative k_3 makes no physical sense and is thefore ignored. k_3^2 is positive under the condition that the incidence angle θ of the $\boldsymbol{k}_f$ wave is under the critical angle $\theta_{J_{lim}}$. This condition is called the subcritical regime. If k_3^2 is a negative number, k_3 will have to solutions that are purelly imaginary. As in the previous case, a negative imaginary k_3 makes no physical sense. This condition is called the hypercritical regime, when the incidence angle θ of the $\boldsymbol{k}_f$ wave is larger than the critical angle $\theta_{J_{lim}}$.

Assuming that the FRP material is elastic, attenuation is not considered, and therefore the $\boldsymbol{k}_J$ should be a real number. However, according to the generalized Snell's law, for angles larger than $\theta_{J_{lim}}$, the $\boldsymbol{k}_J$ waves attenuate with a damping vector $\boldsymbol{k}_J''$ for the direction of axis 3 [Hosten **1991**]. At angles larger than $\theta_{J_{lim}}$ the refracted waves become evanescent [Deschamps **1996**] So, for the hypercritical regime, Eq. (3-3) becomes

$$\boldsymbol{k}_J^* = \boldsymbol{k}_J - i\boldsymbol{k}_J'' = k_{J1}\boldsymbol{x}_1 - ik_{J3}''\boldsymbol{x}_3 \tag{3-6}$$

The polarization vectors $\boldsymbol{P}_J$ are obtained as eigenvectors solving the eigenvalue problem from Eq. (3-2) [Hosten **1991**]. For the subcritical regime we have

$$P_3 = -\Gamma_{J31}P_{J1}/\Gamma_{J33} \tag{3-7}$$

and for the hypercritical regime

$$P_{J3} = i\Gamma_{J31}P_{J1}/\Gamma_{J33} \tag{3-8}$$

where P_{J3} is the component of polarization vector of the J wave in the 3 direction and Γ_{Jij} is the ij element of the tensor matrix for the J refracted wave. The P_{J1} component of the polarization vector is normalized [Hosten **1991**]. In the subcritical regime, both $\boldsymbol{k}_J$ and $\boldsymbol{P}_J$ are vectors of real numbers, but in the hypercritical regime both $\boldsymbol{k}_J^*$ and $\boldsymbol{P}_J^*$ are vectors of complex numbers.

To model the transfer matrix the displacement and stress vectores in the lower boundary (+ superscript) of the plate are defined. The displacement vector in the 1 and 3 axes is $\boldsymbol{u}_n^+ = [u_n^+, w_n^+]^T$ and the strees vector is $\boldsymbol{\sigma}_n^+ = [\sigma_n^+, \tau_n^+]^T$. The amplitude vectors of the refracted wave in the upper ($-$ superscript) and lower boundaries are

defined as $\boldsymbol{a}_n^- = [a_n^-, c_n^-]^T$ and $\boldsymbol{a}_n^+ = [a_n^+, c_n^+]^T$ respectively. To obtain the transfer matrix of a layer with thickness d, the matrix that links the displacements and stresses at upper and lower interfaces of the layer is considered [Hosten **1993**b]:

$$\begin{bmatrix} \boldsymbol{u}_n^+ \\ \boldsymbol{\sigma}_n^+ \end{bmatrix} = [T]_n \begin{bmatrix} \boldsymbol{a}_n^+ \\ \boldsymbol{a}_n^- \end{bmatrix} = \begin{bmatrix} P_{l1}R & P_{s1}Q & P_{l1}R^{-1} & P_{s1}Q^{-1} \\ P_{l3}R & P_{s3}Q & -P_{l3}R^{-1} & -P_{s3}Q^{-1} \\ ia_1R & ia_2Q & ia_1R^{-1} & ia_2Q^{-1} \\ ia_4R & ia_5Q & -ia_4R^{-1} & -ia_5Q^{-1} \end{bmatrix} \begin{bmatrix} \boldsymbol{a}_n^+ \\ \boldsymbol{a}_n^- \end{bmatrix} \tag{3-9}$$

where $R = e^{-ik_l d}$; $Q = e^{-ik_s d}$, $d = d_n - d_{n-1}$ and a_1, a_2, a_4 and a_5 are coefficients dependent on the properties of the layer (stiffness $[C_{ij}]$ and thickness d) and those of the refracted waves (polarization vector $\boldsymbol{P}_J$ and wavenumber $\boldsymbol{k}_J$).

Eq. (3-9) can also be expressed as $[S]_n^+ = [T]_n[V]_n$, where $[S]_n^+$ is the displacement and stress vector in the lower boundary of a n-layer and $[V]_n$ is the amplitude vector. Assuming $[V]_n$ to be constant for the n-layer [Hosten **1993**b], and consequently $[S]_n^- = [E]_n[V]_n$, where $[S]_n^-$ is the displacement and stress vector in the lower boundary of the n-layer. The matrix $[E]_n$ is equal to $[T]_n$, but the R and Q terms are 1 [Hosten **1993**b]. Thus, the transfer matrix $[A]_n$ for the n-layer can be obtained as follows:

$$[S]_n^+ = [T]_n[E]_n^{-1}[S]_n^- \tag{3-10}$$

$$[A]_n = [T]_n[E]_n^{-1} \tag{3-11}$$

$$[S]_n^+ = [A]_n[S]_n^- \tag{3-12}$$

To calculate the transfer matrix for an N-layer material ($[A]_N$) the continuity of displacements and stresses in the different layers (n and n-1) is considered:

$$[S]_n^+ = [S]_{n-1}^- \tag{3-13}$$

then $[A]_N$ can be expressed as [Hosten **1993**b]:

$$[A]_N = \prod_{n=0}^{N-1} [A]_n \tag{3-14}$$

With this multilayer transfer matrix, the dispersion curves of the LLW for a composite material can be obtained, by establishing the boundary conditions for a plate. The displacements at the upper and lower boundaries of the N-layer plate are the same ($\boldsymbol{u}_0^- = \boldsymbol{u}_{N-1}^+ = \boldsymbol{u}$) and the stresses are zero ($\boldsymbol{\sigma}_0^- = \boldsymbol{\sigma}_{N-1}^+ = \boldsymbol{0}$). Thus Eq. (3-12) can be rewritten as follows [Castaings **2003**]:

$$\begin{bmatrix} \boldsymbol{u} \\ \boldsymbol{0} \end{bmatrix} = [A]_N \begin{bmatrix} \boldsymbol{u} \\ \boldsymbol{0} \end{bmatrix} \tag{3-15}$$

To ensure that Eq. (3-15) has non-trivial solutions, and therefore LLW propagate, $\det([A]_N) = 0$ must be fulfilled. The $\boldsymbol{k}_f$ waves that fulfil the condition will propagate LLW in the composite plate.

3.1.2 Stiffness matrix method

TMM is fast and efficient, but it becomes numerically unstable at large frequency-thickness values [Castaings **1994**]. This instability is known as "small differences of large numbers" [Giurgiutiu **2015**]. The SMM was developed to overcome TMM associated instability problems [Wang **2001**].

As TMM, SMM has two steps. First, the wavenumber $\boldsymbol{k}_J$ [Wang **2001**] and the polarization vectors $\boldsymbol{P}_J$ are obtained. Then, the transfer matrix is obtained. For multilayer plates, another step is required to relate the transfer matrix of each layer. As in Section 3.1.1, only propagation in the principal axis 1 will be evaluated.

Considering the wave propagating in the principal axis 1, two solutions for k_3 are obtained [Wang **2001**]:

$$k_{J3} = \sqrt{(-B \pm (B^2 - 4AC)^{1/2})/2A} \tag{3-16}$$

where the – sign is for the J refracted longitudinal wave and + is for the J refracted shear wave. A, B and C are coefficients dependent on the mechanical properties of the plate (stiffness $\boldsymbol{C}_{ij}$ and density ρ_s) and the refracted waves (angular frequency ω and wavenumber k_{J1}).

The solution to Eq. (3-16) only has two solutions, while Eq. (3-5) has three solutions. To calculate the polarization vector $\boldsymbol{P}_J$ Wang and Rokhlin proposed the following expression [Wang **2001**]:

$$P_{J3} = \frac{\rho_s \omega^2 - C_{11} k_1^2 - C_{55} k_{J3}^2}{(C_{13} + C_{55}) k_1 k_{J3}} \tag{3-17}$$

Yet, the main benefit of the SMM, regarding the TMM is how the transfer matrix is obtained.

The displacement, stress and displacement vectors in the upper and lower boundaries are defined as in Section 3.1.1. In the SMM, the displacement and stress terms in equations Eq. (3-9) to Eq. (3-15) are rearranged, with the final objetive of eliminating the thickness term that is present in diagonal of $[A]_n$ [Wang **2001**]. The displacements in the upper and lower boundaries of the n-layer is related with the amplitude as

$$\begin{bmatrix}\boldsymbol{u}_n^- \\ \boldsymbol{u}_n^+\end{bmatrix} = [T]_n^u \begin{bmatrix}\boldsymbol{a}_n^- \\ \boldsymbol{a}_n^+\end{bmatrix} = \begin{bmatrix} P_{l1} & P_{s1} & P_{l1}R^{-1} & P_{s1}Q^{-1} \\ P_{l3} & P_{s3} & -P_{l3}R^{-1} & -P_{s3}Q^{-1} \\ P_{l1}R & P_{s1}Q & P_{l1} & P_{l1} \\ P_{l3}R & P_{s3}Q & -P_{l3} & -P_{s3} \end{bmatrix} \begin{bmatrix}\boldsymbol{a}_n^- \\ \boldsymbol{a}_n^+\end{bmatrix} \tag{3-18}$$

and the stresses in the upper and lower boundaries as

$$\begin{bmatrix}\boldsymbol{\sigma}_n^- \\ \boldsymbol{\sigma}_n^+\end{bmatrix} = [T]_n^\sigma \begin{bmatrix}\boldsymbol{a}_n^- \\ \boldsymbol{a}_n^+\end{bmatrix} = \begin{bmatrix} ia_1 & ia_2 & ia_1R^{-1} & ia_2Q^{-1} \\ ia_4 & ia_5 & -ia_4R^{-1} & -ia_5Q^{-1} \\ ia_1R & ia_2Q & ia_1 & ia_2 \\ ia_4R & ia_5Q & -ia_4 & -ia_5 \end{bmatrix} \begin{bmatrix}\boldsymbol{a}_n^- \\ \boldsymbol{a}_n^+\end{bmatrix} \tag{3-19}$$

Considering that the amplitudes $\begin{bmatrix}\boldsymbol{a}_n^- \\ \boldsymbol{a}_n^+\end{bmatrix}$ have to be the same, from Eq. (3-18) and Eq. (3-19) the relationship between the displacements and stresses can be obtained:

$$\begin{bmatrix}\boldsymbol{\sigma}_n^- \\ \boldsymbol{\sigma}_n^+\end{bmatrix} = [T]_n^\sigma [T]_n^{u^{-1}} \begin{bmatrix}\boldsymbol{u}_n^- \\ \boldsymbol{u}_n^+\end{bmatrix} \tag{3-20}$$

$$[K]_n = [T]_n^\sigma [T]_n^{u^{-1}} \tag{3-21}$$

As it can be observed from Eq. (3-18) and Eq. (3-19), the stiffness matrix $[K]_n$ ($[A]_n$ for TMM), does not have the thickness term in its diagonal, which will keep the stiffness matrix as a regular matrix [Wang **2001**].

For the multilayer plate, the case for two adjoining plates is considered, $[K]_n$ and $[K]_{n-1}$:

$$\begin{bmatrix}\boldsymbol{\sigma}_n^- \\ \boldsymbol{\sigma}_n^+\end{bmatrix} = [K]_n \begin{bmatrix}\boldsymbol{u}_n^- \\ \boldsymbol{u}_n^+\end{bmatrix} \text{ and } \begin{bmatrix}\boldsymbol{\sigma}_{n-1}^- \\ \boldsymbol{\sigma}_{n-1}^+\end{bmatrix} = [K]_{n-1} \begin{bmatrix}\boldsymbol{u}_{n-1}^- \\ \boldsymbol{u}_{n-1}^+\end{bmatrix} \tag{3-22}$$

where $\boldsymbol{\sigma}_n^+ = \boldsymbol{\sigma}_{n-1}^-$, $\boldsymbol{u}_n^+ = \boldsymbol{u}_{n-1}^-$, $[K]_{11}$ to $[K]_{22}$ are 2x2 submatrices

$$[K]_n = \begin{bmatrix}[K]_{11}^n & [K]_{12}^n \\ [K]_{21}^n & [K]_{22}^n\end{bmatrix} \text{ and } [K]_{n-1} = \begin{bmatrix}[K]_{11}^{n-1} & [K]_{12}^{n-1} \\ [K]_{21}^{n-1} & [K]_{22}^{n-1}\end{bmatrix} \tag{3-23}$$

Excluding $\boldsymbol{\sigma}_n^+$ and $\boldsymbol{u}_n^+$ in the first equation of Eq. (3-22) and substituting in the second of Eq. (3-22), $\boldsymbol{\sigma}_n^-$ and $\boldsymbol{u}_n^-$ are related with $\boldsymbol{\sigma}_{n-1}^+$ and $\boldsymbol{u}_{n-1}^+$:

$$\begin{bmatrix}\boldsymbol{\sigma}_n^- \\ \boldsymbol{\sigma}_{n-1}^+\end{bmatrix} = \begin{bmatrix} [K]_{11}^n + [K]_{21}^n([K]_{11}^{n-1} - [K]_{22}^n)^{-1}[K]_{12}^n & -[K]_{21}^n([K]_{11}^{n-1} - [K]_{22}^n)^{-1}[K]_{21}^{n-1} \\ [K]_{12}^{n-1}([K]_{11}^{n-1} - [K]_{22}^n)^{-1}[K]_{12}^n & [K]_{22}^{n-1} - [K]_{12}^{n-1}([K]_{11}^{n-1} - [K]_{22}^n)^{-1}[K]_{21}^{n-1} \end{bmatrix} \begin{bmatrix}\boldsymbol{u}_n^- \\ \boldsymbol{u}_{n-1}^+\end{bmatrix} \tag{3-24}$$

By calculating Eq. (3-24) iteratively for each of the N-layers, the stiffness matrix $[K]_N$ can be obtained, which will still be regular [Wang **2001**].

Following a similar procedure as in the TMM, based on the multilayer matrix $[K]_N$ the dispersion curves for the LLW are obtained. The same boundary conditions as previously are considered with the displacement being equal at the boundaries and stresses zero:

$$\begin{bmatrix} \mathbf{0} \\ \mathbf{0} \end{bmatrix} = [K]_n \begin{bmatrix} \boldsymbol{u} \\ \boldsymbol{u} \end{bmatrix} \tag{3-25}$$

As in the case for TMM for the cases that $\det([K]_N) = 0$, the condition to propagate LLW will be fulfilled.

3.1.3 Mixed TMM & SMM

The SMM method presents a numerical problem at low wavenumbers and high frequency values [Kamal **2014**]. When the wavenumber k_{j3} for the principal axis is calculated in Eq. (3-16), the elements B and C are dependent on the angular frequency (ω). At high frequencies and low wavenumbers, the wavenumber k_{j3} becomes purely imaginary, although the radical should never become negative for angles under the critical angle.

In this thesis, a mixed TMM&SMM method is proposed to the limitations of both TMM and SMM. For the calculation of $\boldsymbol{k}_J$ and $\boldsymbol{P}_j$, eigenvectors and eigenvalues are calculated like in the TMM. However, for the transfer matrix calculation, the SMM is employed, to avoid instabilities at high frequency thickness values.

3.2 Set-up and methodology

3.2.1 Straight and curved composite plate

To evaluate the elastic properties, a composite profile with a straight and a curved section manufactured by 3D-UV pultrusion process [Tena **2015**] was used. The profile was a GFRP composite with unidirectional E-Glass rovin fiber with a VE matrix. Its thickness was 3 mm, its density 1940 kg/m^3 and it had an omega shape in the thickness direction (Figure 3-3). The omega part had a straight plate-like section of 160 mm x 25 mm. This section was measured over the range of 60 mm, with 0.6 mm steps, as it can be observed in Figure 3-4: Set-up for the measurement of the straight section.. The omega part also had a curved plate like section of 90º and with 190 mm radius in its furthermost face. This section was also measured over the curve range of 60 mm, which is a radial distance of 18.1º of angle, as can be observed in Figure 3-5.

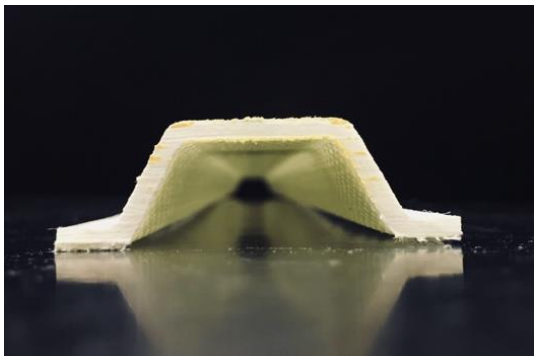

Figure 3-3: Omega geometry.

To measure the propagation of Lamb waves at different distances, two different set-ups were built for the straight and curved sections. It was necessary to use two different manipulators to displace the transducers, due to the different geometries of both sections. A lineal manipulator was used for the straight section and a rotational manipulator for the curved section. The electronic equipment used to generate and receive the US wave was also different in both set-ups. The common equipment for both set-ups included: two pairs of wideband piezocomposite transducers from 200 kHz to 400 kHz and 400 kHz to 800 kHz made at the CSIC; a goniometer to control the incidence angle of the US wave; and a 10 V/pC Femto HQA-15M-10T charge amplifier.

For the straight section, apart from the aforementioned equipment, an Airtech 1000 from Ingenieur-Büro Dr. Hillger was used as a manipulator. The USPC 4000 AirTech, from the same company, was used to excite the transducers and to capture the data. The excitation signal was a train of square pulses with 1 to 20 pulses length and a voltage from 50 V to 200 V. Several pulse lengths and voltages were used for different measurements. For the transducer with the lowest frequency, 200 kHz to 400 kHz, a single pulse with the highest voltage, 200 V, could excite all of the frequency range of the transducer. At higher frequencies with the other transducers, 400 kHz to 800 kHz, a single pulse could only excite the lowest frequencies, up to 550 kHz. The higher frequency transducers where more efficient at their lowest working frequency, which required longer train pulses, of up to 20 pulses, to ensure that the highest frequencies, 550 kHz to 750 kHz, were propagated and measured. The excitation voltage was reduced from 200 V to 50 V since high voltages were not necessary.

For the curved section, an A3200 manipulator from Aerotech was used to displace the transducer rotationally. A HP 33120A signal generator and a Falco-WMA-300 power amplifier were used to excite the transducers. A Tektronix MDO4104-B oscilloscope was used to capture the signals. The excitation signal used was the same as for the straight section, however, the minimum voltage used was 100 V instead of 50 V. A higher than 50 V signal was necessary due to a worse coupling of the wave in the curved section.

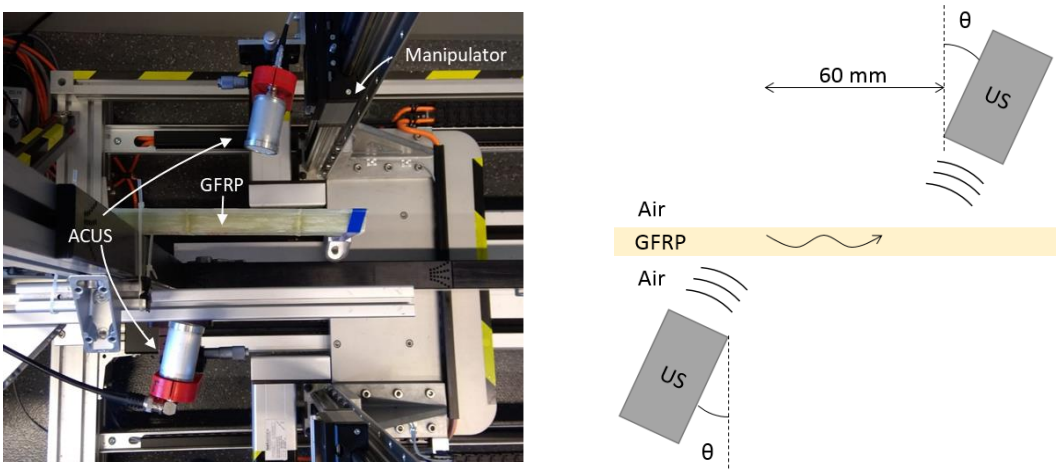

Figure 3-4: Set-up for the measurement of the straight section.

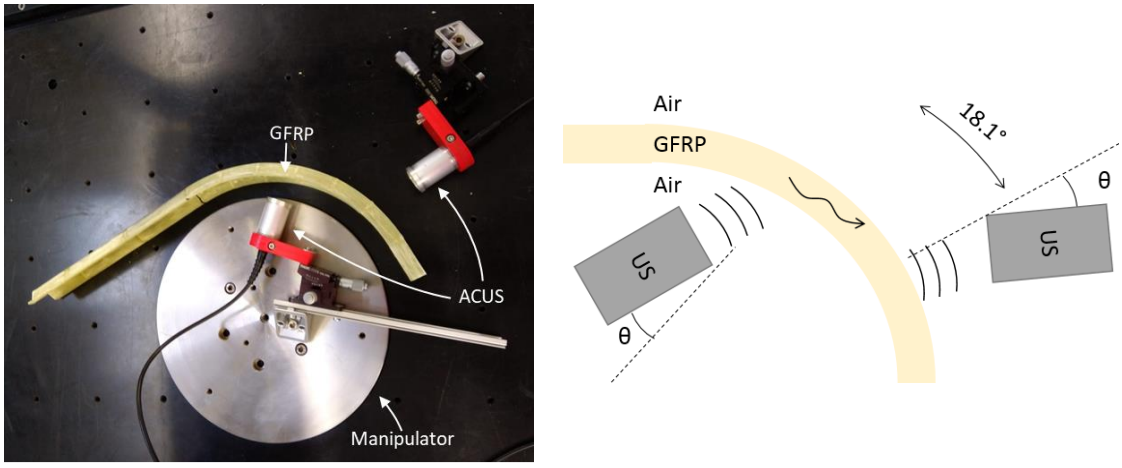

Figure 3-5: Set-up for the measurement of the curved section.

To obtain the dispersion curves of the straight and curved section a 2-dimensional fast Fourier transform (2D-FFT) was carried out [Alleyne **1990**]. The results of the 2D-FFT where later compared with the theoretical dispersion curves obtained with the mixed TMM&SMM model, explained in Section 3.1.3. The elastic properties of the GFRP were initially approximated [Castaings **2004**]. For curvatures with wide radius over 100 mm radius, which is the case for the GFRP plate, the same TMM model can be used for the straight and curved sections [Fong **2005**].

3.2.2 Transducer efficiency: geometry and multimode generation

The generation of guided waves in solids with ACUS has proved to be a task that requires high precision in the choice of incidence angle [Castaings **1996**]. Selecting this angle is not always a simple task when either the approximate material properties are unknown or the shape of the surface is curved.

In straight plates, an unfocused transducer generates a single incidence angle in the surface of the plate. To generate multiple incidence angles with an unfocused transducer it is necessary to change the angle of the transducer. Therefore, to generate

multiple modes with different velocities it is necessary to make several measurements at different angles. A focused transducer, unlike the unfocused one, generates multiple incidence angles in the surface of the plate [Giacchetta **2015**]. Since multiples incidence angles are generated simultaneously, there is no need to move the transducer to generate this effect. With focused transducers, several modes can theoretically be generated in the straight plate.

In curved plates, the shape of the surface causes the incident wave to behave differently than for straight plates. With unfocused transducers, unlike for the straight plate, multiple incidence angles are generated in the surface of the curved plate. The curvature causes the incident plane wave to scatter into different incident angles in each of the infinitesimal sections of the curve. This way, several incidence angles can be generated from a single incident plane wave. With focused transducers, the behavior of the wave with the surface is the same, the only difference being that the incident wave could already generate multiple incidence angles.

On the one hand, generating multiple incidence angles simultaneously could be beneficial, since several modes could be simultaneously excited. On the other hand, the scattered incidence angles also disperse the energy of the US wave into each of the incident angles. With a technique like ACUS, dispersing the energy in the form of useful and non-useful incidence angles may cause an inability to measure any signal at all. This means that evaluating the efficiency in generating several modes is necessary.

First, it is necessary to evaluate the efficiency of each of the transducers independently in order to be able to make a comparison between them, since different transducers have different efficiency transducing waves into the air. In order to measure the efficiency of the transducers, a set-up was built to measure their sensitivity in a simple pulse echo. The sensitivity was calculated dividing the input voltage with the output voltage, to obtain the relationship between input and output. This was later simply transformed into dB. The transducers where placed at a distance of 50 mm from a thick wood block, used just as the reflective boundary for the waves propagating through the air, with a normal incidence angle. The distance of 50 mm is the focal distance of the focused transducers. The transducers used where the NCG200-D19, NCG200-D19-P50 and NCG500-D19-P50 from ULTRAN and a previously described pair from the CSIC. Second, to measure the efficiency in generating and measuring guided waves, the same set-up as in Section 3.2.1 was used for the straight and curved sections.

In addition to the fully ACUS measurements, hybrid ACUS-LUS measurements were carried out, showed in Figure 3-6. LUS is advantageous when the objective is trying to measure several modes, since its efficiency does not depend on the incidence angle like ACUS. The LUS measurements were carried out with a Polytec PSV-500-3D, a 3-dimensional laser Doppler vibrometer (3D-LDV). The 3D-LDV measures the velocity of the vibration of the surface of the material in the three axes. Some modes are more present a higher displacement in different directions (propagation, thickness…), as

it is later observed in Section 3.3.2, where the use of a 3D-LDV, as opposed to a 1D-LDV, is advantageous. Another advantage of the LDV is the possibility to obtain an image of the area of the plate, either the straight or the curved section. The propagation of different waves can be observed along each section. The 3D-LDV, however, is a costly equipment that requires high precision in the location of the plate. The measurement points in the plate are calibrated once, a process that is done manually, and the position of the plate must be kept fixed. In processes where this changes, this is a limitation.

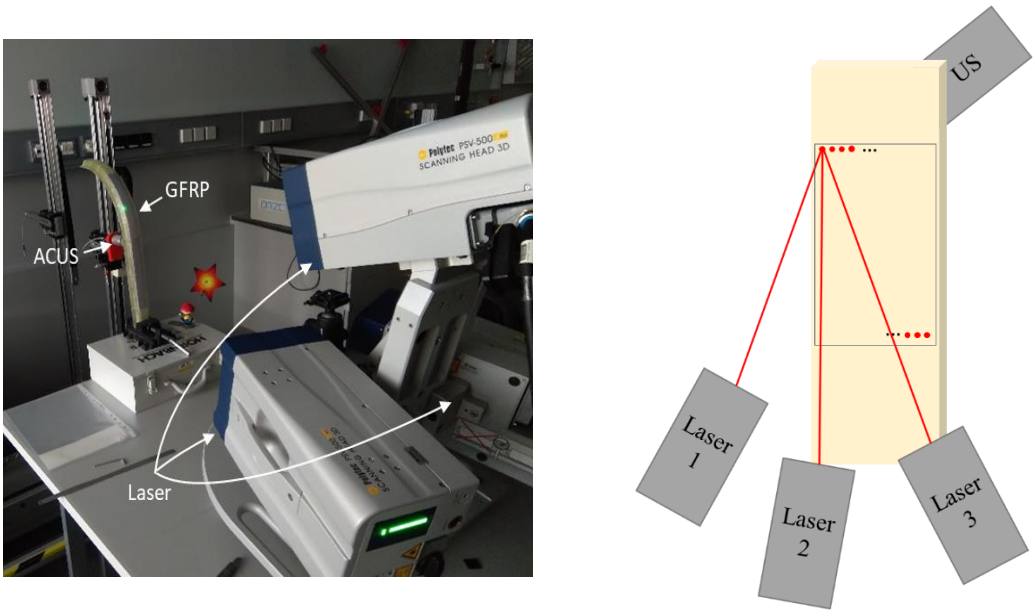

Figure 3-6: Set-up for the measurement of the straight and curved section with the 3D-LDV.

3.3 Results

3.3.1 Straight and curved composite plate

The results for the propagated LLW for the straight and curved sections can be observed in the Figure 3-7 (a) and Figure 3-7 (b) respectively. Measurements made with different train pulses at different frequencies were put together in the observable range of 200 kHz to 750 kHz.

In Figure 3-7, the modes with different phase velocities were measured changing the angle of the goniometer and the train pulse length. The A0 mode in both Figure 3-7 (a) and Figure 3-7 (b), which is the lowest order mode, has almost constant velocity, less than 5% change, along the measurement range. This means that the A0 mode was measured at a fixed incidence angle, close to 9º, in the whole range. The S0 mode, the second lowest order mode, reduces its velocity more than 40%. This has a direct effect in the incidence angle, which changes from close to 4º at the highest velocity to close to 7.5º at the lowest measured. The A1 mode was also measured and can be observed in Figure 3-7. Despite different modes usually having different velocities and incidence

angles, that is not always the case. For example, when the velocity is the same or the incidence angles are close to each other, around 1º difference, it is possible to simultaneously measure multiple modes. This is the case for the A1 mode, which was simultaneously measured with the S0 n the 400 kHz to 750 kHz range. Thanks to the wide bandwidth of the transducers, several modes with the same velocities could be simultaneously measured.

To enhance the captured signals, due to the non-homogeneous transmission efficiency of the transducers over their working range of 200 kHz to 400 kHz and 400 kHz to 800 kHz, the dispersion curves where normalized. Each measurement that was carried out, for each mode and frequency range, was normalized with respect to its maximum voltage. This was done over short frequency ranges of 10 kHz and 25 kHz, to avoid the aforementioned transducer effect. To reduce the noise that arouse from the measurements, the data under 50% of the maximum amplitude was considered as zero. For the curved plate, Figure 3-7 (b), the measured LLW was not as efficient as for the straight section, due to angle scattering, which can be observed to be noisier than the straight plate, Figure 3-7 (a).

The experimental curves were fitted with the analytical dispersion curves calculated with the TMM&SMM mixed model. The initial approximation of the orthotropic elastic properties for the GFRP were taken from [Castaings **2004**]. The estimated values of the properties for both sections are presented in Table 3-1. Observing the dispersion curves calculated with the model and the measured from the GFRP, a difference in the dispersion curves for the straight and curved plate can be observed. This difference can be observed at the frequency at which the velocity of the S0 mode changes. The frequency for this initial change is around 525 kHz for the straight plate, whilst it is at around 575 kHz for the curved section. This difference was not expected for this curve radius, since the behavior of Lamb waves should be equal [Fong **2005**]. However, a simple test measuring the thickness showed the cause for such a disparity. The thickness of the straight and curved were not equal, with 6.66% thickness difference. This variation of 0.2 mm thinner thickness in the curved section, whilst in the range of acceptance for the manufactured part, can cause a huge difference in the estimated properties with guided waves. The calculated curve in Figure 3-7 (b) already includes this difference in the thickness. With the corrected part thickness for the curved section, Table 3-1 shows very small differences in the properties of the straight and curved sections. These differences might be caused by many reasons, like small differences in local density that may have been present in between both areas. This would not be far from what would be expected since less resin with the same amount of fiber would alter the density of the section.

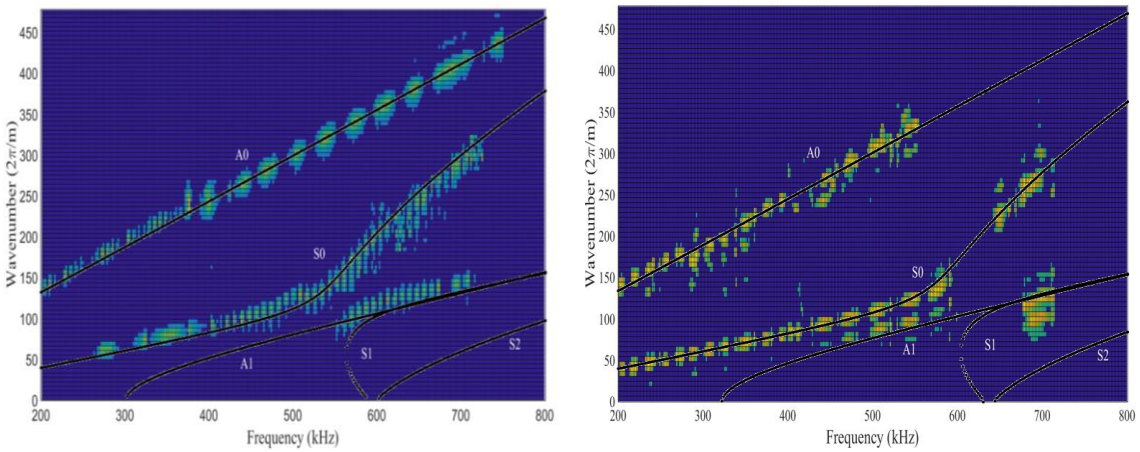

Figure 3-7: Lamb wave measured and calculated dispersion curves of the straight (a) and curved (b) sections of the part.

Table 3-1: Fitted elastic properties for the main direction of the plates.

Section	Thickness (mm)	Density (kg/m^3)	C_{11} (GPa)	C_{13} (GPa)	C_{33} (GPa)	C_{55} (GPa)
Straight	3	1900	49.8	9.1	24.2	6.3
Curved	2.8	1900	50.3	9.3	24.3	6.6

3.3.2 Transducer efficiency: geometry and multimode generation

To evaluate the efficiency of transducers with difference geometry, four pairs of piezocomposite transducers were tested. The transducers sensitivity at their resonance frequency is presented in Table 3-2. The NCG200 focused and unfocused transducers were evaluated at their main resonance frequency of 200 kHz. It can be observed from the sensitivity result that the unfocused transducers show 4-5 dB higher transmission rate at their resonance frequency. The CSIC-300 and NCG500 were tested at 300 kHz, since that was their peak resonance frequencies. It can be observed quite a difference between both the transducers in the efficiency range, since the CSIC transducers showed 22-24 dB improvement compared to the focused ULTRAN ones. The difference in sensitivity was also quite meaningful comparing it with those at 200 kHz, with a minimum of 11 dB.

Observing the results of the four pairs of transducers in Table 3-2, an important detail is observable regarding their resonance frequency. Despite expecting their resonance to be fixed at 200 or 300 kHz, the resonance frequencies had a variation of up

to 15%. This is usually done in wideband transducers to widen the frequency band. Instead of having a single transducer with a wider resonance band, since that reduces the efficiency, each transducer from the pair resonates at a slightly difference frequencies, which increases the bandwidth.

Table 3-2: Sensitivity of the evaluated piezocomposite transducers in pulse-echo.

Excitation frequency (kHz)	**Manufacturer**	**Model**	**Serial Number**	**Resonance frequency (kHz)**	**Sensitivity (dB)**
200 kHz	ULTRAN	NCG200-D19	350317	232	-41
			350318*	174	-40
		NCG200-D19-P50	350350*	207	-45
			350351	175	-45
300 kHz	CSIC	CSIC-300	170*	278	-29
			171	287	-29
	ULTRAN	NCG500-D19-P50	290423	333	-53
			290424*	340	-51

* Used as transmitter to evaluated the efficiency measuring guided modes.

To analyze the efficiency to propagate guided waves, two different incidence angles were tested: 9º, to excite the A0 mode; and 0º, to test if any mode could be excited with the focused or unfocused transducers. In order to test the efficiency generating guided waves, the transducers in Table 3-2 were tested for the two incidence angle scenarios. The transducers with the asterisk in Table 3-2 where used as transmitters, while the rest were used as receivers. The focused and unfocused transducers from ULTRAN where mixed for the test at 200 kHz and the focused ULTRAN and unfocused CSIC transducers where mixed for the 300 kHz test. The combinations of transmitter and receiver transducer can be observed in Table 3-3 and Table 3-4. The transducers from different manufacturers and different geometries where combined to test whether if combining them would provide any advantage, like multimode measurement or improved sensitivity.

For the measurements at 0º incidence angle, or normal incidence angle, no guided mode was measurable. No mode was measurable with any combination of transducers, not even the S0 mode that is generated at around 4º, as seen in Section 3.3.1. The focused transducers either don't have enough aperture to be able to excite angles where LLW are generated or the energy is scattered so much that the transducers are not sensitive enough. The inability to measure anything at a normal angle, even with focused transducers, reduces the possibility of using ACUS without any knowledge on the material properties or the angles where LLW are excited.

At 9º incidence angle, as would be expected from the measurements in Section 3.3.1, the A0 could be measured with all the transducer combinations. The normalized results for the different transducer combinations are shown in Table 3-3 and Table 3-4. The results where normalized at 0 dB for each of the receiver pair. Observing the results of the transmission efficiency measured for the A0 mode, the non-focused transducers were always the most efficient. Since the energy is not scattered over a range of incidence angles, this is the expected behavior. According to the results for the straight plate, Table 3-3, it can be observed that the difference in the transmission efficiency between the focused and the unfocused ULTRAN transducers is between 1 dB to 3 dB. To calculate this difference, the difference in transducer sensitivity was compensated from Table 3-2 (+2 dB for the focused 200 kHz transducer and +12 dB for the focused 300 kHz transducer). The transmission efficiency for ACUS transducer was observed to be inhomogeneous over their working range, in Section 3.3.1. This implies that analyzing the efficiency to generate LLW, the transducer resonance frequency needs to be taken into account. The resonance frequency for each transducer, shown in Table 3-2, differs up to 15% from the theoretical one. Since transmission efficient is uneven over the working frequency range, when the resonance frequency of the transmitter and receiver are close to each other, the efficiency should be increased. The resonance frequency difference causes the difference from the non-focused and focused to be reduced under certain circumstances. Observing for the test at 300 kHz, in Table 3-3, this effect can be observed much clearly. The resonance frequencies of the CSIC and ULTRAN transducers differ up to 68 kHz, whilst less than 10 kHz from their own pair. The unfocused transducers show a higher transmission rate, even with the correction of their sensitivity. Using the CSIC transducers as transmitter and receiver the difference is up to 47 dB better than using the CSIC as transmitter and the ULTRAN as receiver. However, the difference falls to only 8 dB in when the transmitter used is from ULTRAN. Since the difference in the resonance frequency of the ULTRAN and CSIC transducers is of almost 20%, the efficiency of the transmission between the same pair is enhanced.

Comparing the results at the curved section, in Table 3-4, the differences in efficiency were smaller between the focused and unfocused transducers than in the straight section. In the case of the measurements at 200 kHz, the focused and unfocused transducers were virtually identically efficient. The similarity may also be due to the resonance frequency differences. For the measurements at 300 kHz, the difference is

almost as high as for the straight section, with 38 dB better transmission for the unfocused transducers. The smaller difference in efficiency compared with the straight plate might be related to the geometry of the plate and the behavior of the plane wave that in incident to the surface. Since a curved section generated multiple incidence angles in its surface with the plane wave, the energy is dispersed into various angles. Since this dispersion only happens in the curved section for unfocused transducers, it would be expected for their efficiency to be reduced. For the focused transducers, on the other hand, since the wave had already multiple angle components, this effect is not so noticeable. In fact, it was observed the focused transducer, in the same way of unfocused transducers, required to be placed with the adequate incidence angle, 9º in the A0 case. When the angle was slightly changed, the efficiency sharply fell, which may explain why nothing was observable at normal incidence.

Table 3-3: Normalized transmission efficiency of guided modes in the straight section.

Transducer (200 kHz)	**NCG200-D19 (dB)**	**NCG200-D19-P50 (dB)**	**Transducer (300 kHz)**	**CSIC-300 (dB)**	**NCG500-D19-P50 (dB)**
NCG200-D19	0	-3	**CSIC-300**	0	-47
NCG200-D19-P50	0	-1	**NCG500-D19-P50**	0	-8

Table 3-4: Normalized transmission efficiency of guided modes in the curved section.

Transducer (200 kHz)	**NCG200-D19 (dB)**	**NCG200-D19-P50 (dB)**	**Transducer (300 kHz)**	**CSIC-300 (dB)**	**NCG500-D19-P50 (dB)**
NCG200-D19	0	-1	**CSIC-300**	0	-38
NCG200-D19-P50	0	0	**NCG500-D19-P50**	0	-6

With the use of the focused or unfocused transducers, modes with different velocities could not be simultaneously measured. The results showed that the reason for not being able to measure more than one LLW mode might be the low efficiency in both generating and measuring them out of their incidence angles. The hybrid ACUS and 3D-LDV was used to test whether several modes were simultaneously generated in the straight or curved section. The results of the measurement are shown in Figure 3-8.

Figure 3-8 (a) shows the displacement in the propagation direction of the guided waves in the curved section. Figure 3-8 (b) shows the displacement in the thickness direction of the guided waves in the curved section. Figure 3-8 (c) shows the displacement in the propagation direction of the guided waves in the straight section. Figure 3-8 (d) shows the displacement in the thickness direction of the guided waves in the straight section.

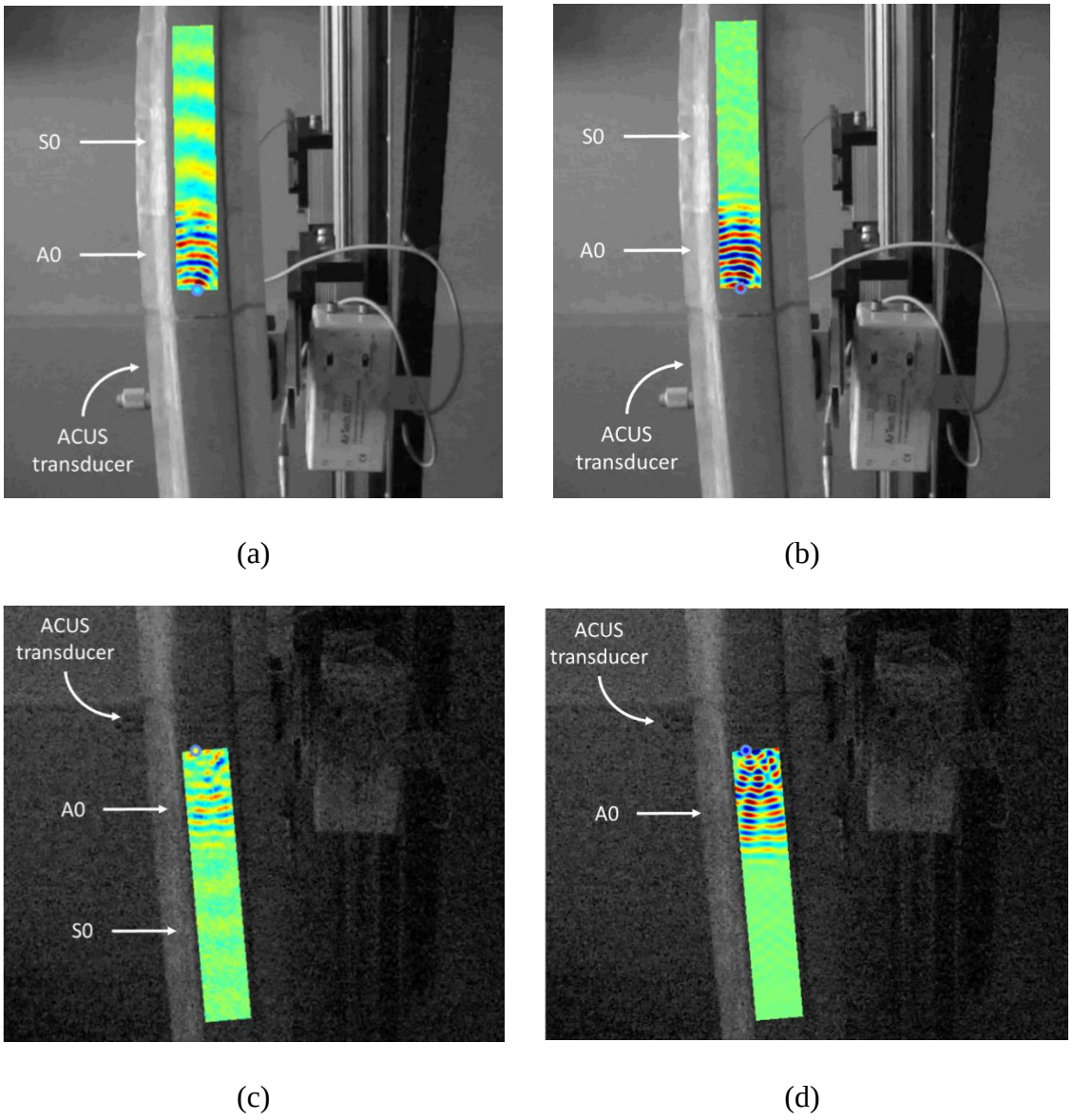

Figure 3-8: Laser measurement of the simultaneous generation of Lamb modes with different velocities in the curved (a,b) and straight (c,d) sections: displacement in propagation direction (a,c) and in the thickness direction (b,d).

In Figure 3-8 (a), most clearly, and (b) and (c), less clearly, two guided modes can be observed. The measurements of multiple modes with different velocities proves that, in fact, several modes can be generated simultaneously. These two modes, the A0 and S0, show not only different velocities but also different amplitudes. The difference in amplitude is related to the attenuation of each mode at a certain frequency, as well as the different efficiency in generating each mode. If several modes with different

velocities are generated, it means that the energy is dispersed into different incidence angles. Since ACUS requires such high sensitivity for the transducers, dissipating the energy does not allow measuring several modes simultaneously. The LDV, compared with ACUS, is more sensitive, since it avoids the transmission losses present at the interface of the plate and the ACUS transducer itself. Moreover, in the case of the 3D-LDV, it is sensitive to the plate displacement in the three axes. This is important since the different Lamb wave modes displace in different direction. In Figure 3-8 (a) and (b), the difference in the particle displacement velocity can be observed for the S0 mode. The S0 mode presents a higher amplitude in Figure 3-8 (a) than it does in Figure 3-8 (b). In fact, in the straight section, Figure 3-8 (c) and (d), this difference is still more clearly observable. In Figure 3-8 (c), the S0 mode can be observed and measured whilst, in Figure 3-8 (d), it is not.

3.4 Conclusions

In this chapter, the effect of the curvature in the guided waves velocity and the efficiency to generate LLW has been theoretically and experimentally evaluated with ACUS and 3D-LDV.

For both sections of the GFRP profile, the straight and the curved sections, the dispersion curves could be obtained over a wide range, from 200 kHz to 800 kHz. The straight section showed better transmission than the curved section. The dispersion curves for the straight and curved section were calculated with the TMM&SMM mixed method, which provided the same results for material properties. The radius of 190 mm of the curved section of the GFRP plate showed no difference in the behavior compared with the straight section. It was observed, however, that changes in the thickness of less than 7%, which might be in the acceptable range for the material, has a far greater effect on the LLW than the curvature.

Comparing focused and unfocused transducers, unfocused transducers showed to be more efficient. Comparing the efficiency to generate guided waves, however, fitting the resonance frequency of the transducers showed to be most critical. Fitting the frequency improved the efficiency of the transducers up to 39 dB. The use of focused transducer did not provide any benefit in order to generate multiple modes. No modes could be generated if normal transmission incidence angle, which would have been most useful. Moreover, the transduction efficiency of focused transducers was observed to decrease if the incidence angle was varied from the same used for unfocused transducers.

With the ACUS set-up LLW with different velocities were not measurable. However, with the use of a hybrid ACUS and 3D-LDV, modes with different velocities were measurable. The measurements made with the 3D-LDV showed that, indeed, several modes were generated in the plate, both in the straight and curved sections. The loss in efficiency due to incidence angle misplacement of ACUS transducers and the requirement to measure efficiently from various angles prevents it.

The 3D-LDV presents clear improvements in sensitivity with respect to ACUS, although it can only be used as a receiver. LDV, specifically the 3D-LDV, measures all the vibrations in the surface of the material, independently of the velocity or frequency, as long as it is inside of the measurement range. However, this advantage is also a disadvantage for small plates. In small plates, the reflection of the wave in the edges is also measured and could lead to noisy measurements. In the case of the ACUS, this noise is greatly limited, because the angle at which the ultrasonic waves are leaking into the air is different from the angle of the transducer. The inability to measure waves with different velocities and directions with ACUS is an advantage in some applications.

Chapter 4

Monitoring the thermal curing of a GFRP with ACUS

The third goal of this thesis is to evaluate the properties of composite materials during curing without contact. Due to the complexity of composite materials and the inability to always access through both sides, inspection methods that are single-sided and can be applied for anisotropic materials are necessary. In this chapter, the use of LLW to monitor the cure process of a GFRP is evaluated. The first section focuses on the theoretical background to model the composite material and simplify its anisotropy. The second section presents the set-up and methodology used. The third section presents the results, whilst the last one shows the conclusions.

4.1 Theoretical background

4.1.1 Micromechanics

Modelling the properties of composite materials can be quite difficult due to their anisotropy. Since FRPs have orthotropic anisotropy at most, the anisotropy level is reduced. This orthotropic anisotropy is defined by nine stiffness tensors that are dependent on the directional properties of the composite. Directly measuring all of those nine tensors with US testing requires measurements in the different directions and in some cases that is not possible. For example, when the part has a plate like geometry, measuring the properties of the fiber direction cannot be directly done, since the transducer size can be bigger than the thickness. Luckily, for FRP materials, the orthotropic anisotropy can be further simplified, assuming a micromechanical model which consists of a combination of the resin and the fiber [Minakuchi **2016**]. With this model, which is used for unidirectional fiber in this case, the directional properties of the composite are dependent on the resin and fiber separately. This model is of special interest in cases like cure monitoring of an FRP. During curing, the properties of the whole composite are changing, but in reality, only the properties of the resin change, since the fiber stays the same. The resin is an isotropic material and the fiber brings the orthotropic anisotropy into the composite material. If the properties of the fiber and the resin are known, the directional elastic Young's modulus (E), shear modulus (G) and Poisson's ratio (ν) of an unidirectional FRP are defined as [Minakuchi **2016**]:

$$E_1 = E_{1_f} V_f + E_m(1 - V_f) + \frac{4 V_f k_f k_m G_m (1 - V_f)\left(\nu_m - \nu_{12_f}\right)^2}{k_m(k_f + G_m) + G_m V_f (k_f - k_m)} \tag{4-1}$$

$$E_2 = E_3 = \frac{1}{(1/4k_T) + (1/4G_{23}) + (\nu_{12}^2/E1)} \tag{4-2}$$

$$G_{12} = G_{13} = G_m \frac{G_{12_f} + G_m + V_f(G_{12_f} - G_m)}{G_{12_f} + G_m - V_f(G_{12_f} - G_m)} \tag{4-3}$$

$$G_{23} = G_m \frac{k_m\left(G_m + G_{23_f}\right) + 2G_{23_f}G_m + V_f k_m\left(G_{23_f} - G_m\right)}{k_m\left(G_{23_f} + G_m\right) + 2G_{23_f}G_m - V_f(k_m + 2G_m)\left(G_{23_f} - G_m\right)} \tag{4-4}$$

$$\nu_{12} = \nu_{13} = \nu_{12_f}V_f + \nu_m(1 - V_f) + \frac{V_f G_m\left(\nu_m - \nu_{12_f}\right)(k_m - k_f)}{k_m(k_f + G_m) + V_f G_m(k_f - k_m)} \tag{4-5}$$

$$\nu_{23} = 1 - (E_2/2k_T) - (2E_2\nu_{12}^2/E_1) \tag{4-6}$$

where

$$G_m = \frac{E_m}{2(1 + \nu_m)} \tag{4-7}$$

$$G_{23_f} = \frac{E_{3_f}}{2\left(1 + \nu_{23_f}\right)} \tag{4-8}$$

$$k_m = \frac{E_m}{2(1 - \nu_m - 2\nu_m^2)} \tag{4-9}$$

$$k_f = \frac{E_{3_f}}{2\left(1 - \nu_{23_f} - \nu_{23_f}^2\right)} \tag{4-10}$$

$$k_T = \frac{k_m(k_f + G_m) + V_f G_m(k_f - k_m)}{(k_f + G_m) - V_f(k_f - k_m)} \tag{4-11}$$

where V_f is the fiber volume content of the FRP and subscripts f and m refer to the fiber and resin respectively. The subscript numbers (1,2,3) represent the direction of the material properties, where 1 represents the direction of the fibers, and 2 and 3 are the transverse directions. These properties are related to the orthotropic elastic tensor as [ABAQUS **2009**]:

$$C_{11} = E_1(1 - \nu_{23}\nu_{32})\Upsilon \tag{4-12}$$

$$C_{22} = E_2(1 - \nu_{13}\nu_{31})\Upsilon \tag{4-13}$$

$$C_{33} = E_3(1 - \nu_{12}\nu_{21})\Upsilon \tag{4-14}$$

$$C_{12} = E_1(\nu_{21} - \nu_{31}\nu_{23})\Upsilon \tag{4-15}$$

$$C_{13} = E_1(\nu_{31} - \nu_{21}\nu_{32})\Upsilon \tag{4-16}$$

$$C_{23} = E_2(\nu_{32} - \nu_{12}\nu_{31})\Upsilon \tag{4-17}$$

$$C_{44} = G_{12} \tag{4-18}$$

$$C_{55} = G_{13} \tag{4-19}$$

$$C_{66} = G_{23} \tag{4-20}$$

where

$$\Upsilon = 1/(1 - \nu_{12}\nu_{21} - \nu_{23}\nu_{32} - \nu_{31}\nu_{13} - 2\nu_{12}\nu_{32}\nu_{13}) \tag{4-21}$$

$$\nu_{\mathrm{ij}}/E_i = \nu_{ji}/E_j \tag{4-22}$$

where $i, j = 1,2,3$.

Using the micromechanics model from Eq. (4-1) to (4-11), there are only two unknowns to define during curing, E_m and ν_m, instead of the nine of a completely unknown orthotropic material.

4.1.2 Mixed TMM & SMM

To model the LLW curves, the micromechanical model in Section 4.1.1 is used, where the material is orthotropic, but only has E_m and ν_m as unknowns. The mixed TMM&SMM shown in Section 3.1.3. is used, without further change in the model but the way the matrix $[C_{ij}]$ is obtained. During curing, to calculate the dispersion curves of the LLW, the matrix $[C_{ij}]$ is adapted and the LLW calculated with the mixed TMM&SMM.

4.2 Set-up and methodology

To monitor the evolution of the orthotropic elastic properties, three GFRP plates consisting of eight quasi-unidirectional glass fiber layers were manually impregnated with VE resin provided by Irurena S.A (IRUVIOL GFR-17 without photo-initiators). Three plates where evaluated to ensure the repeatability of the measurements. Due to the manual impregnation and lack of a mold, the thickness of the plates varied between 3 and 3.4 mm. The resin was accelerated for a resin cure time of five hours at room temperature. After the curing process, a postcure at 100 ºC for one hour was carried out.

Under the GFRP plate a thin, 0.03 mm, plastic sheet was placed. This sheet prevents the coupling of mechanical waves between the GFRP plate and the structure under it. In addition, since the thickness of the plastic film is less than 1% of the thickness of the plate, its effect on the LLW is negligible. The evolution of the curing degree was characterized with a differential scanning calorimeter (DSC) from Mettler Toledo.

To estimate the elastic properties of the FRP material during the curing process, the set-up shown in Figure 4-1 was used. A set-up that consisted of a fully ACUS measurement and a hybrid ACUS-contact US measurement was used. For the fully ACUS, a pair of broadband ACUS transducers with a working range of 200 to 400 kHz manufactured at the CSIC, the same used in Chapter 3, where placed in pitch catch. For the hybrid ACUS-contact, the ACUS transducers was used as a generator and a piezo disc (referred as PZT from now on) was placed in contact with the FRP as a receiver. The ACUS transducers were placed at an oblique and constant angle of 4.5º ± 0.5º during the whole curing process. This angle was selected according to the results of Section 4.3.1, in order to excite the S0 and A1 modes. To drive the transducer the Tektronix AFG-1022 signal generator and the Falco WMA-300 power amplifier were used. A three-pulse square wave tone burst at 300 kHz was used. This waveform maximizes the transmitted wave energy in the 200 kHz to 400 kHz frequency spectrum, which is the working range of the transducers. For the fully ACUS, at the receivers side a Femto HQA-15M-10 T charge amplifier with 10 V/pC gain was used. For the hybrid ACUS-contact, the amplifier of a Panametrics 5077PR was used. To capture the signal of the ACUS and hybrid measurements the Tektronix MDO4104 oscilloscope was used to register the signals. A measurement of the curing was carried out every 15 minutes after 45 minutes of the beginning of the cure.

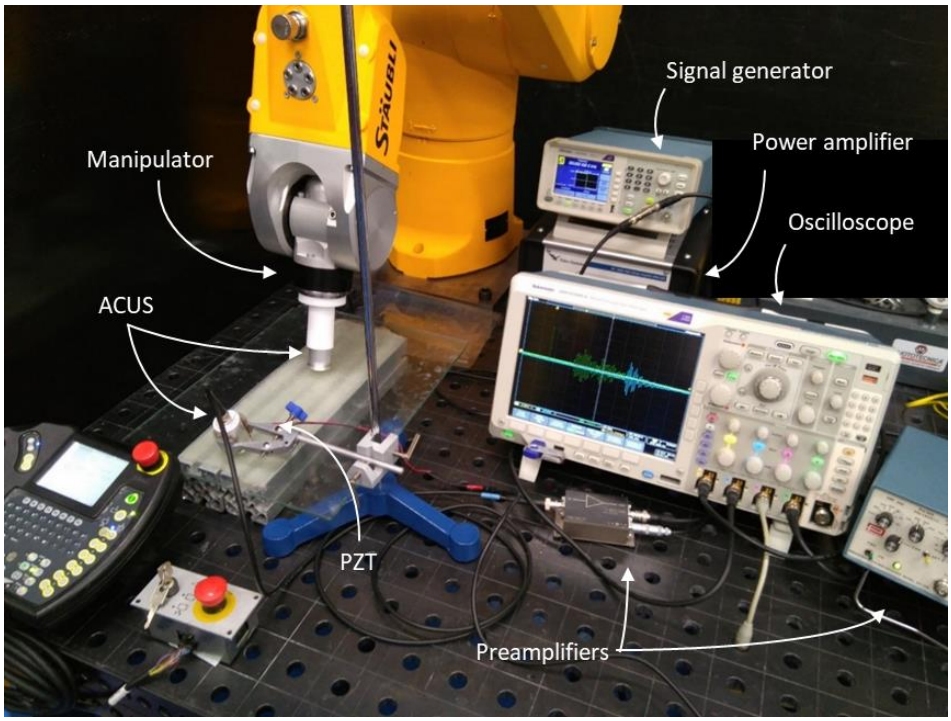

Figure 4-1: Set-up to measure the LLW with a fully ACUS and a PZT receiver.

The measurements made with the ACUS and hybrid measurements were carried out equally. In both cases, the ACUS transducer was used as a generator with both the ACUS and PZT as a receiver. To measure the phase velocity of the LLW it was necessary to displace the ACUS generator, since the PZT in contact could not be displaced. The ACUS generator was displaced in the main direction of the fiber. To maximize the resolution of the spatial frequency, the total measurement distance was 150 mm. The further the total measurement distance, the better the resolution is. However, at the beginning of curing, the signal is highly attenuated and at a greater distance than 150 mm no signal was measurable. The step size was chosen to be 2 mm, since the step size limits the minimum measurable velocity. At 2 mm steps with 150 mm distance, the minimum measurable velocity is 802 m/s at a frequency of 400 kHz. The minimum measured velocity for the propagated modes is more than twice that velocity, as is later observed in Section 4.3.1 and Section 4.3.2. To obtain the dispersion curves of the experimental measurements a 2D-FFT was carried out over the captured data.

To fit the measured dispersion curves with the mixed TMM&SMM, the micromechanical model was used. The properties of the glass fiber [Mounier **2012**] and the thickness (Table 4-1), measured with a micrometer after the curing, were considered constant during curing. The properties of the VE resin, on the other hand, were fitted through a stochastic gradient descent algorithm. The fiber volume content and density of the composite, where fitted once at the first instant where LLW were measurable. The density and fiber volume content of the GFRP were latter measured in several points of the plates according to ASTM D792-08 and ASTM D3171-09 by burn off, respectively. Young's modulus and Poisson's ratio for the VE resin were calculated for each step after LLW were measurable. The initial conditions for the GFRP and the resin are shown in Table 4-1. For the fiber volume content and density, what other authors achieved for hand lay-up was used as an initial reference [Avila **2005**]. For the initial properties of Young's modulus and Poisson's ratio, intermediate values of the properties of the fully cured VE resin where selected [Dominguez-Macaya **2019**].

Table 4-1: Initial parameters of the composite.

Material	**Young's modulus (GPa)**	**Poisson's ratio**	**Density (kg/m^3)**	**Fiber volume content (%)**	**Thickness (mm)**
VE	1.65	0.4	1160	-	-
Glass	72.5	0.2	2550	-	-
GFRP	-	-	1855	50	3.2 ± 0.2

4.3 Results

4.3.1 Sensitivity analysis

Measuring the propagation of guided waves in a curing FRP material can be difficult due to the highly attenuative nature of the material and complex mechanical properties. Simplifying the orthotropic anisotropy with the micromechanical model, where only the resin properties change, reduces the complexity. However, guided waves are highly dispersive and are composed of an infinite number of modes. Selecting which mode or modes is critical to ensure the desired results. Thus, evaluating the variation in the dispersion curves with the change in the properties of the resin is necessary, mainly using such a technique as ACUS LLW.

LLW do not propagated in composite materials, at least, until after the gelation point has been reached, but more usually measured after vitrification. Considering the micromechanical simplification of the composite material the change of the mechanical properties are exclusively due to the resin curing process. The VE resin's Young's modulus and Poisson's ratio are the most interesting terms, since they change the most. To evaluate the change in LLW dispersion curves depending on both of these mechanical properties, two scenarios were evaluated theoretically with the mixed TMM&SMM method in the frequency range going from 200 kHz to 400 kHz. The thickness selected for both scenarios was 3.2 mm, to ensure that the theoretical analysis and the experimental measurements (Section 4.3.2) were the same. At the first scenario, the Young's modulus is varied between 3.3 GPa, which corresponds to the material fully cured [Dominguez-Macaya **2019**], and 1.65 GPa for a partially cured material. The difference in Young's modulus between both plates is 1.65 GPa, and will be called as ΔE from now on. In this scenario, Poisson's ratio is kept constant at 0.37. At the second scenario, Poisson's ratio is changed for these two curing degrees, assuming that the Poisson's ratio is 0.37 for the fully cured material [Dominguez-Macaya **2019**], and 0.45 for the partially cured one. The difference in Poisson's ratio between both plates is 0.08 and will be called as $\Delta\nu$ from now on. For this second scenario, Young's modulus is kept constant with a value of 1.65 GPa, to ensure that the dispersion curves are in the inspection range. The sensitivity is established as the rate of change of the wavenumber (in percentage) in the ΔE or $\Delta\nu$ range.

Figure 4-2 shows the dispersion curves for the partially and fully cured GFRP plates with different Young's modulus. From Figure 4-2, the first thing that can be observed is that all of the modes that are visible present a similar behavior in the partially cured and completely cured plates. When the material stiffens, the modes response increases in frequency. This is why in the partially cured plate five modes are visible (A0, S0, A1, S1 and S2), whereas only four are visible in the fully cured plate (A0, S0, A1 and S1). From Figure 4-2 it can also be observed that the S1 mode is superimposed with the A1 mode. This makes the S1 mode undistinguishable from the A1 mode. Therefore, observing this, the modes that could be potentially used to evaluate the evolution of the material properties are the A0, S0 and A1 modes.

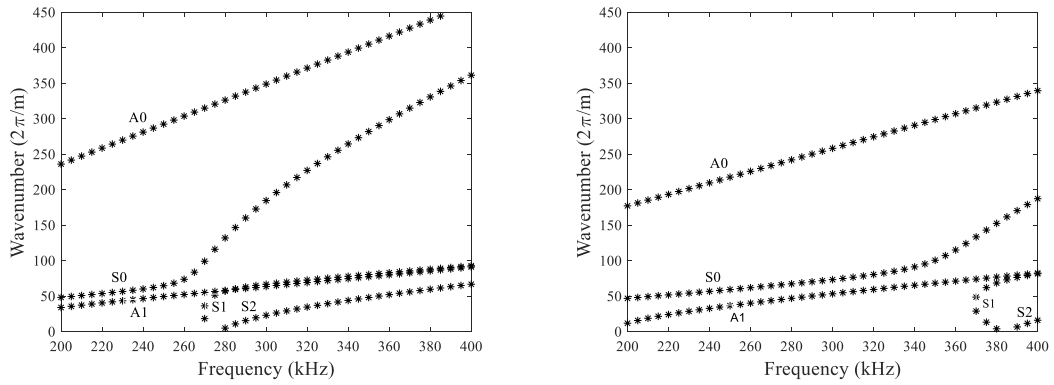

Figure 4-2: Dispersion curves for the partially (a) and fully (b) cured GFRP for ΔE.

The lowest order mode (A0) is observed to change significantly between the partially and fully cured GFRP, as shown in Figure 4-3. The slope of the A0 mode in both plates is constant. In the case of the A0 mode, the slope of the wavenumber indicates that it's a constant velocity. This can be calculated due to the relationship between the velocity, frequency and wavenumber of the mode. Since the slopes and velocities of both plates are constant, the sensitivity can be calculated in the whole working range. The sensitivity for the wavenumber of the A0 mode between the partially and fully cured plates is ~30%.

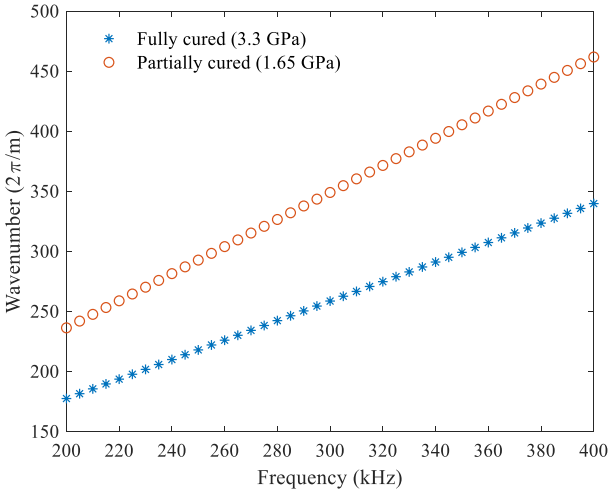

Figure 4-3: A0 mode in the partially and fully cured GFRP for ΔE.

The S0 mode for the partially and fully cured plate is shown in Figure 4-4. To calculate the sensitivity of the S0 mode, it is necessary to separate it into two regions. These regions are divided by an inflexion point. The inflexion point is the frequency at which the S0 mode's slope changes significantly. The inflexion point for the partially cured plate is at 260 kHz, whereas for the fully cured plate it is around 350 kHz. The first region is set before the inflexion point of the partially cured plate. In this region, the wavenumber of both of the plates have a constant slope. The velocity of the S0

mode in this region is constant, similarly to the A0 mode. The sensitivity of the wavenumber in this region is less than 3% between both plates. Between the two regions, is the inflexion point itself. The inflexion point can be observed to change much more significantly than the first region. The sensitivity of the inflexion point is ~34% between both plates. The second region is set after the inflexion point. In this region, the mode changes its shape. This happens due to a change in the velocity of the S0 mode. Evaluating the sensitivity of this region is not meaningful, since the mode is displaced in frequency and, therefore, has different shape at each frequency. However, despite not quantifying the sensitivity, the change is as meaningful as the inflexion point itself and needs to be taken into consideration.

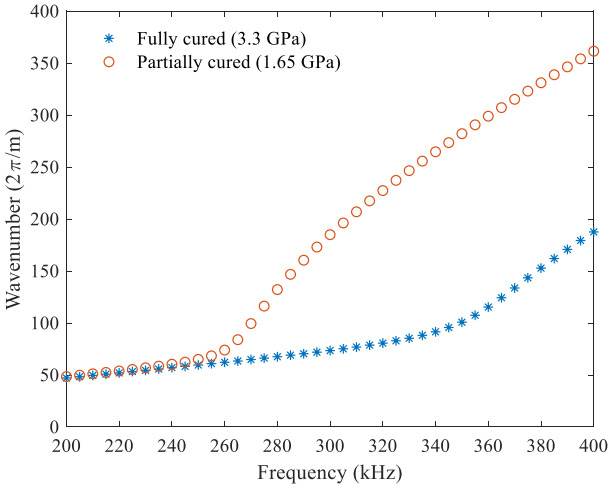

Figure 4-4: S0 mode in the partially and fully cured GFRP for ΔE.

The A1 mode for both plates is shown in Figure 4-5. The partially cured plate has a constant slope, whilst the shape of the fully cured shows a steeper slope at the beginning. It should be pointed out that in the case of the A1, the constant slope does not indicate a constant velocity. Simply relating the wavenumber and the velocity, this fact can be observed. The shape of the A1 mode is the same in both plates after 300 kHz, which simplifies the calculation of the sensitivity. The sensitivity of the wavenumber over 300 kHz is 12%.

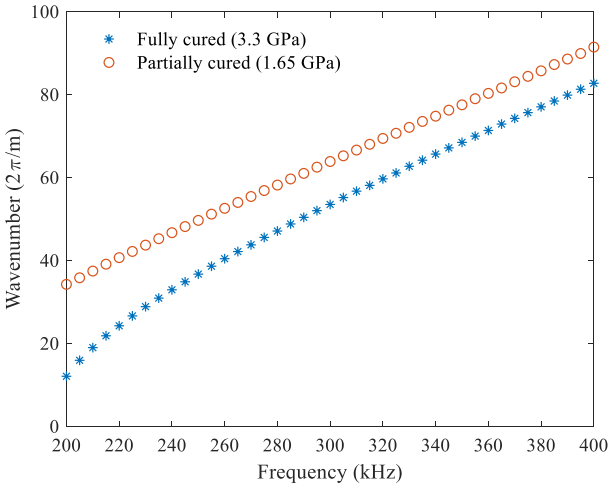

Figure 4-5: A1 mode in the partially and fully cured GFRP for ΔE.

Figure 4-6 shows the dispersion curves for the partially and fully cured GFRP plates with different Poisson's ratio. Like in the first scenario, five modes are visible (A0, S0, A1, S1 and S2). All the modes behave similarly for the partially and fully cured plate. The S1 mode at its lowest frequency is the only one with a different shape. In fact, it can be observed that only the S0 mode changes significantly. Since the A0, S0 and A1 where the most useful in the previous scenarios, these are also evaluated in this case.

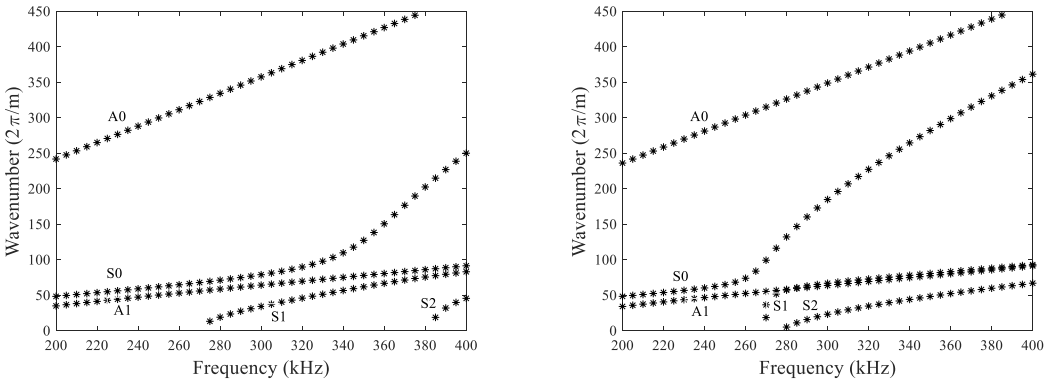

(a) (b)

Figure 4-6: Dispersion curves for the partially (a) and fully (b) cured GFRP for $\Delta\nu$.

The A0 modes for the partially and fully cured plates are shown in Figure 4-7. The A0 mode for both plates behaves very similarly. The sensitivity of the A0 mode is less than 5% of its value. It is important to notice that Poisson's ratio affects acoustic properties in a different way from Young's modulus, since it determines the ability of shear waves to propagate through the material.

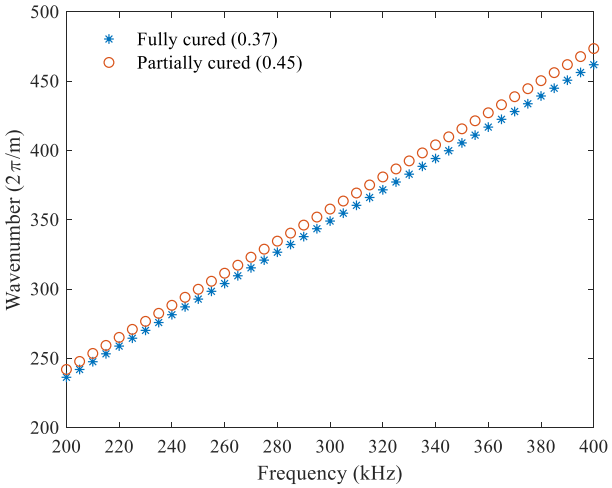

Figure 4-7: A0 mode in the partially and fully cured GFRP for $\Delta\nu$.

The S0 mode for the partially and fully cured plate is shown in Figure 4-8. The S0 mode is evaluated like in the previous scenario with two regions, separated by the inflexion point. The first region is up to 260 kHz. In this region, the difference between both plates is close to 0%, thus, the sensitivity is not estimated. Regarding the inflexion point, the variation is from 340 kHz at the partially cured plate whilst it's 260 kHz at the fully cured. The sensitivity for this region is of 30%. With the second region the same happens as in the previous scenario. Thus, this is not quantified.

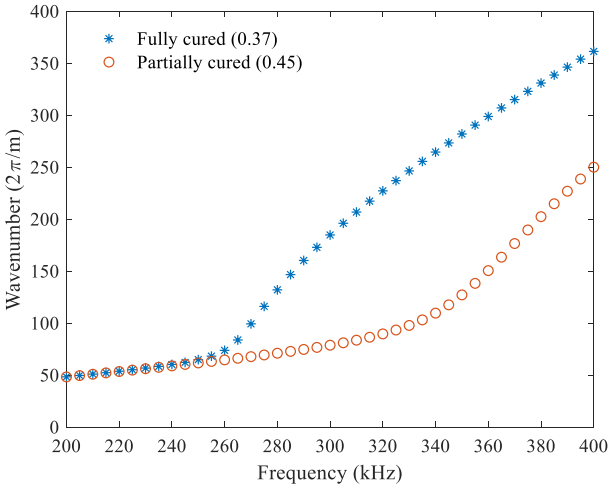

Figure 4-8: S0 mode in the partially and fully cured GFRP for $\Delta\nu$.

The A1 mode for both plates is shown in Figure 4-9. Similarly to the A0 mode, the A1 modes changes very little. The sensitivity is barely 1%.

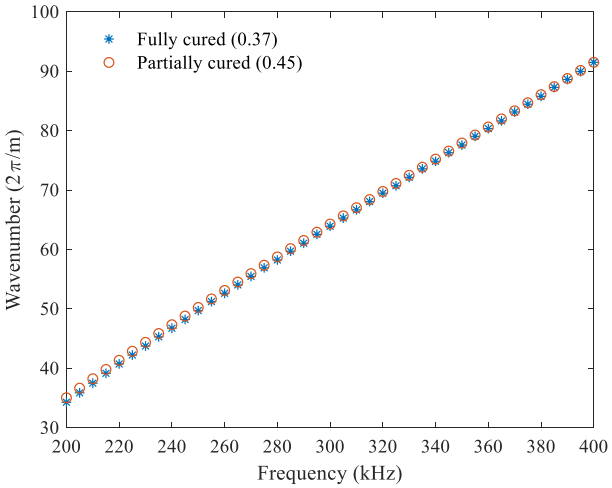

Figure 4-9: A1 mode in the partially and fully cured GFRP for $\Delta\nu$.

Observing the variation in the LLW modes for both scenarios, the following conclusions can be obtained:

- The A0 mode can be used to monitor the evolution of the resin's Young's modulus. However, it cannot be used to monitor Poisson's ratio.
- The S0 mode can be used to monitor the evolution of the resin's Young's modulus and the Poisson's ratio. However, not all of the regions of the S0 mode provide useful information.
    - At the first region, before the inflexion point, the response of the S0 mode is independent to the resin's properties. This means that it is strictly dependent on the fiber reinforcement.
    - At the inflexion point, the S0 mode changes with Young's and Poisson's ratio. The increase in Young's modulus increases the frequency of the inflexion point and the decrease in Poisson's ratio decreases the frequency. Since these events occur during curing, both properties may counteract each other.
    - The second region, which is directly affected by the inflexion point, behaves like the inflexion point.
- The A1 mode can be used to monitor the evolution of the resin's Young's modulus. However, it cannot be used to monitor Poisson's ratio.

Taking into account these previous statements, theoretically, the most useful mode to monitor is the S0 mode, specifically around its inflexion point. Additionally, from the experimental point of view, this is also the most practical choice. Since the S0 mode shows the same velocity up to the inflexion point, independently from the properties of the resin, the angle of the ACUS transducer can be fixed. This solves the issue of having to find the precise angle at every single measurement. Furthermore, since the velocity before the inflexion point is only dependent on the reinforcement, the volume of fiber can be estimated, without the need to measure it afterwards. Besides,

measuring with this velocity/angle for the S0 mode, the A1 mode can also be obtained simultaneously. Observing these advantages, the S0 mode and A1 modes were selected around the inflexion point of the S0 mode.

4.3.2 Cure monitoring

The dispersion curves of the LLW of the GFRP plate have been evaluated from the point where the resin was a viscous liquid to the end of curing, where it can be considered as a solid. Some snapshots of the response of the plate in the 200 to 400 kHz range during curing are shown in Figure 4-10. At the beginning of the curing, minute 45 in Figure 4-10 (a), the first measurement was made. No guided wave was measured. However, a wave propagating in the plate was measurable with the contact and ACUS transducers. The velocity of the propagated wave in the three plates evaluated was constant at 4850 ± 40 m/s. The wave measured with the resin in viscous liquid state must be a longitudinal wave, since shear waves would be greatly attenuate in the material.

As the properties of the resin begin to change, the first event that it is observed is the increase in the attenuation of the measured signal. From minute 45 on, the attenuation of the resin increases without changes in the velocity. The maximum in attenuation is reached at 2:00 h (Figure 4-10 (b)). At this point in time, the longitudinal wave was hardly observable with the ACUS transducer, although it was always measured with the PZT.

After the maximum attenuation point is crossed, a change in the dispersion curves of the plate is observable. Measured velocity decreased from 4850 ± 40 m/s to 4450 ± 55 m/s, which represents a 10% reduction. This variation indicates a change in the velocity of the measured longitudinal wave or that guided waves start to be propagated. If LLW were propagated in the plate, since it is in the earliest curing stages, the measured mode might be the A1 or a higher mode. This would be a consequence of the reduced stiffness. However, due to the limited frequency range inspected, it is not possible to observe the inflexion point of the S0 mode. Additionally, there are too many unknowns and limited information, the plate's properties cannot be calculated yet.

At 2:45 h, LLW can finally be measured inside the inspection range. As it can be observed in Figure 4-10 (c), the inflexion point of the S0 mode is at 240 kHz. At that point in the frequency, the S0 mode changes its velocity and is no longer excited by the transducer. On the other hand, the velocity of the A1 mode is close to the S0 mode before the inflexion point and, therefore, has an similar excitation angle (around 1º or 2º less compared to the S0 mode). Therefore, from 200 kHz to 240 kHz the S0 and from 240 kHz to 360 kHz the A1 modes can be measured. From the 2:45 h measurement onwards, Figure 4-10 (c) to Figure 4-10 (f), the evolution of the inflexion point and the S0 mode and A1 mode can be observed. The inflexion point shows the most significant variation from 240 kHz at 2:45 h to 300 kHz at 5:00 h. The A1 mode also changes, although it is not as easily observable at plain sight. With the evolution of the dispersion

curves, the properties of the resin during curing and the volume of fiber can be calculated.

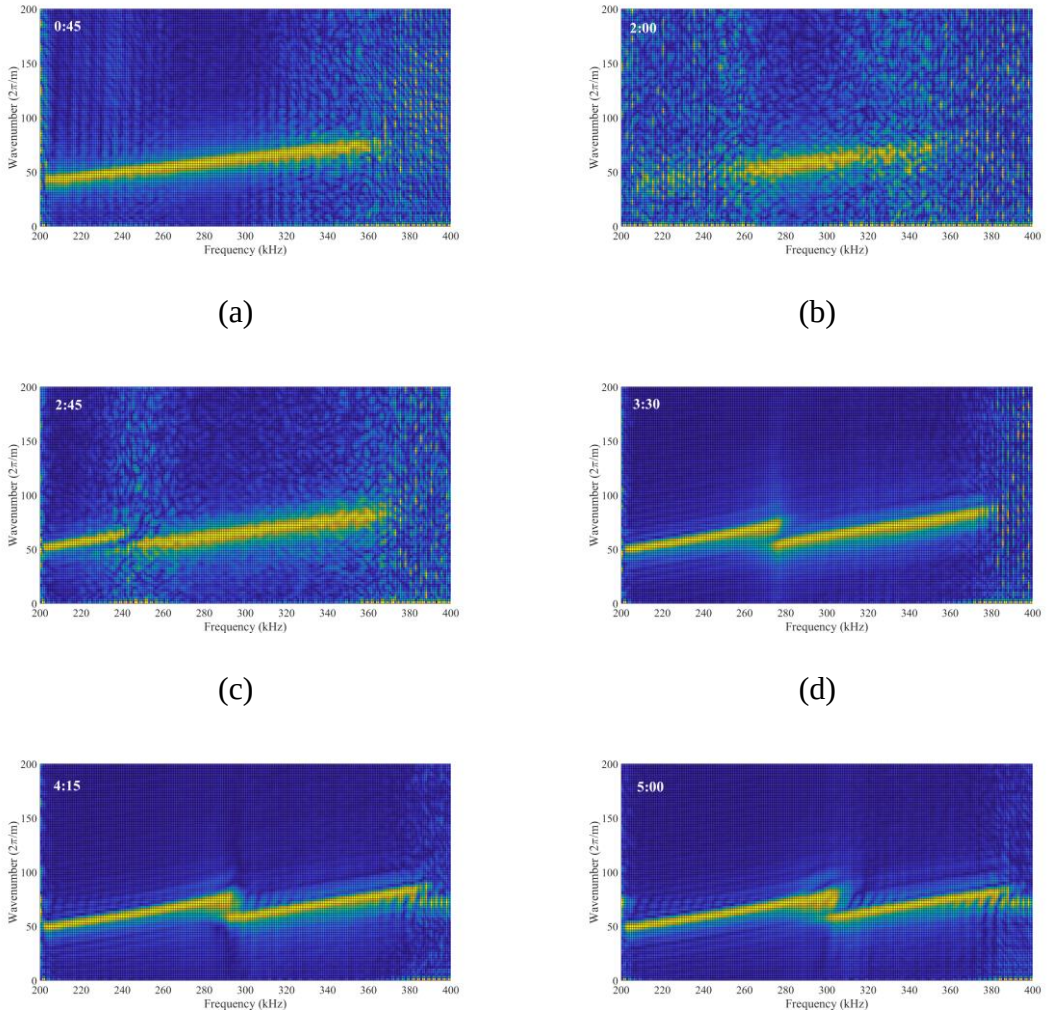

Figure 4-10: Frequency response change of the GFRP measured with the ACUS during the cure: (a) 0:45 h, (b) 2:00 h, (c) 2:45 h, (d) 3:30 h, (e) 4:15 h and (f) 5:00 h.

Between Figure 4-10 (c) and (f), more measurements were carried out. However, for cleanliness, only four images have been shown. For all the measurements carried out, the properties of the resin were be obtained. At 2:45 hours, the fiber volume content, density, as well as the properties of the resin were fitted with the dispersion curves, for the three plates. The fiber volume content is the most critical parameter for the S0 mode, especially before the inflexion point. When the theoretically obtained LLW where fitted with the results, the fiber volume and density were estimated, since they are interrelated. The fiber volume content and density obtained for the GFRP was 40 ± 1% and 1716 ± 14 kg/m^3 respectively. The fiber volume content measured with the ASTM D3171-09 was 40.1 ± 1%. The density measured with the ASTM D792-08 was 1693 ± 30 kg/m^3. The difference between the ACUS and ASTM tests was around 1%, which shows that LLW are efficient to measure the fiber volume content and density.

The similarity in fiber volume content and density in the three plates indicates that the manufacturing process was consistent. With the fiber volume content estimated, the evolution of the properties of the resin was evaluated.

Figure 4-11 shows the evolution of VE resin's Young's modulus. At the beginning of the measurement period, a fast increase in Young's modulus can be observed, whilst once the 5 h mark is reached, it is stabilized. The measured Young's modulus at the end of the curing process is 2.65 GPa, which is lower than the nominal value (3.3 GPa). This difference is due to the fact that the DoC at room temperature is far from 100% (Figure 4-13). Comparing the results from the ACUS and PZT for each of the measurements, the consistency is high with a mean difference of less than 3% between contact and non-contact measurements. Comparing the results of the different plates, the mean difference is less than 10%, but at some points, it rises up to 15%. These differences are caused by the changes of the room temperature in the different test.

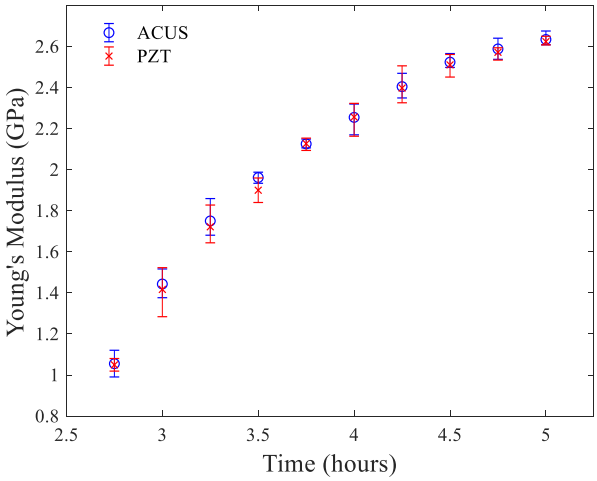

Figure 4-11: Evolution of the Young's modulus of the VE.

The evolution of the VE resin's Poisson's ratio is shown in Figure 4-12. The evolution of Poisson's ratio is measurable from 0.432 to 0.367. The mean error in Poisson's ratio between the three plates is less than 3%, whilst the error between the ACUS and PZT is around 1% only. These differences are smaller than those for Young's modulus and are related to the smaller ratio of change of Poisson's ratio. During curing, it can be observed that Poisson's ratio changes in a fast and sharp way. At the lowest curing degrees, where the S0 and A1 modes are the closest, Poisson's ratio is the highest. Nevertheless, the fast separation of the modes shows a fast variation of the properties.

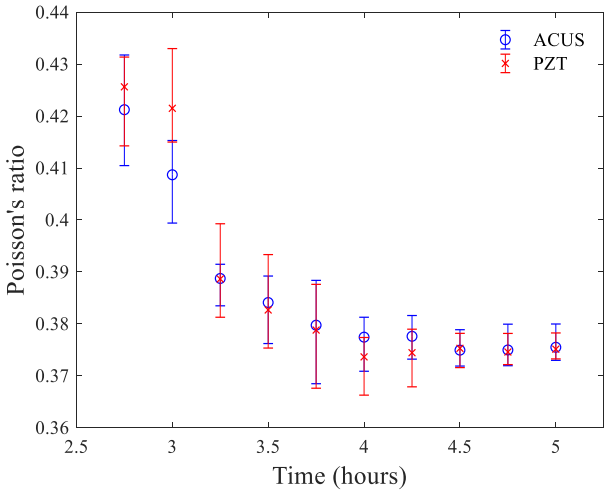

Figure 4-12: Evolution of Poisson's ratio of the VE.

The evolution of the VE's Young's modulus (Figure 4-11) and Poisson's ratio (Figure 4-12) has also been evaluated with respect to the DoC of the sample measured with the DSC (Figure 4-13 and Figure 4-14). Figure 4-13 shows the evolution of the DoC and Young's modulus during curing time and Figure 4-14 shows the evolution of Young's modulus with respect to the DoC. The curing process begins at around 30 minutes and reaches a DoC of 55% after 5 hours. 50% of the DoC is done in the first 2:45 hours, whilst the other 5% is done in over 2 hours. The point of 50% DoC is also the approximate moment at which LLW are finally measurable. Young's modulus is observed to change from 1 GPa to 2.6 GPa in a range of 5% DoC. It must be pointed out that the evolution of the elastic properties and the DoC are out-of-phase. This behavior is similar to what other researchers have observed [Ruiz **2005**] and is clearly observed in both figures.

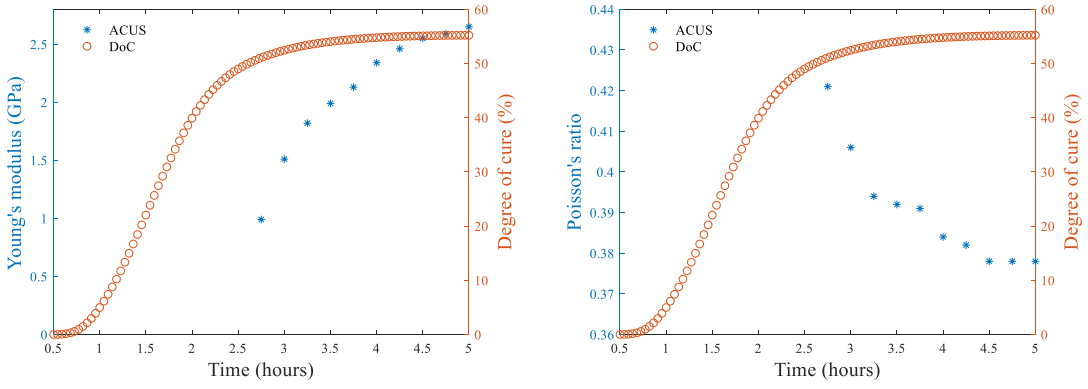

(a) (b)

Figure 4-13: Evolution of (a) Young's modulus and (b) Poisson's ratio compared with the DoC.

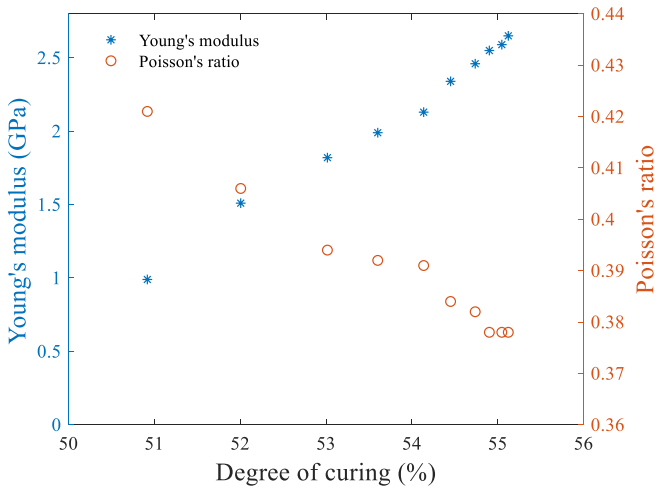

Figure 4-14: Evolution of Young's modulus and Poisson's ratio with the DoC.

To observe the differences that the variation in the resin properties causes in the composite material, the properties of the composite at three points are shown in Table 4-2. The three points are: at the first measurement of LLW, at the end of the curing at room temperature and after the post-curing. The matrix coefficients that are least dependent to curing process are the C_{11}, C_{12} and C_{23}. The rate of change for the C_{11} is the lowest, with just less than a 10%. As it would be expected, the properties in the direction of the fiber are more dependent on the fiber than on the resin. A variation in the fiber volume content, on the other hand, would affect this property the most, due to the aforementioned dependency. The C_{12} is also amongst the least dependent on curing, with a change of under 40%. The variation is four times that of C_{11} since the components of the C_{12} are the fiber direction and the thickness or lateral side. As the fibers are unidirectionally oriented, properties in directions 2 and 3 are equal. The C_{23} also changes very little, despite being almost completely dependent on the resin properties. The increase in the Young's modulus is counteracted by the reduction in Poisson's ratio. At the postcure, however, since there is no change in Poisson's ratio, C_{23} changes a 32%. The rest of the properties, C_{22}, C_{44} and C_{55}, are more dependent on this change. The C_{22}, which is the property that depends almost entirely on the resin, is the one that changes the most in absolute numbers. A change of 4 GPa is translated into a change of 66% in its stiffness, since the fiber does almost no work in this direction. The greatest relative change, yet, is observed in C_{44} and C_{55}. The C_{44} and C_{55} are strictly related to the shear properties of the composite material in the directions in which they act, unlike the $C_{11}, C_{12}, \dots, C_{33}$ coefficients, which are interrelated as observed in Eq. (4-12) to (4-20). The rate of change of C_{44} and C_{55} are 130% and 138% respectively. This is due to the fact that in these directions the contribution of the fibers to the properties of the composite is the highest. However, all the changes calculated above are below the rate of change of the VE's Young's modulus, which changes up to 260%.

A clear conclusion can be obtained from the data in Table 4-2. In composite material, the fiber is usually the most important part of the material, since it gives the stiffness to the composite. However, in order to evaluate the composite as a whole, it is necessary to focus on those directional properties where the fiber has the least effect. This means that monitoring the C_{44} and C_{55} coefficients is the most efficient procedure to obtain the right properties of the composite.

Table 4-2: Properties of the GFRP.

Time	C_{11} (GPa)	C_{22} (GPa)	C_{12} (GPa)	C_{23} (GPa)	C_{44} (GPa)	C_{55} (GPa)
2:45 hours	30.79 ± 0.18	6.44 ± 0.12	3.53 ± 0.07	4.38 ± 0.08	1.06 ± 0.03	1.14 ± 0.02
5:00 hours	31.35 ± 0.1	8.06 ± 0.08	3.67 ± 0.05	4.31 ± 0.06	1.87 ± 0.02	2.04 ± 0.02
Post cure	32.68 ± 0.11	10.73 ± 0.1	4.89 ± 0.08	5.72 ± 0.06	2.5 ± 0.03	2.72 ± 0.02

4.4 Conclusions

In this chapter, ACUS LLW have been used to monitor the thermal curing of a GFRP. This technique has proved to be useful to monitor the evolution of the properties of the resin and the whole composite with the use a micromechanics model without the need of contact between the part and the transducers. The selection of the modes to excite was critical in order to have enough signal to noise ratio, where the modes most dependent on the fibers probed to be the most viable.

It has been observed that Lamb waves were not measurable until high degrees of conversion were reached. Once this point was reached, however, significant changes in the properties were measurable, in a more sensitive way than the DSC technique.

Comparing the hybrid and fully ACUS inspection method, the same results were obtained. The hybrid method did not provide any advantage besides an increased signal level when the attenuation was at its highest point. The fully ACUS method allows focusing in a single area of the measurement zone due to the angle selection. With the measurement of multiple modes with the ACUS, the VE's properties can be directly measured.

The DoC obtained at room temperature was only of 55%, but it was enough to measure the variation in the properties of the composite.

However, the method has certain limitations. First, the attenuation was not taken into account in the model, which may affect both the acoustic and the mechanical properties. Second, the hypothesis of the micromechanics model for the composite material is used. Whereas for the high degrees of conversion this principle is fulfilled, at lower ones the model may not be usable. Due to the great attenuation of the resin and lack of shear strength, no guided wave can be propagated during the lowest curing states. A micromechanical model of propagation which considers the resin as a highly viscous fluid could solve this.

Chapter 5
Summary and conclusions

We conclude this thesis by stating the conclusions and the main contributions obtained from the whole research carried out during this doctoral thesis. Finally, a set of tasks that would complement and enhance the work done in this doctoral thesis are proposed.

5.1 Conclusions

This thesis evaluates the evolution of elastic properties of composite materials with non-contact techniques, focusing in ACUS. Inspection techniques nowadays are not able to give insight on the material properties without contact. Moreover, obtaining these properties during the cure process can further improve the manufacturing in the future.

In the first part of this thesis an air-coupled ultrasonic technique to monitor the evolution of the viscoelastic properties of a resin during the ultraviolet curing process was developed. It was observed that this technique worked for fast processes and was able to provide information on longitudinal and shear properties. Limits were also found since this technique can only measure shear properties at high curing degrees. It was also noted that resonant air-coupled ultrasonics can only be used with non-hollow materials and require access through both sides of the part.

In the second part, the elastic properties of composite materials with leaky lamb waves were evaluated. It has been observed that generating and measuring multiple modes with air-coupled ultrasonics, whether for straight or curved parts, it is not viable with the efficiency that transducers have nowadays. However, using laser ultrasonics it was possible to measure them, which indicates that it is a matter of transmission losses. It was also observed that plane transducers were more efficient than focused ones, which provided no advantage. Straight and curved parts also presented equal propagation properties for Lamb waves for large radii parts.

When the curing of composite materials was evaluated, for glass fiber reinforced polymers, the selection of the modes to evaluate was observed to be critical. The modes dependence on the resin properties would be the most interesting to evaluate it, but the high attenuation limits this possibility. Evaluating the properties of the resin through the effect of the resin in the section of the guided waves that are mostly dependent on the fiber showed good results. The properties were efficiently measured and validated with a contact sensor.

Air-coupled ultrasonics proved to be efficient to measure the mechanical properties with the techniques developed. The choice between which technique to use would depend upon the requirements of the process to evaluate.

5.2 Suggestions for Further Research

Many issues described in this PhD dissertation can be addressed in the future as improvements and extensions of the current work. These are some of the suggestions for further research:

- Testing the techniques developed for different materials such as carbon fiber reinforced polymers, resins with particles, adhesives, and so on.
- Evaluating the effect of the temperature over different degrees of curing could give more insight over the behavior of the material during the bending process for 3D ultraviolet pultrusion. In the case of application of theses technique in molded processes this information could be used or to ensure correct demolding.
- Measurements in the real 3D ultraviolet curing process would be necessary to solve other problems that can arise from industrialization of these techniques.
- More automatized measurement systems are required to apply techniques such as leaky Lamb wave monitoring to faster curing processes.
- The future development of ultrasonic arrays or the use of laser ultrasonic to measure would further improve measurement speed and provide more information.
- Different geometries, with sharper curves and even edges need to be evaluated. Other propagation techniques different from the transfer matrix or stable transfer matrix may be required to model. Techniques like semi-analytic finite elements could be used.
- Air-coupled ultrasonic inspection cannot only be used to evaluate properties but also for defects. Delamination, voids or uncured areas could be tackled with the application of various techniques that are usually applied in contact US.

References

ABAQUS (**2009**). *Defining orthotropic elasticity by specifying the terms in the elastic stiffness matrix*, Dassault Systèmes, Available: http://130.149.89.49:2080/v6.9/books/usb/default.htm?startat=pt05ch18s02abm02.html, (date last viewed: 11-Nov-19). Retrieved November 11, 2019, from http://130.149.89.49:2080/v6.9/books/usb/default.htm?startat=pt05ch18s02abm02.html

Adam, A. J. L. (**2011**). "Review of near-field Terahertz measurement methods and their applications: How to achieve sub-wavelength resolution at THz frequencies," J. Infrared, Millimeter, Terahertz Waves, **32**, 976–1019. doi:10.1007/s10762-011-9809-2

Aggelis, D. G., and Paipetis, A. S. (**2012**). "Monitoring of resin curing and hardening by ultrasound," Constr. Build. Mater., **26**, 755–760. doi:10.1016/j.conbuildmat.2011.06.084

Aldridge, M., Wineman, A., Waas, A., and Kieffer, J. (**2014**). "In Situ Analysis of the Relationship between Cure Kinetics and the Mechanical Modulus of an Epoxy Resin," Macromolecules, **47**, 8368–8376. doi:10.1021/ma501441c

Alleyne, D. N., and Cawley, P. (**1990**). "A 2-dimensional Fourier transform method for the quantitative measurement of Lamb modes," IEEE Symp. Ultrason., IEEE, Honolulu, 1143–1146. doi:10.1109/ULTSYM.1990.171541

Alleyne, D. N., and Cawley, P. (**1992**). "Optimization of lamb wave inspection techniques," NDT E Int., **25**, 11–22. doi:10.1016/0963-8695(92)90003-Y

Álvarez-Arenas, T. E. G. (**2003**). "Air-coupled ultrasonic spectroscopy for the study of membrane filters," J. Memb. Sci., **213**, 195–207. doi:10.1016/S0376-7388(02)00527-6

Álvarez-Arenas, T. E. G. (**2010**). "Simultaneous determination of the ultrasound velocity and the thickness of solid plates from the analysis of thickness resonances using air-coupled ultrasound," Ultrasonics, **50**, 104–109. doi:10.1016/j.ultras.2009.09.009

Álvarez-Arenas, T. E. G., and Camacho, J. (**2019**). "Air-Coupled and Resonant Pulse-Echo Ultrasonic Technique," Sensors, **19**, 2221. doi:10.3390/s19102221

Álvarez-Arenas, T. E. G., Montero de Espinosa, F. R., Moner-Girona, M., Rodríguez, E., Roig, A., and Molins, E. (**2002**). "Viscoelasticity of silica aerogels at ultrasonic frequencies," Appl. Phys. Lett., **81**, 1198–1200. doi:10.1063/1.1499225

Álvarez-Arenas, T. E. G., Sancho-Knapik, D., Peguero-Pina, J. J., Gómez-Arroyo, A., and Gil-Pelegrín, E. (**2018**). "Non-contact ultrasonic resonant spectroscopy resolves the elastic properties of layered plant tissues," Appl. Phys. Lett., **113**, 253704. doi:10.1063/1.5064517

An, Y.-K., Park, B., and Sohn, H. (**2013**). “Complete noncontact laser ultrasonic imaging for automated crack visualization in a plate,” Smart Mater. Struct., **22**, 025022. doi:10.1088/0964-1726/22/2/025022

Antonucci, V., Giordano, M., Hsiao, K.-T., and Advani, S. G. (**2002**). “A methodology to reduce thermal gradients due to the exothermic reactions in composites processing,” Int. J. Heat Mass Transf., **45**, 1675–1684. doi:10.1016/S0017-9310(01)00266-6

APC International, L. (**2002**). *Piezoelectric ceramics: principles and applications*, APC International, 114 pages.

Asay, J. R., and Guenther, A. H. (**1967**). “Experimental determination of ultrasonic wave velocities in plastics as functions of temperature. IV. Shear velocities in common plastics,” J. Appl. Polym. Sci., **11**, 1087–1100. doi:10.1002/app.1967.070110708

Auld, B. A. (**1973**). *Acoustic fields and waves in solids*, Рипол Классик,.

Avila, A. F., and Morais, D. T. S. (**2005**). “A multiscale investigation based on variance analysis for hand lay-up composite manufacturing,” Compos. Sci. Technol., **65**, 827–838. doi:10.1016/j.compscitech.2004.05.021

Bader, M. G. (**2002**). “Selection of composite materials and manufacturing routes for cost-effective performance,” Compos. Part A Appl. Sci. Manuf., **33**, 913–934. doi:10.1016/S1359-835X(02)00044-1

Balvers, J. M., Chen, J., Octeau, M. A., Bersee, H. E. N., and Yousefpour, A. (**2009**). “Through-Thickness Cure Monitoring of Thick Advanced Composites Using Dielectric Sensors,” Proc. 17th Int. Conf. Compos. Mater., 10. Retrieved from http://www.iccm-central.org/Proceedings/ICCM17proceedings/Additional Papers/C4.8 Octeau.pdf

Bernassau, A., Hutson, D., Demore, C. E. M., Flynn, D., Amalou, F., Parry, J., McAneny, J., et al. (**2009**). “Progress towards wafer-scale fabrication of ultrasound arrays for real-time high-resolution biomedical imaging,” Sens. Rev., **29**, 333–338. doi:10.1108/02602280910986575

Bickerton, S., Stadtfeld, H. C., Steiner, K. V., and Advani, S. G. (**2001**). “Design and application of actively controlled injection schemes for resin-transfer molding,” Compos. Sci. Technol., **61**, 1625–1637. doi:10.1016/S0266-3538(01)00064-1

Caronti, A., Caliano, G., Carotenuto, R., Savoia, A., Pappalardo, M., Cianci, E., and Foglietti, V. (**2006**). “Capacitive micromachined ultrasonic transducer (CMUT) arrays for medical imaging,” Microelectronics J., **37**, 770–777. doi:10.1016/j.mejo.2005.10.012

Castaings, M., Bacon, C., Hosten, B., and Predoi, M. V. (**2004**). “Finite element predictions for the dynamic response of thermo-viscoelastic material structures,” J. Acoust. Soc. Am., **115**, 1125–1133. doi:10.1121/1.1639332

Castaings, M., and Cawley, P. (**1996**). “The generation, propagation, and detection of

Lamb waves in plates using air-coupled ultrasonic transducers," J. Acoust. Soc. Am., **100**, 3070–3077. doi:10.1121/1.417193

Castaings, M., and Hosten, B. (**1994**). "Delta operator technique to improve the Thomson–Haskell-method stability for propagation in multilayered anisotropic absorbing plates," J. Acoust. Soc. Am., **95**, 1931–1941. doi:10.1121/1.408707

Castaings, M., and Hosten, B. (**2001**). "Lamb and SH waves generated and detected by air-coupled ultrasonic transducers in composite material plates," NDT E Int., **34**, 249–258. doi:10.1016/S0963-8695(00)00065-7

Castaings, M., and Hosten, B. (**2003**). "Guided waves propagating in sandwich structures made of anisotropic, viscoelastic, composite materials," J. Acoust. Soc. Am., **113**, 2622–2634. doi:10.1121/1.1562913

Castaings, M., Hosten, B., and Kundu, T. (**2000**). "Inversion of ultrasonic, plane-wave transmission data in composite plates to infer viscoelastic material properties," NDT E Int., **33**, 377–392. doi:10.1016/S0963-8695(00)00004-9

Challis, R. E., Alper, T., Freemantle, R. J., Crean, G., and Zhang, D. (**1993**). "Acoustic wave velocities in ceramics and other materials measured by a broadband goniometric method," Rev. Sci. Instrum., **64**, 1271–1273. doi:10.1063/1.1144078

Chan, C. W., and Cawley, P. (**1998**). "Lamb waves in highly attenuative plastic plates," J. Acoust. Soc. Am., **104**, 874–881. doi:10.1121/1.423332

Cheeke, J. D. N. (**2017**). *Fundamentals and applications of ultrasonic waves, second edition*, (C. Press, Ed.) Fundam. Appl. Ultrason. Waves, Second Ed., 1–484 pages. doi:10.1201/b12260

Chimenti, D. E. (**2014**). "Review of air-coupled ultrasonic materials characterization," Ultrasonics, **54**, 1804–1816. doi:10.1016/j.ultras.2014.02.006

Chokanandsombat, Y., and Sirisinha, C. (**2013**). "MgO and ZnO as reinforcing fillers in cured polychloroprene rubber," J. Appl. Polym. Sci., **128**, 2533–2540. doi:10.1002/app.38579

Cielo, P., Krapez, J. C., Cole, K. C., and Vaudreuil, G. (**1989**). *Method and apparatus for evaluating the degree of cure in polymeric composites*, United States of America patent, 4874948, (US Patent 4,874,948). Retrieved from https://www.google.com/patents/US4874948

Cobbold, R. S. C. (**2006**). *Foundations of Biomedical Ultrasound*, Oxford Univ. Press, 832 pages.

Cuevas, E., García, C., Hernandez, S., Álvarez-Arenas, T. E. G., and Cañada, M. (**2013**). "Non destructive testing for non cured composites: Air coupled Ultrasounds and Thermography," 5th Int. Symp. NDT Aerosp., Singapore, 13–15.

Dahmen, S., Ketata, H., Ben Ghozlen, M. H., and Hosten, B. (**2010**). "Elastic constants measurement of anisotropic Olivier wood plates using air-coupled transducers generated Lamb wave and ultrasonic bulk wave," Ultrasonics, **50**, 502–507.

doi:10.1016/j.ultras.2009.10.014

Deschamps, M. (**1996**). “Reflection and refraction of the inhomogeneous plane wave,” Acoust. Interact. With Submerg. Elastic Struct. Part I Acoust. Scatt. Reson., pp. 164–206. doi:10.1142/9789812830593_0006

Deschamps, M., and Hosten, B. (**1992**). “The effects of viscoelasticity on the reflection and transmission of ultrasonic waves by an orthotropic plate,” J. Acoust. Soc. Am., **91**, 2007–2015. doi:10.1121/1.403685

Dominguez-Macaya, A., Álvarez-Arenas, T. E. G., Saenz-Dominguez, I., Tena, I., Aurrekoetxea, J., and Iturrospe, A. (**2019**). “Monitoring the evolution of stiffness during ultraviolet curing of a vinyl ester resin with quasi-normal air-coupled ultrasonic spectroscopy,” Polym. Test., **80**, 106112. doi:10.1016/j.polymertesting.2019.106112

Dominguez-Macaya, A., Romero, J., Vicente, J., Iturrospe, A., Abete, J. M., Martiín De La Escalera, F., and Alcaide, Á. (**2016**). “A novel self-tuning method for Lamb wave inspection of plate-like structures,” EWSHM 2016, Bilbo, 1–11. Retrieved from https://www.ndt.net/events/EWSHM2016/app/content/Paper/37_Dominguez-Macaya.pdf

Dominguez-Macaya, A., Saenz-Dominguez, I., Abete, J. M., Aurrekoetxea, J., and Iturrospe, A. (**2018**). “In-process ultrasonics inspection method for ultraviolet (UV) out of die curing pultrusion process,” 12th ECNDT, Gothenburg, 1–7. Retrieved from https://www.ndt.net/article/ecndt2018/papers/ecndt-0544-2018.pdf

Dunkers, J. P., Lenhart, J. L., Kueh, S. R., van Zanten, J. H., Advani, S. G., and Parnas, R. S. (**2001**). “Fiber optic flow and cure sensing for liquid composite molding,” Opt. Lasers Eng., **35**, 91–104. doi:10.1016/S0143-8166(00)00110-X

EPTA (**2018**). “Attractive long-term prospects for pultruded composites.,” Retrieved from https://pultruders.org/pdf_news/1_WPC 2018 report_final.pdf

Farinas, M. D., Alvarez-Arenas, T. E. G., Cuevas Aguado, E., and Garcia Merino, M. (**2013**). “Non-contact ultrasonic inspection of CFRP prepregs for aeronautical applications during lay-up fabrication,” 2013 IEEE Int. Ultrason. Symp., IEEE, 1590–1593. doi:10.1109/ULTSYM.2013.0405

Farinas, M. D., Calas, H., and Alvarez-Arenas, T. E. G. (**2012**). “Visualization of lamb wave propagation in uncured CFRP and curved surfaces using air-coupled ultrasound,” 2012 IEEE Int. Ultrason. Symp., IEEE, 1429–1432. doi:10.1109/ULTSYM.2012.0357

Fariñas, M. D., Sancho-Knapik, D., Peguero-Pina, J. J., Gil-Pelegrín, E., and Álvarez-Arenas, T. E. G. (**2013**). “Shear waves in vegetal tissues at ultrasonic frequencies,” Appl. Phys. Lett., **102**, 103702. doi:10.1063/1.4795785

Fink, B. K., Don, R. C., and Gillespie Jr, J. W. (**1999**). *Development of a Distributed Direct Current Sensor System for Intelligent Resin Transfer Moulding* Army Res. Lab., 51 pages. Retrieved from https://apps.dtic.mil/dtic/tr/fulltext/u2/a370973.pdf

Fischer, B. (**2016**). “Optical microphone hears ultrasound,” Nat. Photonics, **10**, 356–358. doi:10.1038/nphoton.2016.95

Fong, K. L. J. (**2005**). *A Study Of Curvature Effects On Guided Elastic Waves* Imperial College London, 206 pages. Retrieved from http://www3.imperial.ac.uk/pls/portallive/docs/1/50545698.PDF

Fraser, D. B., and LeCraw, R. C. (**1964**). “Novel Method of Measuring Elastic and Anelastic Properties of Solids,” Rev. Sci. Instrum., **35**, 1113–1115. doi:10.1063/1.1718976

Di Fratta, C., Klunker, F., and Ermanni, P. (**2013**). “A methodology for flow-front estimation in LCM processes based on pressure sensors,” Compos. Part A Appl. Sci. Manuf., **47**, 1–11. doi:10.1016/j.compositesa.2012.11.008

Gaal, M., Bartusch, J., Schadow, F., Beck, U., Daschewski, M., and Kreutzbruck, M. (**2016a**). “Airborne ultrasonic systems for one-sided inspection using thermoacoustic transmitters,” 2016 IEEE Int. Ultrason. Symp., IEEE, 1–4. doi:10.1109/ULTSYM.2016.7728787

Gaal, M., Daschewski, M., Bartusch, J., Schadow, F., Dohse, E., Kreutzbruck, M., Weise, M., et al. (**2016b**). “Novel air-coupled ultrasonic transducer combining the thermoacoustic with the piezoelectric effect,” 19th World Conf. Non-Destructive Test. 2016,.

Garschke, C., Weimer, C., Parlevliet, P. P., and Fox, B. L. (**2012**). “Out-of-autoclave cure cycle study of a resin film infusion process using in situ process monitoring,” Compos. Part A Appl. Sci. Manuf., **43**, 935–944. doi:10.1016/j.compositesa.2012.01.003

Giacchetta, R., Bueno, G., Moreno, J. M., and Cruza, J. F. (**2015**). “Nuthic: Non-contact ultrasound inspection machine of highly integrated composite parts,” 7 th Int. Symp. NDT Aerosp., Retrieved from http://2015.ndt-aerospace.com/Portals/aerospace2015/BB/we2a6.pdf. Retrieved from http://2015.ndt-aerospace.com/Portals/aerospace2015/BB/we2a6.pdf

Giurgiutiu, V. (**2015**). *Structural health monitoring of aerospace composites*, Academic Press, New York, 454 pages.

Govignon, Q., Bickerton, S., and Kelly, P. (**2013**). “Experimental investigation into the post-filling stage of the resin infusion process,” J. Compos. Mater., **47**, 1479–1492. doi:10.1177/0021998312448500

Hosten, B. (**1991**). “Reflection and transmission of acoustic plane waves on an immersed orthotropic and viscoelastic solid layer,” J. Acoust. Soc. Am., **89**, 2745–2752. doi:10.1121/1.400685

Hosten, B., and Castaings, M. (**1993a**). “Validation at Lower Frequencies of the Effective Elastic Constants Measurements for Orthotropic Composite Materials,” Rev. Prog. Quant. Nondestruct. Eval., Vol. 12, pp. 1193–1199. doi:10.1007/978-1-4615-2848-7_153

Hosten, B., and Castaings, M. (**1993b**). “Transfer matrix of multilayered absorbing and anisotropic media. Measurements and simulations of ultrasonic wave propagation through composite materials,” J. Acoust. Soc. Am., **94**, 1488–1495. doi:10.1121/1.408152

Hosten, B., Deschamps, M., and Tittmann, B. R. (**1987**). “Inhomogeneous wave generation and propagation in lossy anisotropic solids. Application to the characterization of viscoelastic composite materials,” J. Acoust. Soc. Am., **82**, 1763–1770. doi:10.1121/1.395170

Hosten, B., Hutchins, D. A., and Schindel, D. W. (**1996**). “Measurement of elastic constants in composite materials using air-coupled ultrasonic bulk waves,” J. Acoust. Soc. Am., **99**, 2116–2123. doi:10.1121/1.415398

Hsiao, K.-T., Little, R., Restrepo, O., and Minaie, B. (**2006**). “A study of direct cure kinetics characterization during liquid composite molding,” Compos. Part A Appl. Sci. Manuf., **37**, 925–933. doi:10.1016/j.compositesa.2005.01.019

Iriarte, G. F., Rodríguez, J. G., and Calle, F. (**2010**). “Synthesis of c-axis oriented AlN thin films on different substrates: A review,” Mater. Res. Bull., **45**, 1039–1045. doi:10.1016/j.materresbull.2010.05.035

Jager, A., Wright, W. M. D., Kupnik, M., Hinrichs, J., Allevato, G., Sachsenweger, M., Kadel, S., et al. (**2019**). “Non-contact ultrasound with optimum electronic steering angle to excite Lamb waves in thin metal sheets for mechanical stress measurements,” 2019 IEEE Int. Ultrason. Symp., IEEE, Glasgow, 924–927. doi:10.1109/ULTSYM.2019.8925900

Jepsen, P. U., Cooke, D. G., and Koch, M. (**2011**). “Terahertz spectroscopy and imaging - Modern techniques and applications,” Laser Photon. Rev., **5**, 124–166. doi:10.1002/lpor.201000011

Jung, K., and Jin Kang, T. (**2007**). “Cure Monitoring and Internal Strain Measurement of 3-D Hybrid Braided Composites using Fiber Bragg Grating Sensor,” J. Compos. Mater., **41**, 1499–1519. doi:10.1177/0021998306068088

Kalamkarov, A. L., Fitzgerald, S. B., and MacDonald, D. O. (**1999**). “The use of Fabry Perot fiber optic sensors to monitor residual strains during pultrusion of FRP composites,” Compos. Part B Eng., **30**, 167–175. doi:10.1016/S1359-8368(98)00052-3

Kamal, A., and Giurgiutiu, V. (**2014**). “Stiffness Transfer Matrix Method (STMM) for stable dispersion curves solution in anisotropic composites,” In T. Kundu (Ed.), Heal. Monit. Struct. Biol. Syst. 2014, 906410. doi:10.1117/12.2044789

Karim, M. R., Mal, A. K., and Bar-Cohen, Y. (**1990**). “Inversion of leaky Lamb wave data by simplex algorithm,” J. Acoust. Soc. Am., **88**, 482–491. doi:https://doi.org/10.1121/1.399927

Kister, G., and Dossi, E. (**2015**). “Cure monitoring of CFRP composites by dynamic mechanical analyser,” Polym. Test., **47**, 71–78. doi:10.1016/j.polymertesting.2015.08.009

Konstantopoulos, S., Fauster, E., and Schledjewski, R. (**2014**). "Monitoring the production of FRP composites: A review of in-line sensing methods," Express Polym. Lett., **8**, 823–840. doi:10.3144/expresspolymlett.2014.84

Krautkrämer, J., and Krautkrämer, H. (**1990**). "Ultrasonic Testing by Determination of Material Properties," Ultrason. Test. Mater., Springer Berlin Heidelberg, Berlin, Heidelberg, pp. 528–550. doi:10.1007/978-3-662-10680-8_34

Kundu, T. (**2012**). *Ultrasonic and Electromagnetic NDE for Structure and Material Characterization*, CRC Press, 890 pages. doi:10.1201/b12268

Lawrence, J. M., Hsiao, K.-T., Don, R. C., Simacek, P., Estrada, G., Sozer, E. M., Stadtfeld, H. C., et al. (**2002**). "An approach to couple mold design and on-line control to manufacture complex composite parts by resin transfer molding," Compos. Part A Appl. Sci. Manuf., **33**, 981–990. doi:10.1016/S1359-835X(02)00043-X

Legault, M. (**2015**). *In-mold sensors: In-situ process monitoring for RTM*, CompositesWorld, Available: https://www.compositesworld.com/articles/in-mold-sensors-in-situ-process-monitoring-for-rtm, (date last viewed: 01-Jan-20). Retrieved January 1, 2020, from https://www.compositesworld.com/articles/in-mold-sensors-in-situ-process-monitoring-for-rtm

Leisure, R. G., and Willis, F. A. (**1997**). "Resonant ultrasound spectroscopy," J. Phys. Condens. Matter, **9**, 6001–6029. doi:10.1088/0953-8984/9/28/002

Li, G., and Gladden, J. R. (**2010**). "High Temperature Resonant Ultrasound Spectroscopy: A Review," Int. J. Spectrosc., **2010**, 1–13. doi:10.1155/2010/206362

Li, G., Lee-Sullivan, P., and Thring, R. W. (**2000**). "Determination of activation energy for glass transition of an epoxy adhesive using dynamic mechanical analysis," J. Therm. Anal. Calorim., **60**, 377–390. doi:https://doi.org/10.1023/A:1010120921582

Li, Z., and Meng, Z. (**2016**). "A Review of the Radio Frequency Non-destructive Testing for Carbon-fibre Composites," Meas. Sci. Rev., **16**, 68–76. doi:10.1515/msr-2016-0010

Liebers, N., Raddatz, F., and Schadow, F. (**2012**). "Effective and flexible ultrasound sensors for cure monitoring for industrial composites production," Dtsch. Luft- und Raumfahrtkongress 2012,.

Lionetto, F., and Maffezzoli, A. (**2013**). "Monitoring the Cure State of Thermosetting Resins by Ultrasound," Materials (Basel)., **6**, 3783–3804. doi:10.3390/ma6093783

Lionetto, F., Tarzia, A., Coluccia, M., and Maffezzoli, A. (**2007a**). "Air-Coupled Ultrasonic Cure Monitoring of Unsaturated Polyester Resins," Macromol. Symp., **247**, 50–58. doi:10.1002/masy.200750107

Lionetto, F., Tarzia, A., and Maffezzoli, A. (**2007b**). "Air-Coupled Ultrasound: A Novel Technique for Monitoring the Curing of Thermosetting Matrices," IEEE Trans. Ultrason. Ferroelectr. Freq. Control, **54**, 1437–1444. doi:10.1109/TUFFC.2007.404

Lowe, M. J. S. (**1995**). “Matrix techniques for modeling ultrasonic waves in multilayered media,” IEEE Trans. Ultrason. Ferroelectr. Freq. Control, **42**, 525–542. doi:10.1109/58.393096

Madigosky, W., and Fiorito, R. (**1979**). “Modal resonance analysis of acoustic transmission and reflection losses in viscoelastic plates,” J. Acoust. Soc. Am., **65**, 1105–1115. doi:10.1121/1.382774

Martin, J. (**2000**). “Study of the curing process of a vinyl ester resin by means of TSR and DMTA,” Polymer (Guildf)., **41**, 4203–4211. doi:10.1016/S0032-3861(99)00631-X

Mesogitis, T. S., Skordos, A. A., and Long, A. C. (**2014**). “Uncertainty in the manufacturing of fibrous thermosetting composites: A review,” Compos. Part A Appl. Sci. Manuf., **57**, 67–75. doi:10.1016/j.compositesa.2013.11.004

Migliori, A., Darling, T. W., Baiardo, J. P., and Freibert, F. (**2001**). “Resonant ultrasound spectroscopy (RUS),” Exp. Methods Phys. Sci., Vol. 39, pp. 189–220. doi:10.1016/S1079-4042(01)80088-6

Migliori, A., and Maynard, J. D. (**2005**). “Implementation of a modern resonant ultrasound spectroscopy system for the measurement of the elastic moduli of small solid specimens,” Rev. Sci. Instrum., **76**, 121301(1–7). doi:10.1063/1.2140494

Migliori, A., Sarrao, J. L., Visscher, W. M., Bell, T. M., Lei, M., Fisk, Z., and Leisure, R. G. (**1993**). “Resonant ultrasound spectroscopic techniques for measurement of the elastic moduli of solids,” Phys. B Condens. Matter, **183**, 1–24. doi:10.1016/0921-4526(93)90048-B

Minakuchi, S., Niwa, S., Takagaki, K., and Takeda, N. (**2016**). “Composite cure simulation scheme fully integrating internal strain measurement,” Compos. Part A Appl. Sci. Manuf., **84**, 53–63. doi:10.1016/j.compositesa.2016.01.001

Mounier, D., Poilane, C., Bucher, C., and Picart, P. (**2012**). “Evaluation of transverse elastic properties of fibers used in composite materials by laser resonant ultrasound spectroscopy,” Proc. Acoust. 2012 Nantes Conf., 1247–1250. Retrieved from https://hal.archives-ouvertes.fr/hal-00811303

Naftaly, M., and Miles, R. E. (**2007**). “Terahertz Time-Domain Spectroscopy for Material Characterization,” Proc. IEEE, **95**, 1658–1665. doi:10.1109/JPROC.2007.898835

Nakamura, K. (**2012**). *Ultrasonic transducers: Materials and design for sensors, actuators and medical applications*, Woodhead Publishing Limited.

Nakamura, N., Ogi, H., and Hirao, M. (**2015**). “Review on Acoustic Transducers for Resonant Ultrasound Spectroscopy,” JOM, **67**, 1849–1855. doi:10.1007/s11837-015-1457-x

Ohno, I. (**1976**). “Free vibration of a rectangular parallelepiped crystal and its application to determination of elastic constants of orthorhombic crystals.,” J. Phys. Earth, **24**, 355–379. doi:10.4294/jpe1952.24.355

Ospald, F., Zouaghi, W., Beigang, R., Matheis, C., Jonuscheit, J., Recur, B., Guillet, J., et al. (**2013**). "Aeronautics composite material inspection with a terahertz time-domain spectroscopy system," Opt. Eng., **53**, 031208. doi:10.1117/1.OE.53.3.031208

Performance Composites Inc. (**2017**). *Fiberglass and Composite Material Design Guide*, Available: http://www.performancecomposites.com/about-composites-technical-info/122-designing-with-fiberglass.html, (date last viewed: 01-Jan-20). Retrieved January 1, 2020, from http://www.performancecomposites.com/about-composites-technical-info/122-designing-with-fiberglass.html

Premix (**2013**). *Why Composites?*, Available: https://www.premix.com/why-composites/adv-composites.php#targetText=Advantages of Composites,more miles to the gallon)., (date last viewed: 19-Feb-19). Retrieved February 19, 2019, from https://www.premix.com/why-composites/adv-composites.php#targetText=Advantages of Composites,more miles to the gallon).

Qiao, J., Amirkhizi, A. V., Schaaf, K., Nemat-Nasser, S., and Wu, G. (**2011**). "Dynamic mechanical and ultrasonic properties of polyurea," Mech. Mater., **43**, 598–607. doi:10.1016/j.mechmat.2011.06.012

Redo-Sanchez, A., Karpowicz, N., Xu, J., and Zhang, X.-C. (**2006**). "Damage and defect inspection with terahertz waves," 4th Int. Work. Ultrason. Adv. Methods Nondestruct. Test. Mater. Charact., 67–78. Retrieved from https://www.ndt.net/search/docs.php3?id=3416

Roberts, S. S. J., and Davidson, R. (**1991**). "Mechanical Properties of Composite Materials Containing Embedded Fibre Optic Sensors," Proc. SPIE - Int. Soc. Opt. Eng., **1588**, 326–341.

Rokhlin, S. I., Bolland, T. K., and Adler, L. (**1986**). "Reflection and refraction of elastic waves on a plane interface between two generally anisotropic media," J. Acoust. Soc. Am., **79**, 906–918. doi:10.1121/1.393764

Ruiz, E., and Trochu, F. (**2005**). "Numerical analysis of cure temperature and internal stresses in thin and thick RTM parts," Compos. Part A Appl. Sci. Manuf., **36**, 806–826. doi:10.1016/j.compositesa.2004.10.021

Saenz-Dominguez, I., Tena, I., Sarrionandia, M., Torre, J., and Aurrekoetxea, J. (**2018**). "Effect of ultraviolet curing kinetics on the mechanical properties of out of die pultruded vinyl ester composites," Compos. Part A Appl. Sci. Manuf., **109**, 280–289. doi:10.1016/j.compositesa.2018.03.015

Sancho-Knapik, D., Calas, H., Peguero-Pina, J. J., Ramos Fernandez, A., Gil-Pelegrin, E., and Alvarez-Arenas, T. E. G. (**2012**). "Air-coupled ultrasonic resonant spectroscopy for the study of the relationship between plant leaves' elasticity and their water content," IEEE Trans. Ultrason. Ferroelectr. Freq. Control, **59**, 319–325. doi:10.1109/TUFFC.2012.2194

Schindel, D. W., Hutchins, D. A., Lichun Zou, and Sayer, M. (**1995**). "The design and characterization of micromachined air-coupled capacitance transducers," IEEE Trans. Ultrason. Ferroelectr. Freq. Control, **42**, 42–50. doi:10.1109/58.368314

Sedlák, P., Landa, M., Seiner, H., Bicanova, L., and Heller, L. (**2008**). "Non-Contact Resonant Ultrasound Spectroscopy for Elastic Constants Measurement," 1st Int. Symp. Laser Ultrason. Sci. Technol. Appl. Montr. Canada, Retrieved from https://www.ndt.net/article/laser-ut2008/papers/Sedlak LU2008.pdf. Retrieved from https://www.ndt.net/article/laser-ut2008/papers/Sedlak LU2008.pdf

Selfridge, A. R. (**1985**). "Approximate Material Properties in Isotropic Materials," IEEE Trans. Sonics Ultrason., **32**, 381–394. doi:10.1109/T-SU.1985.31608

Sirkis, J. S., and Dasgupta, A. (**1995**). "Optical fiber/composite interaction mechanics," Fiber Opt. smart Struct.,.

Sloan, J. (**2018**). "CompositesWorld 2018 Operations Report," CompositesWorld, Retrieved from https://www.compositesworld.com/articles/compositesworld-2018-operations-report. Retrieved from https://www.compositesworld.com/articles/compositesworld-2018-operations-report

Sommer, S., Probst, T., Kraus, E., Baudrit, B., Town, G. E., and Koch, M. (**2016**). "Cure monitoring of two-component epoxy adhesives by terahertz time-domain spectroscopy," Polym. Sci. Ser. B, **58**, 769–776. doi:10.1134/S1560090416060154

Tena, I. (**2015**). *Pultrusión de perfiles 3d en base al curado ultravioleta fuera del molde y sistemas de tirado por robot* Mondragon Unibertsitatea, 224 pages.

Tena, I., Esnaola, A., Sarrionandia, M., Ulacia, I., Torre, J., and Aurrekoetxea, J. (**2015**). "Out of die ultraviolet cured pultrusion for automotive crash structures," Compos. Part B Eng., **79**, 209–216. doi:10.1016/j.compositesb.2015.04.044

Tena, I., Sarrionandia, M., Aurrekoetxea, J., and Torre, J. (**2013**). "Monitorizado del curado ultravioleta (UV) de un compuesto poliéster reforzado con fibra de vidrio," MATCOMP2013, 1–6. Retrieved from https://synthesites.com/resources/files/UV-curing- MATERIALES COMPUESTOS 13- MondragonUniveristy.pdf

Tena, I., Sarrionandia, M., Aurrekoetxea, J., and Torre, J. (**2014**). "Selection of led or conventional UV lamp based on the composite thickness," 16th Eur. Conf. Compos. Mater. ECCM 2014, 22–26. Retrieved from http://www.escm.eu.org/eccm16/assets/0689.pdf

Tena, I., Sarrionandia, M., Torre, J., and Aurrekoetxea, J. (**2016**). "The effect of process parameters on ultraviolet cured out of die bent pultrusion process," Compos. Part B Eng., **89**, 9–17. doi:10.1016/j.compositesb.2015.11.027

Terahertz wave technology, (**2016**). Available: https://www.hamamatsu.com/eu/en/technology/lifephotonics/BasicResearch/TerahertzWaveTechnology/index.html, (date last viewed: 07-Feb-16). Retrieved February 7, 2016, from https://www.hamamatsu.com/eu/en/technology/lifephotonics/BasicResearch/TerahertzWaveTechnology/index.html

The Engineering ToolBox (**2003**). *Coefficients of Linear Thermal Expansion*, Available:

https://www.engineeringtoolbox.com/linear-expansion-coefficients-d_95.html, (date last viewed: 01-Jan-20). Retrieved January 1, 2020, from https://www.engineeringtoolbox.com/linear-expansion-coefficients-d_95.html

Thermometrics (**2014**). *Thermocouples*, Available: http://www.thermocouplertd.com/thermocouple.html, (date last viewed: 01-Jan-20). Retrieved January 1, 2020, from http://www.thermocouplertd.com/thermocouple.html

Thompson, R. B. (**1990**). "Physical Principles of Measurements with EMAT Transducers," Phys. Acoust., Academic Press, New York, Vol. 19, pp. 157–200. doi:10.1016/B978-0-12-477919-8.50010-8

Thomson, W. T. (**1950**). "Transmission of Elastic Waves through a Stratified Solid Medium," J. Appl. Phys., **21**, 89–93. doi:10.1063/1.1699629

Tschoegl, N. W., Knauss, W. G., and Emri, I. (**2002**). "Poisson's ratio in linear viscoelasticity - a critical review," Mech. Time-Dependent Mater., **6**, 3–51. doi:10.1023/A:1014411503170

Tuncol, G., Danisman, M., Kaynar, A., and Sozer, E. M. (**2007**). "Constraints on monitoring resin flow in the resin transfer molding (RTM) process by using thermocouple sensors," Compos. Part A Appl. Sci. Manuf., **38**, 1363–1386. doi:10.1016/j.compositesa.2006.10.009

US-Biomat (**2015**). *Air-Coupled ultrasound transducers*, Available: https://us-biomat.com/research/air-coupled-ultrasound-transducers/, (date last viewed: 10-Jun-19). Retrieved June 10, 2019, from https://us-biomat.com/research/air-coupled-ultrasound-transducers/

Varnell, W. D., Doty, M. J., Richgels, S. H., Knox, T. M., and Parfomak, A. N. (**1992**). "Method for measuring degree of cure of resin in a composite material and process for making the same.," Retrieved from https://www.google.com/patents/US5142151

Visscher, W. M., Migliori, A., Bell, T. M., and Reinert, R. A. (**1991**). "On the normal modes of free vibration of inhomogeneous and anisotropic elastic objects," J. Acoust. Soc. Am., **90**, 2154–2162. doi:10.1121/1.401643

Wang, L., and Rokhlin, S. I. (**2001**). "Stable reformulation of transfer matrix method for wave propagation in layered anisotropic media," Ultrasonics, **39**, 413–424. doi:10.1016/S0041-624X(01)00082-8

Wang, Y. C., and Lakes, R. S. (**2003**). "Resonant ultrasound spectroscopy in shear mode," Rev. Sci. Instrum., **74**, 1371–1373. doi:10.1063/1.1535739

Webster, J. G. (**1999**). *The measurement, instrumentation, and sensors handbook*, 2588 pages. Retrieved from http://www.kelm.ftn.uns.ac.rs/literatura/si/pdf/Measurement Instrumentation Sensors.pdf

White, R. M. (**1963**). "Generation of Elastic Waves by Transient Surface Heating," J. Appl. Phys., **34**, 3559–3567. doi:10.1063/1.1729258

Whitney, T. M., and Green, R. E. (**1996**). "Low temperature characterization of carbon epoxy composites: an application of resonant ultrasound spectroscopy," Ultrasonics, **34**, 383–392. doi:10.1016/0041-624X(96)81782-3

Wilson, O. B. (**1988**). *Introduction to theory and design of sonar transducers*, Peninsula Pub, 212 pages.

Wong, K. K. (**2002**). *Properties of lithium niobate*, INSPEC, London, England, 417 pages.

Yakovlev, E. V, Zaytsev, K. I., Dolganova, I. N., and Yurchenko, S. O. (**2015**). "Non-Destructive Evaluation of Polymer Composite Materials at the Manufacturing Stage Using Terahertz Pulsed Spectroscopy," IEEE Trans. Terahertz Sci. Technol., **5**, 810–816. doi:10.1109/TTHZ.2015.2460671

Zhou, G., and Sim, L. M. (**2002**). "Damage detection and assessment in fibre-reinforced composite structures with embedded fibre optic sensors-review," Smart Mater. Struct., **11**, 925–939. doi:10.1088/0964-1726/11/6/314